LAWRENCE
LIVERMORE
NATIONAL
LABORATORY

LLNL-JRNL-862151

Magmatism and extension in the Death Valley extensional region with convergence of two migrating Cenozoic regional magmatic fronts

C.F. Chan, J. E. Andrew, N. M. McLean, A. Moeller

March 25, 2024

Geosphere

Disclaimer

DOI:10.1130/GES02808.1

LLNL-JRNL-862151

Tracking the spatial and temporal links between late Cenozoic extension and magmatism in the Death Valley region

Christine F. Chan[1,2], Joseph E. Andrew[2], Noah M. McLean[2], and Andreas Möller[2]

[1]Lawrence Livermore National Laboratory, Livermore, CA, 94550, USA

[2]Department of Geology, The University of Kansas, Lawrence, KS, 66045, USA

ABSTRACT

The relationship between Late Cenozoic magmatism and extension in the central Basin and Range province is complex, necessitating high-precision geochronology to understand its spatiotemporal connections. In the Death Valley region, the lack of high-precision U-Pb zircon ages has limited our understanding of the timing of pluton formation and its links to regional extension. We present new high-precision CA-ID-TIMS $^{206}Pb/^{238}U$ zircon ages and trace element analyses for eight Death Valley plutons. Our findings reveal three distinct phases of intrusive magmatism: (1) emplacement of shallow rapikivi granites at 13.2 Ma, (2) construction of the mid-crustal Black Mountain intrusive complex at 11.3 Ma, and (3) late emplacement of shallow, compositionally diverse intrusions at 8.2 Ma. A gap in zircon crystallization between 10 and 8.2 Ma coincides with exhumation of the Black Mountains and a transition from sill to dike emplacement. The dominance of rapakivi granites in the Death Valley region, which is rare among Cenozoic granitoids, is likely a result of rapid crustal extension that induces adiabatic decompression. A comparison of the timing of volcanism, plutonism, and tectonic events in Death Valley reveals that intrusive magmatism closely aligns with extension, underscoring the plutonic record as a vital link for understanding regional tectonics and changes in plate boundary dynamics during this period.

DOI:10.1130/GES02808.1

INTRODUCTION

Reconstructing the magmatic history in the Basin and Range province (western United States and northwestern Mexico; henceforth, "Basin and Range") from 50 Ma to 12 Ma reveals two distinct space-time trends that highlight the region's complex geologic evolution. The first trend shows a southwestward progression of magmatism across Nevada, while the second trend shows a northwestward progression through western Arizona into southern Nevada along the Colorado River extensional corridor (Fig. 1; Christiansen et al., 1992; Humphreys, 1995; Gans and Bohrson, 1998; Konstantinou et al., 2012; Best et al., 2013; cf. Glazner, 2022). These magmatic trends nearly converge at the narrowest part of the Basin and Range, where significant extension has occurred, particularly in the Death Valley region, which has undergone some of the greatest amounts of extension in the entire Basin and Range (e.g., Stewart, 1983; Wernicke et al., 1988; Wernicke, 1992; McQuarrie and Wernicke, 2005).

The relationship between Cenozoic magmatism and extension across the Basin and Range is complex. In the northern Basin and Range of Nevada, magmatism and extension appear to occur independently (Best and Christiansen, 1991; Colgan et al., 2006). Conversely, in the Colorado River extensional corridor of the southern Basin and Range, magmatism precedes large-magnitude extension (Fig. 1; Glazner and Bartley, 1984; Gans et al., 1989; Armstrong and Ward, 1991; Gans and Bohrson, 1998). This disparity raises intriguing questions about the primary drivers for magmatism in actively extending tectonic settings. Potential drivers in the Basin and Range include mantle plume processes (e.g., Best and Brimhall, 1974; Parsons et al., 1998; Wang et al., 2002), decompression melting resulting from continental extension (e.g., Gans et al., 1989; Christiansen et al., 1992; Wernicke, 1992; McQuarrie and Oskin, 2010; Putirka and Platt, 2012), northward migration of the Mendocino triple junction (e.g., Dickinson and Snyder, 1979; Glazner and Supplee, 1982), slab rollback (e.g., Humphreys, 1995, 2009; Feldstein and Lange, 1999), and variations of these processes.

The Death Valley region is characterized by multiple stages of deformation since ca. 15 Ma (e.g., Wernicke et al., 1988; Wright et al., 1991; Wernicke, 1992; Holm and Dokka, 1993; Davis et al., 1993; Topping, 1993; Miller, 1999; Miller and Friedman, 1999; McQuarrie and Wernicke, 2005; Andrew and Walker, 2009; Fridrich and Thompson, 2011; Norton, 2011; Andrew et al., 2015; Bidgoli et al., 2015; Sizemore et al., 2019; Fleming et al., 2021, 2022) and provides a significant record of late Cenozoic magmatism, featuring well-preserved volcanic deposits and exhumed plutons revealed through tectonic and erosional denudation (e.g., Drewes, 1963; McDowell, 1974; Asmerom et al., 1990; Holm and Wernicke, 1990; McKenna and Hodges, 1990; Wright et al., 1991; Davis et al., 1993; Calzia and Rämö, 2005; Luckow et al., 2005; Miller and Pavlis, 2005; Fridrich and Thompson, 2011; Calzia et al., 2016). The volcanic record provides snapshots of magmatic activity during discrete eruptive events, many of which reflect shorter-lived processes (e.g., Lipman, 1984; Bachmann et al., 2007). These snapshots may obscure the long-term evolution of regional magmatism, complicating our understanding of the

temporal links between extension and magmatism. In contrast, the plutonic record offers a more integrated view over extended periods (e.g., Hildreth, 1981; Matzel et al., 2006; Miller et al., 2011; Paterson et al., 2011), enhancing our understanding of the driving forces behind magmatism in extensional settings.

Despite the rich geological record, the relationship between intrusive magmatism and tectonics in the Death Valley region remains poorly understood, primarily due to the lack of modern high-precision crystallization ages for the region's plutons. In this study, we present new chemical abrasion–isotope dilution–thermal ionization mass spectrometry (CA-ID-TIMS) $^{206}Pb/^{238}U$ zircon ages and zircon trace element geochemical data for eight Miocene plutons in Death Valley (Fig. 2). This study aims to determine the timing and duration of plutonism in relation to regional tectonic processes. Specifically, we will: (1) assess whether intrusive magmatism occurs episodically or continuously, (2) identify spatiotemporal trends associated with intrusive magmatism, and (3) develop an integrated framework that connects plutonism, volcanism, and tectonism for the late Cenozoic in Death Valley.

GEOLOGIC BACKGROUND

Late Miocene extension in the Death Valley region has resulted from 42 km to 105 km of displacement across the region. This displacement was partitioned into a complex network of strike-slip and normal fault systems, which in its latest stage formed a pull-apart basin (e.g., Burchfiel and Stewart, 1966; Stewart, 1983; Wernicke et al., 1988; Serpa et al., 1988; Snow and Wernicke, 1989, 2000; Serpa and Pavlis, 1996; Norton, 2011). The Death Valley region consists of several crustal blocks of significant size, including the (1) Black Mountains, the tectonically exhumed footwall of the Amargosa-Black Mountains detachment; (2) Greenwater Range, a block dextrally offset from the Black Mountains; and (3) Panamint Range, a large hanging-wall block (Fig. 2).

The eastern part of the Death Valley region includes the Kingston Range–Halloran Hills detachment fault (Fig. 2; Burchfiel et al., 1983; Davis et al., 1993; Fowler and Calzia, 1999). The extensional breakaway of the Death Valley region occurs in the Kingston Range, indicated by exposed shallow footwall rocks that show minor amounts of displacement (Davis et al., 1993; Fowler and Calzia, 1999). In the following section, we provide a brief description of the Black Mountains, Greenwater Range, Kingston Range, and Panamint Range, along with the late Miocene plutons exposed in these ranges.

Black Mountains

The Black Mountains are a highly exhumed, southeast-tilted crustal block that exposes a structural discontinuity between (1) a footwall of metamorphosed Proterozoic rocks (e.g., Holm and Wernicke, 1990; Miller and Friedman, 1999; Miller and Pavlis, 2005) and mid-crustal Miocene intrusions (>10–20 km emplacement depth; Holm et al., 1992; Pavlis et al., 2018; Fleming et al., 2022) and (2) a hanging wall of Miocene–Pliocene volcanic and sedimentary rocks lying on highly deformed but unmetamorphosed Proterozoic strata with their underlying crystalline basement. This structural discontinuity is marked by the Amargosa–Black Mountains detachment fault (e.g., Holm and Wernicke, 1990; Miller, 1991, 2003; Wright et al., 1991; Holm et al., 1992; Holm and Dokka, 1993; Topping, 1993; Mancktelow and Pavlis, 1994; Miller and Pavlis, 2005). The Black Mountains preserve a complex sequence of repeated metamorphic and high-temperature deformation events since the Cretaceous (e.g., Holm et al., 1992; Miller and Friedman, 1999; Miller, 2003; Miller and Pavlis, 2005; Pavlis et al., 2018; Lima et al., 2018; Fleming et al., 2022).

The Black Mountains are known for three doubly plunging antiformal structures, locally termed as turtlebacks, which are exposed in the footwall rocks of the Amargosa–Black Mountains detachment fault (e.g., Curry, 1938, 1954; Wright et al., 1974, 1991; Holm and Wernicke, 1990; Holm et al., 1992; Holm and Dokka, 1993; Topping, 1993; Mancktelow and Pavlis, 1994). The three turtleback structures—Badwater, Copper Canyon, and Mormon Point (from north to south)—are composed of quartz-feldspar gneiss, pelitic schist, and calcite-dolomite marble rocks that are ductilely sheared, faulted, and folded (e.g., Curry, 1938, 1954; Drewes, 1959; Otton, 1977; Miller, 1991, 1992; Pavlis, 1996; Miller and Friedman, 1999; Çemen et al., 2005; Miller and Pavlis, 2005). Miocene plutons form sill-like intrusions along the structural top of each turtleback and surround the Copper Canyon and Mormon Point turtlebacks (Fig. 2). The basal parts of these sills are mylonitic and are interpreted to represent the exhumed brittle-ductile transition (e.g., Holm et al., 1994b, 1994a; Pavlis, 1996; Miller and Pavlis, 2005). Late Miocene–aged dikes crosscut the Miocene intrusions and turtleback structures (e.g., Wright et al., 1991; Holm et al., 1992; Miller and Friedman, 1999; Dee et al., 2004).

Thermochronology studies of the Black Mountains indicate that high exhumation rates occurred between 10 Ma and 8 Ma (McKenna, 1990; Meurer, 1992; Holm and Dokka, 1993; Bidgoli et al., 2015; Sizemore et al., 2019). This rapid extension resulted in the unroofing of multiple mid-crustal plutons in the western Black Mountains, including the Willow Spring Diorite, Smith Mountain Granite, and quartz monzonite of Gold Valley. Additionally, another diorite intrusion, known as the diorite of Furnace Site, was previously classified as part of the northern Willow Spring Diorite but is distinguishable by its finer-grained texture.

Greenwater Range

The Greenwater Range is dextrally offset by ~15 km along the Grandview fault from the Black Mountains crustal block (Topping, 1993). This range is composed primarily of late Miocene to Pliocene volcanic rocks (Fig. 2). Plutonic rocks are exposed in several erosional windows beneath a nonconformable contact (Holm et al., 1992) or possibly locally a detachment fault (Calzia and Rämö, 2005). The plutonic rocks range in composition from quartz monzonite to granite (Haefner, 1972; Almashoor, 1983; Holm et al., 1992; Holm, 1995; Petronis et al., 2002; Rämö et al., 2011) and include the granite of Deadman Pass and the Shoshone Granite.

Kingston Range

The Kingston Range exposes Proterozoic rocks similar to those in the southern Black Mountains but at lower metamorphic grades (Calzia et al., 2000). These rocks have been minimally exhumed by the Kingston Range–Halloran Hills detachment, which partially reactivates or is localized along a section of Jurassic and Cretaceous thrust faults exposed southeastward in the Mesquite and Clark Mountains (Fig. 2; Burchfiel et al., 1987; Snow and Wernicke, 1989; Walker et al., 1995). The detachment offsets Proterozoic to Paleozoic sedimentary rocks, 14–13 Ma volcanic rocks, and 13–8 Ma supradetachment basin rocks that dip 30° eastward (Davis et al., 1993; Fowler and Calzia, 1999). Following the initiation of ~6 km of WSW-directed displacement along the Kingston Range–Halloran Hills detachment, the Kingston Range Granite was emplaced (Fig. 2; Calzia, 1990; Fowler and Calzia, 1999; Calzia and Rämö, 2000), effectively pinning a segment of the detachment fault. Consequently, a system of strike-slip faults developed to the north and south along with a normal fault to the west, surrounding the granite-pinned segment of the detachment to accommodate continued extension (Davis et al., 1993).

Panamint Range

The western boundary of our study area is defined by the Panamint Range (Fig. 2), a structural block situated between two west-dipping faults: the Emigrant detachment fault and Eastern Panamint fault system. The Emigrant detachment fault, which bounds the western side of the Panamint Range, has experienced two phases of deformation: (1) moderate down-to-the-west extension at 15–10 Ma, followed by (2) rapid unroofing with top-to-the-northwest displacement starting at ca. 4 Ma (Andrew and Walker, 2009; Bidgoli et al., 2015). The Eastern Panamint fault system has been active since after 10 Ma, dipping westward beneath the Panamint Range. It is interpreted as a hanging-wall splay of the Amargosa–Black Mountains detachment fault with top-to-the-northwest displacement (McKenna and Hodges, 1990). The hanging wall exposes Paleoproterozoic crystalline basement, Mesoproterozoic to Triassic sedimentary rocks, Mesozoic plutonic and volcanic rocks, and Miocene plutonic and volcanic rocks (e.g., Wasserburg et al., 1959; Lanphere et al., 1964; Stern et al., 1966; McDowell, 1974). Miocene plutonism includes the Little Chief Granite, which intrudes the central Panamint Range (Hunt and Mabey, 1966; McDowell, 1974, 1978; Topping, 1993).

Miocene Intrusions in the Death Valley Region

In this study, we focus on eight plutons exposed in the Death Valley region, including several plutons exposed in the footwall of the main extensional fault system, the Amargosa–Black Mountain detachment, and a pluton in the hanging wall (Table 1). The Willow Spring Diorite, Smith Mountain Granite, quartz monzonite of Gold Valley, and diorite of Furnace Site are exposed in the Black Mountains; the granite of Deadman Pass in the Greenwater Range; the Little Chief Granite in the Panamint Range; the Kingston Range Granite in the Kingston Range; and the granite of Rabbit Holes Spring, just west of the Kingston Range (Fig. 2). These plutons all intrude Paleoproterozoic to Neoproterozoic rocks (e.g., Hewett, 1940; Otton, 1977; McDowell, 1978; Holm and Wernicke, 1990; Miller, 1992; Pavlis, 1996; Mahon et al., 2014). Notably, all the felsic granitoids in Death Valley have rapakivi textures, potassium feldspar megacrysts mantled by plagioclase feldspar. A summary of all Miocene intrusions in Death Valley, including those outside the scope of this study, is provided in Table 2.

Kingston Range Granite

The Kingston Range Granite is an elliptical rapakivi granite (~150 km^2) exposed in the Kingston Range (Fig. 2; Hewett, 1956; Calzia, 1990; Calzia et al., 2000; Calzia and Rämö, 2005). This granitic porphyry intrudes unmetamorphosed Mesoproterozoic to Neoproterozoic Pahrump Group strata (Hewett, 1940; Mahon et al., 2014). The Kingston Range Granite has three phases (from oldest to youngest): (1) northeastern feldspar porphyry, (2) southwestern quartz porphyry, and (3) aplite (Calzia and Rämö, 2005). The Kingston Range Granite contains widespread miarolitic cavities, consistent with shallow emplacement (<4 km; Calzia, 1990; Davis et al., 1993). Mafic xenoliths and rhyolite porphyry dikes are commonly found in both the feldspar porphyry and quartz porphyry phases. The only geochronology for the Kingston Range Granite is a 12.4 Ma hornblende $^{40}Ar/^{39}Ar$ age (Calzia, 1990).

Granite of Rabbit Holes Spring

The granite of Rabbit Holes Spring is a small rapakivi intrusion (~8 km^2) located west of the Kingston Range (Fig. 2). There are two phases of the granite: (1) gray, medium-grained, monazite-bearing biotite monzogranite and (2) tan, medium- to coarse-grained monzogranite. The tan monzonite phase is typically equigranular but locally porphyritic and commonly contains pegmatite dikes and blocks of gray monzonite (Calzia et al., 2003). The granite of Rabbit Holes Spring was previously interpreted as Cretaceous despite K-Ar biotite ages of 11.0 Ma and 11.6 Ma from the gray and tan granite phases, respectively (Calzia, 1990; Calzia et al., 2003).

Little Chief Granite

The Little Chief Granite is a shallow (<4 km emplacement depth) granite exposed over an area of ~28 km^2 that intrudes Paleoproterozoic gneiss and Meso- to Neoproterozoic metasedimentary rocks of the Panamint Range (Fig. 2; McDowell, 1978). The Little Chief Granite possesses hypabyssal and rapakivi textures, miarolitic cavities, and mafic inclusions (McDowell, 1974). The granite has two phases: a northern phase, which intrudes the southern phase (McDowell, 1974). The southern phase contains abundant accessory monazite, commonly coarse enough to be visible in hand sample. Prior geochronology for the Little Chief Granite includes: (1) a K-Ar feldspar age of 12.5 ± 1.3 Ma (Stern et al., 1966) from a boulder located at the mouth of the Hanaupah Canyon, (2) a plagioclase-biotite-hornblende Rb-Sr isochron of a similar boulder from Hanaupah Canyon with an age of 10.6 ± 0.2 Ma (Hodges et al., 1990), (3) an $^{40}Ar/^{39}Ar$ biotite age of 11.21 ± 0.08 Ma (McKenna, 1990), and (4) zircon fission-track ages of 11.2 ± 0.5 Ma and 9.8 ± 0.5 Ma for the southern and northern facies, respectively (Topping, 1993).

Willow Spring Diorite

The Willow Spring Diorite is the largest Miocene intrusion in Death Valley, exposed over ~300 km^2 in the Black Mountains (Fig. 2; Asmerom et al., 1990). This intrusion is a hornblende gabbro to quartz diorite and appears to form sheets that locally intermingle (Asmerom et al., 1990; Holm, 1995). The Willow Spring Diorite intrudes 1.7 Ga crystalline rocks, Mesoproterozoic metadolomite, and Neoproterozoic Noonday Dolomite (Wright et al., 1974, 1991; Otton, 1977; Holm et al., 1992; Miller and Friedman, 1999; Miller, 2003). The mafic phases of the intrusion are likely sourced from mantle-dominated magmas based on low $^{87}Sr/^{86}Sr$ and high εNd. Isotopic variations on the tens-of-meters scale within the Willow Spring Diorite suggest that magma mixing occurred at or close to the depth of emplacement (Asmerom et al., 1990). Prior geochronology includes three U-Pb bulk zircon TIMS ages using older analytical methods (no chemical abrasion): (1) 10.93 ± 0.75 Ma (Wright et al., 1991), (2) 11.6 ± 0.2 Ma, and (3) 11.5 ± 0.1 (Asmerom et al., 1990). Hornblende and biotite $^{40}Ar/^{39}Ar$ ages indicate that the Willow Spring Diorite cooled to ~500 °C by ca. 10 Ma and then to ~350 °C by ca. 8 Ma (McKenna, 1990; Holm and Dokka, 1993).

The Willow Spring Diorite was emplaced as a sill-like body above the turtlebacks (Fig. 2), which represent the floor of the Willow Spring Diorite pluton, in a mid-crustal shear zone (Holm et al., 1992; Pavlis, 1996; Miller and Pavlis, 2005). Ductile fabrics are generally limited to the lowermost part of the pluton (Pavlis, 1996), and structurally higher levels are capped by the curved fault systems of the Death Valley turtlebacks (e.g., Holm and Wernicke, 1990; Miller, 1991, 1992; Pavlis, 1996). Brittle deformation that overprints ductile foliation is observed only in the northern part of the shear zone at the base of the diorite sill (Holm and Wernicke, 1990).

Smith Mountain Granite

The Smith Mountain Granite is a biotite rapakivi granite exposed over an area of ~40 km^2 in the southern Black Mountains (Fig. 2). The Smith Mountain Granite intrudes the ductile shear zone of the Mormon Point turtleback (Miller et al., 2004), which includes 1.7 Ga metamorphic basement rocks and the upper portion of the Willow Spring Diorite. The Smith Mountain Granite and Willow Spring Diorite show magma mingling textures, suggesting that the two plutons are comagmatic (Meurer, 1992; Holm et al., 1994a, 1994b; Miller et al., 2004). But in contrast to the diorite, the Smith Mountain Granite lacks ductile deformation structures. Prior $^{40}Ar/^{39}Ar$ geochronology for the Smith Mountain Granite yielded ages ranging from 8.69 ± 0.31 Ma (hornblende; Holm et al., 1992) to 10.85 ± 0.04 Ma (orthoclase; Holm et al., 1994a). Two TIMS

U-Pb zircon analyses, using older analytical methods (no chemical abrasion), yielded a crystallization age of 10.45 ± 0.22 Ma (Miller et al., 2004).

Quartz Monzonite of Gold Valley

The Willow Spring Diorite and Smith Mountain Granite are intruded by a medium-grained quartz monzonite pluton and associated dikes, collectively known as the quartz monzonite of Gold Valley, located east of the Copper Canyon turtleback (Holm, 1995). This quartz monzonite pluton contains minor biotite and amphibole and locally exhibits rapakivi textures (Drewes, 1963). The quartz monzonite of Gold Valley appears as a sheeted, tabular pluton that intrudes into the upper portion of the Willow Spring Diorite as numerous subhorizontal interconnected sills. In some places, the quartz monzonite of Gold Valley and Willow Spring Diorite are interfingering, and in other places they form a faulted contact with each other (Supplemental Material[1]). Hornblende $^{40}Ar/^{39}Ar$ dating yields a cooling age of 8.69 ± 0.31 Ma (Holm et al., 1992).

Granite of Deadman Pass

The granite of Deadman Pass is one of several porphyritic and rapakivi quartz monzonite–granite plutons in the Greenwater Range (e.g., Calzia and Rämö, 2005; Calzia et al., 2016). These intrusions were emplaced shallowly (2–2.5 km) and are exposed in erosional windows through Miocene and Pliocene volcanic rocks (Almashoor, 1983). Other granitoids are exposed along the southwest side of the Greenwater Range (Drewes, 1963) and below the Shoshone Volcanics located southeast of the granite of Deadman Pass. The granite of Deadman Pass contains several large xenoliths of gneiss, marble, and quartzite, consistent with intrusion into Neoproterozoic to Mesoproterozoic bedrock (Haefner, 1972).

Diorite of Furnace Site

The diorite of Furnace Site is a fine-grained quartz diorite that was previously mapped as the northern biotite-bearing phase of the Willow Spring Diorite (Otton, 1977). The diorite intruded as a sill-like body below a sheet of quartz monzonite. The diorite is located below the unconformity exposed at Furnace Site. Based on new U-Pb zircon geochronology and zircon trace element data presented herein, we separate this unit out as a distinct diorite pluton younger than the Willow Spring Diorite.

METHODS

Sample Collection and Mineral Separation

Eight intrusions were sampled across the Death Valley region, with multiple intrusive phases collected from the Kingston Range Granite, Little Chief Granite, Willow Spring Diorite, and Smith Mountain Granite. Samples of the granite of Rabbit Holes Springs were obtained from J. Calzia (personal commun., 2020), a sample of diorite of Furnace Site was provided by R. Thompson and A. Gilmer (personal commun., 2019), and a sample of the quartz porphyry phase of the Kingston Range Granite from T. Bidgoli (personal commun., 2012). Within the largest intrusion, Willow Spring Diorite, rock samples were obtained from different structural levels (Fig. 2). Field photographs can be found in the Supplemental Material.

Zircon separation from rock samples followed standard heavy mineral separation techniques to isolate grains. Selected zircon grains were annealed for 60 h at 900 °C in a muffle furnace, modified after the CA-TIMS method of Mattinson (2005). Annealed grains were mounted in epoxy and polished halfway to expose the interior of the grains. Cathodoluminescence (CL) imaging was conducted using a JEOL 5800 LV scanning electron microscope (SEM) with a K.E. Developments panchromatic CL detector at the U.S. Geological Survey in Denver, Colorado, USA. Based on the internal structures and zoning patterns in the CL

imagery (Fig. S1), we targeted specific zircon grains for CA-ID-TIMS U-Pb geochronology and zircon trace element analysis (TIMS-TEA; Schoene et al., 2010). To fully investigate zircon crystallization histories, we selected zircons of varying grain sizes, and where possible, we microsampled grains to isolate tips and cores as informed by CL imagery. Grain fractions that were large enough to break into multiple fragments were separated into two to three pieces and are indicated with a letter at the end of the fraction identifier: T, C, and B correspond to top (tip), center, and bottom (other tip) fragments of a grain, respectively (Table 3; Fig. S1).

U-Pb Zircon Geochronology by CA-ID-TIMS

Selected grains and grain fragments were loaded into 300 µL fluorinated ethylene propylene (FEP) microcapsules and leached in 50 µL of 29 M HF in a Parr acid digestion vessel for 12 h at 210–215 °C. Grains were subsequently fluxed with 7 M HNO_3 for at least 20 min, rinsed four times with ultrapure water, fluxed again with 6 M HCl for at least 20 min, and finally rinsed four times with ultrapure water. Following chemical abrasion treatment, zircon grains and grain fragments were loaded into individual microcapsules with 50 µL of 29 M HF and ~0.009 g of a mixed EARTHTIME ^{205}Pb-^{233}U-^{235}U tracer (ET535; Condon et al., 2015; McLean et al., 2015). Samples were dissolved in a Parr vessel for ~60 h at 210–215 °C, dried to salts, converted to chlorides by fluxing microcaps with ~50 µL of 6 M HCl overnight either in a Parr vessel at >180 °C or on a hotplate at 100 °C, dried to salts again, and finally redissolved in 50 µL of 3 M HCl for anion-exchange chemistry. Separation and purification of Pb and U from zircon followed a modified procedure from Krogh (1973) using 50 µL HCl-based AG 1-X8 resin. Prior to Pb and U elution, trace elements were eluted dropwise using ~75 µL of 3 M HCl. Pb and U were eluted into the same Teflon beaker with 200 µL of 6 M HCl and 250 µL of ultrapure water, respectively, and were dried down with ~5 µL of ~0.018 M H_3PO_4.

Pb and U isotopic data were collected on an Isotopx Phoenix thermal ionization mass spectrometer at The University of Kansas Isotope Geochemistry Laboratories (KU IGL). Both Pb and U were loaded onto the same degassed zone-refined rhenium filament using a mixed solution of colloidal silica gel and dilute H_3PO_4 (Gerstenberger and Haase, 1997). Pb was analyzed as Pb^+ via peak-hopping on a Daly ion counting system, while U was analyzed as UO_2^+ statically on Faraday collectors. Isotopic fractionation corrections for Pb and U are based on repeated analysis of certified Pb reference materials (NBS981 and NBS982) and the estimated $^{233}U/^{235}U$ in the ET535 tracer solution, respectively (Condon et al., 2015). Data reduction and uncertainty propagation were performed using Tripoli and ET_Redux software packages (Bowring et al., 2011) with algorithms detailed in McLean et al. (2011).

Zircon Th/U ratios are calculated from CA-ID-TIMS U-Pb analysis. The U content was determined by isotope dilution, and the Th content was calculated from the radiogenic ^{208}Pb measurement and ^{230}Th-corrected $^{206}Pb/^{238}U$ date of the zircons, assuming concordance between the U-Pb and Th-Pb systems. Initial ^{230}Th disequilibrium corrections were applied to the zircon $^{206}Pb/^{238}U$ ages assuming that the Th/U of the melt is the same as the whole-rock Th/U (Table S2; Kirkland et al., 2015; Gilmer and Thompson, 2024). For plutons for which whole-rock data do not exist (e.g., Little Chief Granite, granite of Rabbit Holes Spring, and Kingston Range Granite), we assume 3.5 for the whole-rock Th/U ratio, as that is the mean value for granitoids (Kirkland et al., 2015). All age and isotope ratio uncertainties are reported as ±2σ (95% confidence intervals; Table 3).

Zircon Trace Element Analysis

Zircon trace element analysis (TEA) was performed using the Element2 inductively coupled plasma–mass spectrometer (ICP-MS) with an Elemental Scientific Instruments Apex-

Omega HF desolvating nebulizer at KU IGL. Our TEA sample preparation and analysis follow a modified TIMS-TEA procedure from Schoene et al. (2010). Trace element aliquots collected during U-Pb chemistry separation were dried to salts, dissolved with ~7 M HNO_3 to remove organics, dried down again, and finally redissolved in 1 mL of a mixed 0.45 M HNO_3 and 0.02 M HF solution that is doped with ~1 ppb Ir. Ir is used as an internal standard to monitor potential plasma fluctuations and varying nebulizer aspiration rates between samples (Schoene et al., 2010).

Instrument and desolvating nebulizer settings, such as gas flow, radio-frequency power, and torch positions, were optimized for high sensitivity ($\geq 1.2 \times 10^7$ cps/ppb ^{238}U) and minimal oxide formation ($UO^+/U^+ < 0.4\%$) based on a 1 ppb multielement calibration solution. The same solution was also used for mass and analog-counting-factor calibrations, which were performed at the start of each ICP session. Analyses were conducted in low mass resolution ($m/\Delta m = 400$) mode. The flow rate of the Teflon nebulizer is 125 µL/min, while the uptake time was set to 40–45 s. A small aliquot of each sample was diluted by 100× and analyzed for Zr, Ti, La, Dy, Yb, and Hf for a rapid "dip-test" run. Based on the rapid "dip tests", all samples were diluted so that samples did not exceed 40 ppb Zr to minimize large Zr intensities while still being able to measure lower abundance trace elements (e.g., light rare earth elements [REEs]).

When collecting TIMS-TEA analyses, four calibration solutions bracketed 15 unknown samples, and a blank sample was analyzed prior to each standard or sample. Our calibration solutions contained a range of concentrations (4.5–150 ppb Zr, 1–500 ppt REEs). Elements analyzed include Y, Zr, Hf, and REEs. Between samples, a series of rinses using a mixed 0.45 M HNO_3 and 0.02 M HF solution was performed. Procedural blanks were prepared and measured alongside samples.

Data reduction of TIMS-TEA analyses, including corrections for procedural and acid blanks, as well as concentration calculations were performed using MATLAB software. To convert from solution concentrations to zircon concentrations, it is assumed that all measured trace elements substitute for Zr^{+4} so that the sum $\Sigma = Zr + Hf + Sc + Y + Nb + Ta + REEs = 497{,}646$ ppm, which is the stoichiometric concentration of the Zr site in zircon (Hoskin and Schaltegger, 2003). Given that the uncertainty in the normalization factor is a systematic error, this error was not propagated because these uncertainties would cancel out for elemental ratios. No significant laboratory trace element contamination is observed from analyzed total procedural blanks. Results are summarized in Table S1 with uncertainties reported as 2σ (95% confidence intervals).

RESULTS

U-Pb Zircon Geochronology

Thirteen samples from eight Miocene intrusions in the Death Valley region (Table 1) were dated by CA-ID-TIMS U-Pb zircon geochronology. These Miocene zircon grains show typical oscillatory and sector zoning patterns. CL images are provided in Figure S1. Isotopic ratios and CA-ID-TIMS U-Pb dates are presented in Table 3 and illustrated in Figure 3. We interpret each rock sample to represent a single magmatic phase of its respective plutons.

Collectively, the ~140 CA-ID-TIMS U-Pb zircon dates define a protracted magmatic history extending from 13.17 Ma to ca. 7.88 Ma (Fig. 3). Ten out of the thirteen CA-ID-TIMS samples exhibit $^{206}Pb/^{238}U$ age dispersion that is greater than analytical uncertainties, while three samples have a single resolvable population of zircon crystallization ages (Table 4). For samples with resolvable age dispersion, we use the Bayesian algorithm in the software Chron.jl (Keller et al., 2018) to estimate the maximum (t_{max}) and minimum (t_{min}) of the zircon age distribution,

which can be interpreted as estimates of the time at which the magmatic system reaches zircon saturation and the solidus, respectively (Table 4; Fig. S2). Given that zircon age distributions are inherently asymmetric (Keller et al., 2018), crystallization time scales (Δt) are the mode of the kernel density estimation distribution of $t_{max} - t_{min}$. These estimates rely on the assumption that zircon crystallization is continuous from the start of zircon saturation until the solidus is reached. Using this approach ensures that the crystallization age range is not artificially expanded by analytical uncertainties (Keller et al., 2018). The largest age dispersion in a single sample is observed in the lower Willow Spring Diorite (786 $^{+0.18}/_{-0.06}$ k.y.). Protracted crystallization histories (≥550 k.y.) were also documented in individual zircon grains where multiple fractions from the same grain are dated (sample DVCC18-2: fractions XL10B, XL10C, and XL10T; Table 3).

Some Death Valley samples exhibit distinct zircon U-Pb age distributions. For example, the Kingston Range Granite feldspar porphyry phase shows at least two distinct zircon age populations (Fig. 3). Inheritance is not common in these zircon grains, and apart from the granite of Deadman Pass, no sample contains zircon dated at millions or tens of millions of years older than the main age population. Although we targeted zircon grains that did not show obvious xenocrystic cores based on the SEM-CL imaging (Fig. S1), a few zircons dated in the granite of Deadman Pass have Proterozoic ages (1.1–1.6 Ga) and are thus excluded from the data.

Zircon Trace Element Analyses

A subset of the dated zircon grains was also analyzed for trace elements by TIMS-TEA. The advantage of TIMS-TEA over in-situ techniques is that is that the trace element data are measured on the same sample volume dated by CA-ID-TIMS, allowing us to track chemical trends through time (Schoene et al., 2010, 2012; Wotzlaw et al., 2013; Samperton et al., 2015). Zircon trace element data are presented in Figures 4–6 as scatter plots of trace element ratios, and the full data set is provided in Table S1.

U-Pb zircon ages are plotted against different trace element ratios that track magma fractionation (Figs. 4–6). For example, zircon Th/U and Zr/Hf ratios increase and decrease, respectively, with progressive zircon fractionation in an evolving melt and can be used to help differentiate magma sources. This is also true for Lu/Hf ratios, although the heavy REEs (e.g., Lu) are compatible in clinopyroxene, amphibole, and garnet, so if any of these phases crystallized prior to zircon saturation, then Lu would decouple from Hf (Dickinson and Hess, 1982; Watson and Harrison, 1983; Boehnke et al., 2013; Bea et al., 2018). Other useful chemical discriminators include the Eu anomaly (Eu/Eu*), which is sensitive to plagioclase fractionation and oxidation state (Dilles et al., 2015), and Yb/Dy ratios, which are sensitive to amphibole and/or titanite fractionation.

Zircon Th/U ratios are also useful for fingerprinting the magma composition and physical conditions of crystal growth (e.g., temperature). If zircon is in equilibrium with its parent melt, higher-temperature melts are characterized by decreasing zircon Th/U ratios with increasing temperature while fractionated melts are characterized by decreasing Th/U ratios with decreasing temperatures (Kirkland et al., 2015). A compilation of felsic magma zircon Th/U ratios from across the western United States shows that the average Th/U ratio of an igneous zircon is 0.5, though magmatic zircon from granitic to dioritic compositions can have a mean Th/U ratio of 0.75–1.03 (e.g., Bindeman et al., 2006; Kirkland et al., 2015). All zircons in this study exhibit Th/U ratios >0.5. Several of the pluton samples are highly enriched in Th, with zircon Th/U ratios >1.5 in the southern phase of the Little Chief Granite and diorite of Furnace Site (Fig. 4).

The most noticeable temporal zircon trace element trends occur in the Willow Spring Diorite between 11.26 Ma and 10.08 Ma, where Zr/Hf and Eu/Eu* ratios steadily increase and $(Yb/Dy)_N$ ratios, where the subscript N denotes values normalized to chondrite (following Sun and McDonough, 1989), decrease (Fig. 5). In general, the lower Willow Spring Diorite zircons (pink circles in Figs. 4–6) have lower Th/U, Zr/Hf, Lu/Hf, and Eu/Eu* ratios with moderately higher $(Yb/Dy)_N$ ratios compared to the middle Willow Spring Diorite zircons (purple circles). The northern diorite zircons (diorite of Furnace Site, dark blue circles) are distinct from the Willow Spring Diorite with higher Th/U ratios and show some of the largest ranges in trace element ratio values (e.g., Th/U, Zr/Hf, Lu/Hf, and Eu/Eu*; see Figs. 4–6). The Smith Mountain Granite (light and dark green triangles) and quartz monzonite of Gold Valley (yellow squares) zircons are chemically similar to the lower and middle Willow Spring Diorite zircons. The granite of Deadman Pass zircons (red squares) also exhibit low Th/U ratios but high Zr/Hf ratios with a narrow range of Lu/Hf and Yb/Dy ratios.

During zircon crystallization, Hf is preferentially removed from the melt and therefore serves as a useful proxy for magmatic differentiation (Linnen and Keppler, 2002). Zircon trace element ratios are plotted against Hf content in Figure 6 and are separated based on rock composition, with dioritic intrusions in the left column and felsic intrusions in the right column. With exception of granite of Deadman Pass, all other plutons show decreasing $(Yb/Dy)_N$ ratios with decreasing Hf content, indicating co-crystallization of amphibole and zircon. A positive trend in Eu/Eu* ratios with decreasing Hf content is observed in the Smith Mountain Granite and quartz monzonite of Gold Valley zircons, which records decreasing plagioclase fractionation during zircon crystallization and magmatic differentiation. In the dioritic intrusions, high-Hf (>9500 ppm) zircons have larger Eu/Eu* anomalies while low-Hf (<9500 ppm) zircons have smaller Eu/Eu* anomalies. This could indicate either that plagioclase fractionation was more prevalent in the early and more primitive melts or that there was a change in redox conditions to more oxidized magmas, which would suppress the magnitude of Eu anomalies (Tang et al., 2018). The zircons in the felsic intrusions show a clear plagioclase fractionation trend with magmatic differentiation, which is not visible in the zircons from mafic intrusions, indicating that a change to more oxidizing conditions is a more likely explanation.

DISCUSSION

Timing of Pluton Emplacement in Death Valley

Our high-precision U-Pb zircon data set represents the first modern single-grain CA-ID-TIMS U-Pb zircon data set for late Cenozoic intrusions in the Death Valley region, offering crucial insights into the region's plutonic history. This dataset allows us to divide intrusive magmatism into three distinct phases: (P1) early rapakivi granite magmatism, represented by the Kingston Range Granite, granite of Rabbit Holes Spring, and Little Chief Granite; (P2) the construction of the Black Mountains intrusive complex, which includes the Willow Spring Diorite, Smith Mountain Granite, and the quartz monzonite of Gold Valley; and (P3) late-stage plutonism in the Black Mountains and Greenwater Range, represented by the diorite of Furnace Site and the granite of Deadman Pass.

Phase I: Early Granite Magmatism (P1)

The first phase (P1) of Miocene plutonism in the Death Valley region began with the construction of the Kingston Range Granite at $13.166\ ^{+0.136}/_{-0.028}$ Ma, based on our measured estimate of the earliest preserved evidence of zircon crystallization (calculations here and throughout) use the methods of Keller et al., 2018). Zircon ages indicate that the feldspar porphyry phase was constructed slowly over 742 k.y. in two distinct pulses (Fig. 3). In contrast,

the quartz porphyry phase of the Kingston Range Granite crystallized more rapidly within 281 k.y. (Table 4). This rapid emplacement aligns with field observations indicating that the quartz porphyry phases was intruded as a sill-like body beneath the feldspar porphyry phase (Calzia and Rämö, 2005). Following emplacement, the Kingston Range Granite cooled rapidly, as shown by overlapping zircon U-Pb ages with published $^{40}Ar/^{39}Ar$ hornblende ages (12.36 ± 0.18 Ma; Calzia, 1990). Rapid cooling supports earlier interpretations that the granite was emplaced in the shallow crust (<4 km depth), supported by the widespread presence of miarolitic cavities (Davis et al., 1993; Calzia and Rämö, 2005). Additionally, crosscutting relationships between the Kingston Range–Halloran Hills detachment and the Kingston Range Granite further suggest that this pluton was emplaced within an active detachment fault system (Davis et al., 1993).

The Kingston Range Granite exhibits multiple age populations and abundant disequilibrium textures, such as rapakivi feldspars and mafic xenoliths, indicating the role of mantle-derived melts and magma mixing processes in the generation of Kingston Range Granite magmas (Hibbard, 1981; Cantagrel et al., 1984; Calzia and Rämö, 2005). The zircon Th/U ratios between the two porphyry phases overlap, suggesting that they crystallized from the same or similar melt compositions.

The granite of Rabbit Holes Spring, located ~1 km west of the Kingston Range Granite across alluvial valley fill, began crystallizing at the end of Kingston Range Granite magmatism. The construction of the granite of Rabbit Holes Spring occurred between 12.148 $^{+0.091}/_{-0.038}$ Ma and 11.830 $^{+0.055}/_{-0.042}$ Ma (Table 4). Unlike the Kingston Range Granite, granite of Rabbit Holes Spring zircon crystallized as a single, continuous pulse over a period of 320 k.y. Zircon Th/U ratios range from 0.75 to 1.98 and do not show a trend with U-Pb zircon ages (Fig. 4). This suggests either that the granite of Rabbit Holes Spring zircon did not crystallize from a single fractionating melt body or that fractionation occurred on time scales shorter than the precision achievable by CA-ID-TIMS U-Pb ages (e.g., Kirkland et al., 2015).

This was followed by the emplacement of the Little Chief Granite, which began at 11.557 $^{+0.093}/_{-0.070}$ Ma. This intrusion was constructed relatively rapidly, in ~291 k.y., starting with the southern intrusive phase followed by northern intrusive phase (Table 4). Although both phases exhibit overlapping zircon crystallization ages, field evidence indicates the northern phase intruded into the southern phase (McDowell, 1974). The southern phase is characterized by high zircon Th/U ratios (0.8–2.5; Fig. 4), best explained by the assimilation of enriched continental crust, such as dolomite. McDowell (1974) documented field, petrographic, and geochemical evidence of dolomite assimilation in the Little Chief Granite. The southern phase also contains abundant monazite, commonly coarse enough to be visible in hand samples. It is likely that zircon crystallization predates monazite saturation given that coexisting zircon with monazite would yield low zircon Th/U ratios, similar to metamorphic zircon in monazite-bearing rocks (Vavra et al., 1999; Rubatto et al., 2001; Cesare et al., 2003; Rubatto, 2017).

By comparing emplacement ages with published zircon fission-track (ZFT) ages, we can assess how rapidly the Little Chief Granite was exhumed after it was emplaced. We interpret the youngest estimated time of zircon crystallization (see Fig. 7 and Table 4) as the age at which the granite cooled through the solidus, making it equivalent to the emplacement age. ZFT ages for the northern and southern phases are reported as 9.8 ± 1.0 Ma and 11.2 ± 1.0 Ma, respectively (Topping, 1993). These data sets suggest that the pluton was rapidly cooled following emplacement (McDowell, 1974; Topping, 1993). Groundmass mineral assemblage barometry suggests that crystallization occurred at an estimated depth of ~4 km while emplacement depths are estimated to be <2.8 km (McDowell, 1978).

Phase I intrusive magmatism (P1) was characterized by emplacement of shallow (<4 km) rapakivi granites (Fig. 7; McDowell, 1974; Calzia and Rämö, 2005). Each granite is composed of several mappable intrusive facies with distinct mineralogy, zircon crystallization histories, and chemistry (this study; McDowell, 1974; Calzia and Rämö, 2005).

Phase II: Black Mountains Intrusive Complex (P2)

Phase II intrusive magmatism (P2) is characterized by the synchronous crystallization of multiple mid-crustal plutons in the Black Mountains (Fig. 7). Collectively referred to as the Black Mountains intrusive complex, P2 includes the Willow Spring Diorite, Smith Mountain Granite, and quartz monzonite of Gold Valley. All three intrusions exhibit overlapping zircon crystallization histories (Fig. 3) and display comagmatic relationships, such as magma mingling textures and mutually intrusive contacts (Asmerom et al., 1990; Meurer, 1992; Holm et al., 1994b, 1994a).

The Willow Spring Diorite is the most voluminous late Cenozoic pluton in the Death Valley region. Zircon crystallization began by $11.260\ ^{+0.115}/_{-0.024}$ Ma and continued for at least 1.17 m.y. (Table 4). The oldest and most mafic unit sampled, the lower Willow Spring Diorite, crystallized over 786 k.y. In contrast, the middle Willow Spring Diorite crystallized more rapidly, within 250 k.y. The youngest unit, the upper Willow Spring Diorite, began zircon crystallization at or before $10.086\ ^{+0.046}/_{-0.015}$ Ma. This sample shows a clear single resolvable zircon age population with a mean square of weighted deviates (MSWD) of 0.6 (Table 4). Our U-Pb ages are younger than the previously published age of 11.6 Ma (Asmerom et al., 1990). One possible explanation for this discrepancy is that their multigrain age may include zircon with Mesozoic or Proterozoic inheritance.

Each Willow Spring Diorite sample represents a distinct intrusive phase, as supported by textural evidence, whole-rock chemistry (Figs. S3–S5; Meurer, 1992; Gilmer and Thompson, 2024), and zircon trace element chemistry (Figs. 4–6). This interpretation is consistent with earlier petrologic studies that documented multiple distinct phases of the Willow Spring Diorite (Otton, 1977; Meurer, 1992). The lower and middle Willow Spring Diorite zircon samples form linear trends in trace element ratios consistent with amphibole (clinopyroxene + biotite + accessory phases) and plagioclase fractionation (Figs. 5–6). This suggests that the lower and middle Willow Spring Diorite formed from in situ differentiation of the same magma source. Establishing the relationship between the upper Willow Spring Diorite and other units is more challenging due to the limited TIMS-TEA analyses available for the upper Willow Spring Diorite.

Willow Spring Diorite samples were collected from different structural levels of the east-tilted footwall of the Black Mountains (inset in Fig. 7). By comparing the structural level of each Willow Spring Diorite sample with its emplacement age, or zircon solidus age, we can elucidate the emplacement history of the Willow Spring Diorite. Despite our small sample size, we observe a trend of younger emplacement ages at structurally higher levels. The sample we collected from the lowest structural level has the oldest emplacement age. Emplacement ages become progressively younger at structurally higher levels, suggesting that phases of the Willow Spring Diorite represent a sequence of vertically stacked sills. The mylonitized lowermost part of the Willow Spring Diorite was not sampled.

The felsic plutons of the Black Mountains intrusive complex, the Smith Mountain Granite and quartz monzonite of Gold Valley, began crystallizing zircon at $10.81^{+0.20}/_{-0.21}$ Ma and $10.82^{+0.16}/_{-0.10}$ Ma, respectively, coeval with the middle and upper Willow Spring Diorite. The Smith Mountain Granite crystallized zircon for 580 k.y. while the quartz monzonite of Gold

Valley crystallized zircon for 640 k.y., indicating that the felsic plutons formed over similar time scales. Previous U-Pb zircon data sets suggested that Willow Spring Diorite was significantly older than the Smith Mountain Granite (Asmerom et al., 1990; Miller et al., 2004). However, our new U-Pb data set demonstrates that all intrusions of the Black Mountains intrusive complex crystallized simultaneously, with compositionally distinct magmas crystallizing at the same time. There is field evidence of magma intermingling between the Willow Spring Diorite and quartz monzonite of Gold Valley (see Supplemental Material; Meurer, 1992)

Zircon trace element ratios and fractionation trends in the Smith Mountain Granite and quartz monzonite of Gold Valley overlap with each other and with those of several Willow Spring Diorite samples (Figs. 4–6). These trends are consistent with a comagmatic relationship, which can be further investigated by examining published whole-rock data (Figs. S3–S5; Gilmer and Thompson, 2024). If the Black Mountains intrusive complex is part of a single magmatic system, then the felsic plutons would be fractionated melts, while the Willow Spring Diorite would represent the cumulate material. Chemical tracers for plagioclase (e.g., Eu/Eu*) and amphibole (e.g., La/Yb and Dy/Yb) crystallization do not show linear trends between the dioritic and felsic intrusions, indicating that the latter cannot be derived solely from the differentiation of Willow Spring Diorite magmas (Fig. S5). This conclusion aligns with Meurer's (1992) findings and is further supported by the absence of cumulate textures in the Willow Spring Diorite. However, this does not negate the possibility that the Smith Mountain Granite and quartz monzonite of Gold Valley are petrogenetically related, given that the latter may represent a northern continuation of the Smith Mountain Granite, a hypothesis originally proposed by Holm et al. (1992) now supported by our geochronologic and new geochemical data.

The Black Mountains intrusive complex was emplaced into the middle crust. Crystallization pressures for the Willow Spring Diorite, determined using Al-in-hornblende barometry on a leucocratic phase, range from 260 MPa to 280 MPa. This indicates a minimum emplacement depth of ~10 km, based on a bulk crustal density of 2700 kg/m^3 (Meurer, 1992; Holm et al., 1992). Emplacement depths increase to the northwest, suggesting exhumation along an initially steeply dipping fault (Meurer, 1992; Miller and Pavlis, 2005). Al-in-hornblende geobarometry from the Smith Mountain Granite also indicates crystallization at a depth of at least 10 km (Holm et al., 1992). Recent garnet thermobarometry of the turtlebacks indicates temperatures of 660–685 °C and pressures of 500–600 MPa during the Miocene, suggesting that the Willow Spring Diorite was emplaced at even greater depths, closer to 15–20 km (Pavlis et al., 2018; Fleming et al., 2022). Although there are no published geobarometry data for the quartz monzonite of Gold Valley, overlapping zircon crystallization ages (Fig. 3) and mutually intrusive contacts with both the Willow Spring Diorite and Smith Mountain Granite imply that the quartz monzonite crystallized at a similar structural level.

Phase III: Late Plutonism in the Black Mountains and Greenwater Range (P3)

A younger phase of intrusive magmatism, phase III (P3), commenced with the emplacement of the granite of Deadman Pass in the Greenwater Range, where zircon crystallization initiated at 8.176 $^{+0.111}/_{-0.019}$ Ma and continued for ~309 k.y. (Fig. 7; Table 4). While this granite is chemically similar to other Greenwater Range intrusions (Figs. S3– S5; Calzia and Rämö, 2005; Gilmer and Thompson, 2024), isotopic differences suggest distinct magma sources for the granite of Deadman Pass (Calzia et al., 2016). Additionally, zircon chemistry indicates that the granite of Deadman Pass crystallized from a more evolved magma than other felsic plutons in the Black Mountains intrusive complex (Figs. 4–6).

Concurrently, zircon crystallization began at 7.902 $^{+0.057}/_{-0.015}$ Ma in the diorite of Furnace Site (Fig. 3; Table 4). Although previously mapped as the Willow Spring Diorite (Otton, 1977; Holm and Wernicke, 1990), the diorite of Furnace Site has younger zircon crystallization ages and higher zircon Th/U ratios (>1.5), indicating it is distinct from the Willow Spring Diorite magmatic system. The diorite of Furnace Site zircon grains are compositionally diverse (e.g., Zr/Hf, Yb/Dy, and Eu/Eu* ratios and Hf content; Figs. 5–6), which means either that these zircons crystallized in discrete melt bodies that were mixed prior to emplacement or that magma differentiation occurred on time scales significantly shorter than those of zircon growth.

Synthesis of Magmatism and Tectonic Activity in Death Valley

The volcanic and plutonic record of Death Valley over the past 16 m.y. offers crucial insights into the development of this tectonically complex region. In this section, we integrate new geochronology from Miocene plutonic rocks, existing volcanic records, and documented tectonic events to examine the spatiotemporal relationship between extension and magmatism. Our compilation in Figure 8 defines six different volcanic episodes (V1–V6; Calzia and Rämö, 2000; Fridrich and Thompson, 2011), three phases of intrusive magmatism (P1–P3; Fig. 7), and four major tectonic stages (T1–T4; Wernicke et al., 1988; Wright et al., 1991; Wernicke, 1992; Holm and Dokka, 1993; Davis et al., 1993; Topping, 1993; Miller and Friedman, 1999; McQuarrie and Wernicke, 2005; Andrew and Walker, 2009; Fridrich and Thompson, 2011; Norton, 2011; Bidgoli et al., 2015; Sizemore et al., 2019; Fleming et al., 2021).

Detachment faulting in the Death Valley region initiated ca. 16–15 Ma, characterized by large-magnitude WSW-directed extension along the Kingston Range–Halloran Hills–Spring Mountains detachment (T1; Burchfiel et al., 1983; Davis et al., 1993; Fowler et al., 1995; Friedmann et al., 1996; Andrew and Walker, 2009). This period also saw WNW-directed extension along several other detachment faults in the Bare Mountain, Bullfrog Hills, and Funeral Mountains (e.g., Hamilton, 1988; Hodges et al., 1989; Hoisch et al., 1997; Fridrich et al., 1999; Fridrich and Thompson, 2011; Lutz et al., 2021). Slip along the Kingston Range–Halloran Hills detachment is bracketed between 13.4 Ma, based on a sill intruded during faulting (K-Ar hornblende; Davis et al., 1993), and 12.4 Ma, which is the published age for the Kingston Range Granite (Calzia, 1990; Fowler and Calzia, 1999). However, new U-Pb zircon ages for the Kingston Range Granite provide a revised minimum of 13.2 Ma for the timing of extension along this detachment.

Magmatism in the region (V1) initiated at ca. 15 Ma with the eruption of several calc-alkaline stratovolcano complexes and associated small intrusive domes in the Wingate Wash–Owlshead Mountains (Fig. 8; e.g., Burchfiel and Davis, 1988; Wagner, 1988; Calzia, 1990; McKenna and Hodges, 1990; Calzia and Rämö, 2000; Niemi et al., 2001; Luckow et al., 2005). Waning volcanism coincided with emplacement of shallow rapakivi granites (P1), which includes the Kingston Range Granite, granite of Rabbit Holes Spring, Little Chief Granite (McDowell, 1974; Calzia, 1990), and the 13.2 ± 0.2 Ma Devil Peak intrusion (Table 2; Guest et al., 2007). Volcanism across the Death Valley region ceased between 12 Ma and 11 Ma (Luckow et al., 2005; Fridrich and Thompson, 2011), with only a few distal tuffs at this time.

The second phase of plutonic activity (P2) is associated with the Black Mountains intrusive complex at ca. 11.3 Ma. This phase lasted for at least 1.2 m.y. and is associated with WNW-directed extension (T2). Although a full tectonic reconstruction is beyond the scope of this project, it is clear that plutonic activity shifted westward, potentially with a minor northward component (e.g., Stewart, 1983; Wernicke et al., 1987; Topping, 1993; Serpa and Pavlis, 1996; Snow and Lux, 1999; Andrew, 2002, 2019; Miller and Prave, 2002; Miller and Pavlis, 2005;

Fleming et al., 2021), between ca. 13.2 Ma and 10 Ma (Fig. 7). During this period, extension is accommodated along a series of conjugate strike-slip faults, including NW-striking dextral faults such as the Southern Death Valley fault (e.g., Pavlis and Trullenque, 2021) and the sinistral SW-striking Garlock fault system (Fig. 2; e.g., Serpa and Pavlis, 1996; Andrew et al., 2015).

Major volcanism resumed by 11 Ma (V2) with bimodal compositions but transitioned to felsic-dominated compositions by 10 Ma with eruption of the ca. 11 Ma Sheephead Andesite, ca. 10.5 Ma Rhodes Tuff, and 10.3 Ma Trail Canyon volcanics (Fig. 8; Troxel and Wright, 1987; Wright et al., 1991; McKenna and Hodges, 1990; Calzia and Rämö, 2000; Fridrich and Thompson, 2011). Felsic-dominated volcanism coincided with peak plutonic activity, marked by the emplacement of the Black Mountains intrusive complex (P2). Given the proximity and overlapping ages of the felsic intrusions within the Black Mountains intrusive complex and nearby volcanic units, such as the 10.5 Ma Rhodes Tuff (Fridrich and Thompson, 2011), it is plausible that these felsic intrusions are the plutonic underpinning to some of these volcanic units.

There is a noticeable gap in zircon crystallization ages between 10.0 Ma and 8.2 Ma (Fig. 3), which may be attributed to several factors. One possibility is sampling bias, given that no rock samples were collected from a >90 km^2 area in the Black Mountains and large swaths of the Greenwater Range (Fig. 2), potentially leaving intrusions from this period unidentified or undated. Alternatively, younger sedimentary or volcanic rocks may have covered these intrusions, or these intrusions could have been eroded or removed tectonically. This gap might also imply a magmatic lull; however, the eruption of the 8.5–7.5 Ma Shoshone Volcanics in the Greenwater Range (V3; Wright et al., 1991) contradicts this idea.

The most likely explanation for the observed gap is a transition from sill to dike emplacement during this period. Several generations of latite and silicic dikes cut the turtleback shear zone and the intrusive complex, with some exhibiting ductile deformation (Drewes, 1963; Otton, 1977; Wright et al., 1991; Holm et al., 1992; Miller and Friedman, 1999; Dee et al., 2004). Limited geochronology indicates that diking occurred ca. 9.5–7.9 Ma (Holm et al., 1992; Miller and Friedman, 2003). This transition coincides with the solidification of the intrusive complex by 10 Ma (Fig. 3), followed by higher rates of exhumation and cooling (Holm et al., 1992; Holm and Dokka, 1993), reaching ~180 °C by 7.8 Ma (Topping, 1993).

Pluton emplacement resumed by ca. 8.2 Ma (P3), marked primarily by shallow granite intrusions in the Greenwater Range and a diorite intrusion in the northern Black Mountains. Intrusive magmatism appears to have shifted northward within the Black Mountains and Greenwater Range (Fig. 7). The northward age progression in the Greenwater Range is supported by older zircon ages in the Shoshone Granite (ca. 10 Ma laser ablation ICP-MS $^{206}Pb/^{238}U$; Rämö et al., 2011), which is located south of the granite of Deadman Pass. This reinitiation of sill-dominated emplacement coincides with the start of rapid extension (Holm et al., 1992; Holm and Dokka, 1993) and NW-directed dextral transtension (Bidgoli et al., 2015; Sizemore et al., 2019; Fleming et al., 2021). Similar to the Black Mountains, exhumation of the Greenwater Range was rapid enough to allow for erosion of the exhumed footwall prior to burial by the ca. 8.5 Ma Shoshone Volcanics (Wright et al., 1991).

Differences in the emplacement depths between the Willow Spring Diorite and the youngest granites in the region reveal significant tectonic changes over a short period of time. The 11.3 Ma Willow Spring Diorite and 10.8 Ma Smith Mountain Granite are the deepest intrusions, with emplacement depths exceeding 10 km and reaching as deep as 20 km (Pavlis et al., 2018; Fleming et al., 2022). The youngest granite, the 7.8 Ma granite of Deadman Pass, has

hypabyssal textures (Haefner, 1972) and is interpreted to have been emplaced shallowly. This implies that there was a profound change in the emplacement depth in a relatively small region of footwall rocks between 10 Ma and 8.2 Ma, which requires rapid tectonic exhumation during this time interval (McKenna and Hodges, 1990; Holm and Dokka, 1993; Topping, 1993; Bidgoli et al., 2015; Sizemore et al., 2019).

Large-magnitude dextral transtension (T3) commenced ca. 8–7 Ma, leading to a period of rapid extension that continued until ca. 4.5 Ma (Topping, 1993; Bidgoli et al., 2015; Sizemore et al., 2019). Transtension may have initiated as early as 10 Ma (e.g., Renik and Christie-Blick, 2013). However, dextral slip observed on NW-striking faults between 10 Ma and 8 Ma could also indicate continued west-directed extension within a conjugate strike-slip system. This system includes the dextral NW-striking Las Vegas Valley shear zone, located east of the Spring Mountains (Fig. 2; Çakir et al., 1998) and the sinistral SW-striking Garlock fault (Andrew et al., 2015), whose combined initial geometries and sense of shear suggests continued east-west extension. Dextral transtension contributed to the exhumation of the Black Mountains through the formation of pull-apart basins located between the Furnace Creek and Southern Death Valley–Sheephead fault zones to the north and south, respectively (Fig. 2; e.g., Troxel and Wright, 1987; Serpa and Pavlis, 1996; Miller and Prave, 2002).

No plutonic activity has been documented in T3; however, basaltic volcanism (V4) continued in the Greenwater Range with the eruption of the ca. 7–5 Ma Greenwater Volcanics (Wright et al., 1991; Calzia et al., 2016). This was followed by ~1 m.y. period of flood basalts (V5), including the ca. 5 Ma Funeral Creek basalts and ca. 6-4 Ma Nova Formation basalts in the northern Panamint Mountains and Darwin Plateau (e.g., McAllister, 1970, 1973; Troxel and Wright, 1987; Hodges et al., 1989; Coleman 788 and Walker, 1990; Snyder and Hodges, 2000). Small-volume basaltic eruptions (V6) continue into the present with the eruption of the 1.5 Ma Shoreline Butte basalts and <1 Ma cinder cones (de Voogd et al., 1986; Wright et al., 1991; Fridrich and Thompson, 2011) and minor rhyolitic eruptions of the 3.6 Ma to ca. 32 ka Mesquite Spring tuff (e.g., Snow and White, 1990; Knott et al., 1999, 2018; Fridrich and Thompson, 2011).

Although no mid-crustal plutons have been identified after P3, young basaltic eruptions and Consortium for Continental Reflection Profiling (COCORP) deep seismic reflection profiles from central Death Valley underscore the existence of a mid-crustal magmatic system below modern-day southern Death Valley (de Voogd et al., 1986; Serpa et al., 1988). This localization of ongoing magmatism may relate to ongoing extensional deformation in this region, which is supported by Holocene slip along the Amargosa–Black Mountains detachment fault (Knott et al., 1999, p. 199; Hayman et al., 2003). However, the main locus of extension shifted west of the study area to the Panamint Valley and Owens Vally fault systems by ca. 4.5 Ma (Knott et al., 1999, 2005; Hayman et al., 2003; Stockli et al., 2003; Andrew and Walker, 2009; Frankel et al., 2016).

Implications of Late Miocene Rapakivi Granites in Death Valley

Rapakivi textures, characterized by potassium feldspar megacrysts rimmed by plagioclase feldspar, are prevalent in all the Miocene felsic plutons in the Death Valley region (this study; McDowell, 1978; Meurer, 1992; Calzia and Rämö, 2005; Calzia et al., 2016). Rapakivi granites typically crystallize from hot, fractionated, magmas (650–950 °C; e.g., Rämö and Haapala, 1995). The atypical progression from alkali feldspar to plagioclase crystallization can be attributed to two main mechanisms (Vernon, 2016): (1) mixing of mafic and felsic magmas (e.g., Hibbard, 1981; Bussy, 1990; Wark and Stimac, 1992; Andersson and Eklund, 1994) and (2)

778 adiabatic decompression (e.g., Nekvasil, 1991; Eklund and Shebanov, 1999). These processes
779 are likely interconnected, given that hot mantle input can sustain high temperatures during
780 adiabatic decompression. This section examines how these mechanisms contribute to the
781 prevalence of rapakivi granites in Death Valley.
782 Magma mixing can lead to two outcomes: (1) hot mafic magma may partially dissolve
783 potassium feldspar megacrysts and crystallize new plagioclase rims, or (2) the injection of new
784 felsic magma can form plagioclase rims around the potassium feldspar (e.g., Hibbard, 1981;
785 Bussy, 1990; Wark and Stimac, 1992; Andersson and Eklund, 1994). This process may occur in
786 both deep and shallow plutonic rocks in Death Valley. In the Black Mountains intrusive
787 complex, magma mingling textures and isotopic heterogeneities on a tens-of-meters scale are
788 indicative of magma mixing (Asmerom et al., 1990; Meurer, 1992; Holm et al., 1994b; Miller et
789 al., 2004). Additionally, shallow rapakivi granites (P1 and P3), containing mafic xenoliths and
790 inclusions, show geochemical and isotopic signatures that suggest partial melting of the lower
791 crust with juvenile mantle contributions (Calzia and Rämö, 2005).
792 During adiabatic decompression, potassium feldspar megacrysts crystallize in felsic
793 magmas at mid-crustal depths and are transported in a crystal mush to shallower levels (e.g.,
794 Annen et al., 2015; Sparks et al., 2019). Decompression alters the solidus and shifts the two-
795 feldspar stability boundary, favoring plagioclase crystallization (e.g., Nekvasil, 1991; Eklund and
796 Shebanov, 1999). This model aligns well with the shallow (<4 km) Miocene plutons in the
797 Kingston, Greenwater, and Panamint Ranges (Haefner, 1972; McDowell, 1974; Calzia, 1990;
798 Calzia and Rämö, 2005). In contrast, felsic plutons in the Black Mountains were emplaced in the
799 middle crust (>10 km; Holm et al., 1992; Pavlis et al., 2018; Fleming et al., 2022), so for the
800 decompression rapakivi texture mechanism to apply, these plutons would have required rapid
801 tectonic exhumation during late-stage crystallization.
802 Rapakivi textures are relatively rare in Tertiary granitoids, primarily documented in
803 Archean and Proterozoic granites (e.g., Rämö and Haapala, 1995). Aside from the rapakivi
804 granitoids in Death Valley, there are only two other documented Cenozoic intrusions with these
805 textures—the 48.1 Ma Golden Horn batholith in Washington (Stull, 1978; Eddy et al., 2016) and
806 the 17.4–15.3 Ma Spirit Mountain batholith of the Colorado River extensional corridor in
807 Nevada (Walker et al., 2007). Although magma mixing is a common magmatic process in the
808 formation of felsic plutons across various geologic settings, rapakivi textures are rare. The
809 distinctiveness of the young rapakivi granites in Death Valley and the Spirit Mountain batholith
810 suggests that specific factors, such as localized large-magnitude extension, may have played a
811 significant role in their formation.
812 We argue that rapid extension of an overthickened crust (≥30 km; e.g., Holm and
813 Wernicke, 1990; Pavlis et al., 2018) is an important factor for generating rapakivi textures. This
814 process likely led to adiabatic decompression, magmatic underplating, and anatexis of the lower
815 crust (Fountain, 1989; Calzia and Rämö, 2005), driving the formation of these textures. Notably,
816 there are striking similarities between the extensional tectonics of Death Valley and that of
817 Proterozoic rapakivi granites in Finland and Greenland (e.g., Haapala and Rämö, 1990, 1992;
818 Brown et al., 1992, 2003; Rämö and Haapala, 1995; Ahl et al., 1999; Haapala et al., 2005),
819 suggesting a link between extensional tectonics and rapakivi textures. While we cannot rule out
820 the magma mixing model, the decompression model fits well within the tectonic framework of a
821 highly extended region (Fig. 8). Further petrologic and geochemical studies are necessary to
822 validate this hypothesis.
823 ***How Does Death Valley Fit into the Late Cenozoic Magmatic Trends in the Basin and Range?***

Late Cenozoic magmatism in Death Valley is a continuation of the northward-migrating magmatic trend from the Colorado River extensional corridor (Fig. 1; Christiansen et al., 1992; Faulds et al., 2001). These two regions are separated by the ~65 km WSW-striking left-lateral Lake Mead fault zone, which became active after ca. 12.7 Ma. In the Colorado River extensional corridor, the principal extension direction is ENE, whereas in Death Valley, WSW-directed extension is observed along the Kingston Range–Halloran Hills detachment. Subsequently, the principal extension direction shifts to WNW, which is documented in the Amargosa-Black Mountains, Funeral Mountains, and Bare Mountain detachment faults. Changes in the extension polarity along strike are common in extensional rifts (e.g., Lister et al., 1986; Péron-Pinvidic et al., 2017; Balázs et al., 2018).

Similar to those in Death Valley, the plutons of the Colorado River extensional corridor have a narrower age range (17–13 Ma) compared to the volcanic rocks (Faulds et al., 2001). Most of plutons in the extensional corridor were emplaced within 200–500 k.y. of local extension and transitioned from sill emplacement to north-south dike swarms within <400 k.y. after pluton solidification in the northern region (e.g., Spirit Mountain batholith; Miller et al., 2011). Extension typically occurred ~700 k.y. after the northward-migrating pulse of magmatism reached a given area (Gans and Bohrson, 1998).

The northward migration of the Arizona magmatic trend is tectonically linked with the migration of the Mendocino triple junction (e.g., Crough and Thompson, 1977; Best and Hamblin, 1978; Dickinson and Snyder, 1979; Atwater and Stock, 1998; Zandt and Humphreys, 2008). This contrasts with the southward-migrating Nevada magmatic trend, which is associated with slab rollback (e.g., Coney, 1978; Lipman, 1980; Best and Christiansen, 1991). As the northward-migrating Mendocino transform boundary—interpreted as the driver of the northward Arizona magmatic trend—passed across the Death Valley region, slab rollback would have ceased. This aligns with the notable similarities observed between the Death Valley and Colorado River extensional corridors. This shift in tectonic activity highlights the complex interplay between magmatism and tectonic forces in the Death Valley region.

CONCLUSIONS

U-Pb zircon geochronology identifies three distinct pulses of Late Cenozoic plutonism in the Death Valley region, beginning with the emplacement of shallow rapakivi granites at ca. 13.2 Ma and lasting for 1.85 m.y. Plutonic activity peaked at 10.5 Ma with the simultaneous crystallization of three mid-crustal plutons associated with the Black Mountains intrusive complex—Willow Spring Diorite, Smith Mountain Granite, and quartz monzonite of Gold Valley. Whole-rock geochemical tracers (e.g., Eu/Eu*, La/Yb, Dy/Yb) indicate that the Smith Mountain Granite and quartz monzonite of Gold Valley are comagmatic but not derived from differentiation of the Willow Spring Diorite. Emplacement ages indicate that the Willow Spring Diorite formed as a sequence of incrementally emplaced, vertically stacked sills.

Zircon crystallization ages reveal continuous intrusive magmatism between 13.2 Ma and 10 Ma, followed by a gap in zircon crystallization that coincides with rapid exhumation of the Black Mountains and a transition from sill to dike emplacement. Late-stage plutonism at 8.2 Ma featured shallow, compositionally diverse intrusions, including the diorite of Furnace Site, which is distinct from the Willow Spring Diorite in U-Pb ages, texture, and zircon trace element ratios (e.g., Th/U, Lu/Hf). Most Death Valley plutons formed incrementally over timescales of 105–106 yr, although a few were constructed instantaneously within the age resolution of CA-ID-TIMS dating. A significant change in emplacement depth between the Willow Spring Diorite and the granite of Deadman Pass reflects rapid tectonic exhumation between 10 Ma and 8.2 Ma,

supported by overlapping or closely aligned zircon crystallization ages and published cooling ages.

Late Cenozoic plutonism fits within the broader volcanic history of the region. The spatial and temporal distribution of plutonism and tectonic events from ca. 15 Ma to 8 Ma indicates that plutonism occurred synchronously with major extensional events. The important link between extension and plutonism is further emphasized by the prevalence of rapakivi textures in Miocene felsic plutons of Death Valley, an uncommon feature in Cenozoic plutons globally. These textures are primarily attributed of adiabatic decompression during rapid, large-magnitude tectonic extension. Rapid extension of an overthickened crust (>30 km) is likely a key factor in the generation of rapakivi granitoids in Death Valley.

ACKNOWLEDGMENTS

This project was supported by grants from the Geological Society of America and University of Kansas Department of Geology to C. Chan and by the U.S. Geological Survey's National Cooperative Geologic Mapping Program. We thank the National Park Service for allowing us to collect rock samples. We are very appreciative to Ren Thompson and Amy Gilmer for sharing their Death Valley expertise, providing insightful discussions, giving expert assistance in the field, and sharing a diorite of Furnace Site sample. We also thank James Calzia for the granite of Rabbit Holes Spring samples and Tandis Bidgoli for the Kingston Range Granite feldspar porphyry sample. We would like to acknowledge Nicholas Hayman, an anonymous reviewer, and Associate Editor Terry Pavlis for their thoughtful reviews, and Christopher Spencer for editorial handling. Part of this work was performed under the auspices of the U.S. Department of Energy by Lawrence Livermore National Laboratory under contract DE-AC52-07NA27344, release number LLNL-JRNL-862151.

REFERENCES CITED

Ahl, M., Sundblad, K., and Schöberg, H., 1999, Geology, geochemistry, age and geotectonic evolution of the Dala granitoids, central Sweden: Precambrian Research, v. 95, p. 147–166, https://doi.org/10.1016/S0301-9268(98)00131-4.

Almashoor, S.S., 1983, The petrology of a quartz monzonite pluton in the southern Greenwater Range, Inyo County, California [Ph.D. Thesis]: Pennsylvania State University, 155 p.

Andersson, U.B., and Eklund, O., 1994, Cellular plagioclase intergrowths as a result of crystal-magma mixing in the Proterozoic land rapakivi batholith, SW Finland: Contributions to Mineralogy and Petrology, v. 117, p. 124–136, https://doi.org/10.1007/BF00286837.

Andrew, J.E., 2002, The Mesozoic and Tertiary tectonic his- tory of the Panamint Range and Quail Mountains, California [Ph.D. Thesis]: Lawrence, Kansas, USA, University of Kansas, 154 p.

Andrew, J.E., 2019, Deciphering the polyphase tectonic evolution of the Jurassic-Cretaceous arc in the Death Valley region by revisiting the enigmatic Butte Valley fault, Panamint Range, California: Geological Society of America Abstracts with Programs v. 51, no. 5, https://doi.org/10.1130/abs/2019AM-339194.

Andrew, J.E., and Walker, J.D., 2009, Reconstructing late Cenozoic deformation in central Panamint Valley, California: Evolution of slip partitioning in the Walker Lane: Geosphere, v. 5, p. 172–198, https://doi.org/10.1130/GES00178.1.

Andrew, J.E., Walker, J.D., and Monastero, F.C., 2015, Evolution of the central Garlock fault zone, California: A major sinistral fault embedded in a dextral plate margin: Geological Society of America Bulletin, v. 127, p. 227–249, https://doi.org/10.1130/B31027.1.

915 Annen, C., Blundy, J.D., Leuthold, J., and Sparks, R.S.J., 2015, Construction and evolution of
916 igneous bodies: Towards an integrated perspective of crustal magmatism: Lithos, v. 230,
917 p. 206–221, https://doi.org/10.1016/j.lithos.2015.05.008.
918 Armstrong, R.L., and Ward, P., 1991, Evolving geographic patterns of Cenozoic magmatism in
919 the North American Cordillera: The temporal and spatial association of magmatism and
920 metamorphic core complexes: Journal of Geophysical Research: Solid Earth, v. 96,
921 p. 13,201–13,224, https://doi.org/10.1029/91JB00412.
922 Asmerom, Y., Snow, J.K., Holm, D.K., Jacobsen, S.B., Wernicke, B.P., and Lux, D.R., 1990,
923 Rapid uplift and crustal growth in extensional environments: An isotopic study from the
924 Death Valley region, California: Geology, v. 18, p. 223–226, https://doi.org/10.1130/0091-
925 7613(1990)018<0223:RUACGI>2.3.CO;2.
926 Atwater, T., and Stock, J., 1998, Pacific-North America plate tectonics of the Neogene
927 southwestern United States: An update: International Geology Review, v. 40, p. 375–402,
928 https://doi.org/10.1080/00206819809465216.
929 Axen, G.J., 2020, How a strong low-angle normal fault formed: The Whipple detachment,
930 southeastern California: Geological Society of America Bulletin, v. 132, p. 1817–1828,
931 https://doi.org/10.1130/B35386.1.
932 Bachmann, O., Oberli, F., Dungan, M.A., Meier, M., Mundil, R., and Fischer, H., 2007,
933 $^{40}Ar/^{39}Ar$ and U–Pb dating of the Fish Canyon magmatic system, San Juan Volcanic field,
934 Colorado: Evidence for an extended crystallization history: Chemical Geology, v. 236,
935 p. 134–166, https://doi.org/10.1016/j.chemgeo.2006.09.005.
936 Balázs, A., Matenco, L., Vogt, K., Cloetingh, S., and Gerya, T., 2018, Extensional polarity
937 change in continental rifts: Inferences from 3-D numerical modeling and observations:
938 Journal of Geophysical Research: Solid Earth, v. 123, p. 8073–8094,
939 https://doi.org/10.1029/2018JB015643.
940 Bea, F., Montero, P., Molina, J.F., Scarrow, J.H., Cambeses, A., and Moreno, J.A., 2018, Lu-Hf
941 ratios of crustal rocks and their bearing on zircon Hf isotope model ages: The effects of
942 accessories: Chemical Geology, v. 484, p. 179–190,
943 https://doi.org/10.1016/j.chemgeo.2017.11.034.
944 Best, M.G., and Brimhall, W.H., 1974, Late Cenozoic alkalic basaltic magmas in the western
945 Colorado Plateaus and the Basin and Range transition zone, U.S.A., and their bearing on
946 mantle dynamics: Geological Society of America Bulletin, v. 85, p. 1677–1690,
947 https://doi.org/10.1130/0016-7606(1974)85<1677:LCABMI>2.0.CO;2.
948 Best, M.G., and Christiansen, E.H., 1991, Limited extension during peak Tertiary volcanism,
949 Great Basin of Nevada and Utah: Journal of Geophysical Research: Solid Earth, v. 96,
950 p. 13,509–13,528, https://doi.org/10.1029/91JB00244.
951 Best, M.G., and Hamblin, W.K., 1978, Origin of the northern Basin and Range province:
952 Implications from the geology of its eastern boundary, *in* Smith, R.B., and Eaton, G.P., eds.,
953 Cenozoic Tectonics and Regional Geophysics of the Western Cordillera: Geological Society
954 of America Memoir 152, p. 313–340, https://doi.org/10.1130/MEM152-p313.
955 Best, M.G., Gromme, S., Deino, A.L., Christiansen, E.H., Hart, G.L., and Tingey, D.G., 2013,
956 The 36–18 Ma Central Nevada ignimbrite field and calderas, Great Basin, USA: Multicyclic
957 super-eruptions: Geosphere, v. 9, p. 1562–1636, https://doi.org/10.1130/GES00945.1.
958 Best, M.G., Christiansen, E.H., de Silva, S., and Lipman, P.W., 2016, Slab-rollback ignimbrite
959 flareups in the southern Great Basin and other Cenozoic American arcs: A distinct style of
960 arc volcanism: Geosphere, v. 12, p. 1097–1135, https://doi.org/10.1130/GES01285.1.

961 Bidgoli, T.S., Amir, E., Walker, J.D., Stockli, D.F., Andrew, J.E., and Caskey, S.J., 2015, Low-
962 temperature thermochronology of the Black and Panamint mountains, Death Valley,
963 California: Implications for geodynamic controls on Cenozoic intraplate strain: Lithosphere,
964 v. 7, p. 473–480, https://doi.org/10.1130/L406.1.
965 Bindeman, I.N., Schmitt, A.K., and Valley, J.W., 2006, U–Pb zircon geochronology of silicic
966 tuffs from the Timber Mountain/Oasis Valley caldera complex, Nevada: Rapid generation of
967 large volume magmas by shallow-level remelting: Contributions to Mineralogy and
968 Petrology, v. 152, p. 649–665, https://doi.org/10.1007/s00410-006-0124-1.
969 Boehnke, P., Watson, E.B., Trail, D., Harrison, T.M., and Schmitt, A.K., 2013, Zircon saturation
970 re-revisited: Chemical Geology, v. 351, p. 324–334,
971 https://doi.org/10.1016/j.chemgeo.2013.05.028.
972 Bowring, J.F., McLean, N.M., and Bowring, S.A., 2011, Engineering cyber infrastructure for U-
973 Pb geochronology: Tripoli and U-Pb_Redux: Geochemistry, Geophysics, Geosystems, v. 12,
974 https://doi.org/10.1029/2010GC003479.
975 Brown, P.E., Dempster, T.J., Harrison, T.N., and Hutton, D.H.W., 1992, The rapakivi granites of
976 S Greenland—Crustal melting in response to extensional tectonics and magmatic
977 underplating: Earth and Environmental Science Transactions of the Royal Society of
978 Edinburgh, v. 83, p. 173–178, https://doi.org/10.1017/S0263593300007860.
979 Brown, P.E., Dempster, T.J., Hutton, D.H.W., and Becker, S.M., 2003, Extensional tectonics and
980 mafic plutons in the Ketilidian rapakivi granite suite of South Greenland: Lithos, v. 67, p. 1–
981 13, https://doi.org/10.1016/S0024-4937(02)00212-8.
982 Burchfiel, B.C., and Davis, G.A., 1988, Mesozoic thrust faults and Cenozoic low-angle normal
983 faults, eastern Spring Mountains, Nevada, and Clark Mountains thrust complex, California,
984 *in* Weide, D.L., and Faber, M.L., eds., This Extended Land: Geological Journeys in the
985 Southern Basin and Range: Field Trip Guidebook, Geological Society of America,
986 Cordilleran Section Meeting: Las Vegas, University of Nevada, Department of Geoscience,
987 p. 87–106.
988 Burchfiel, B.C., and Stewart, J.H., 1966, "Pull-apart" origin of the central segment of Death
989 Valley, California: Geological Society of America Bulletin, v. 77, p. 439–442,
990 https://doi.org/10.1130/0016-7606(1966)77[439:POOTCS]2.0.CO;2.
991 Burchfiel, B.C., Hamill, G.S., and Wilhelms, D.E., 1983, Structural geology of the Montgomery
992 Mountains and the northern half of the Nopah and Resting Spring Ranges, Nevada and
993 California: Geological Society of America Bulletin, v. 94, p. 1359–1376,
994 https://doi.org/10.1130/0016-7606(1983)94<1359:SGOTMM>2.0.CO;2.
995 Burchfiel, B.C., Hodges, K.V., and Royden, L.H., 1987, Geology of the Panamint Valley–Saline
996 Valley pull-apart system, California: Palinspastic evidence for low-angle geometry of a
997 Neogene range-bounding fault: Journal of Geophysical Research: Solid Earth, v. 92,
998 p. 10,422–10,426, https://doi.org/10.1029/JB092iB10p10422.
999 Bussy, F., 1990, The rapakivi texture of feldspars in a plutonic mixing environment: A
1000 dissolution-recrystallization process?: Geological Journal, v. 25, p. 319–324,
1001 https://doi.org/10.1002/gj.3350250314.
1002 Çakir, M., Aydin, A., and Campagna, D.J., 1998, Deformation pattern around the conjoining
1003 strike-slip fault systems in the Basin and Range, southeast Nevada: The role of strike-slip
1004 faulting in basin formation and inversion: Tectonics, v. 17, p. 344–359,
1005 https://doi.org/10.1029/98TC00562.

1006 Calzia, J.P., 1990, Geologic studies in the Kingston Range, southern Death Valley region,
1007 California [Ph.D. Thesis]: Davis, California, USA, University of California, Davis, 230 p.
1008 Calzia, J.P., and Rämö, O.T., 2000, Late Cenozoic crustal extension and magmatism, southern
1009 Death Valley region, California, *in* Lageson, D.R., Peters, S.G., and Lahren, M.M., eds.,
1010 Great Basin and Sierra Nevada: Geological Society of America Field Guide 2, p. 135–164,
1011 https://doi.org/10.1130/0-8137-0002-7.135.
1012 Calzia, J.P., and Rämö, O.T., 2005, Miocene rapakivi granites in the southern Death Valley
1013 region, California, USA: Earth-Science Reviews, v. 73, p. 221–243,
1014 https://doi.org/10.1016/j.earscirev.2005.07.006.
1015 Calzia, J.P., Troxel, B.W., Burchfiel, B.C., Davis, G.A., and McMackin, M.R., 2000, Geologic
1016 map of the Kingston Range, southern Death Valley, California: U.S. Geological Survey
1017 Open-File Report 2000-412, 2 sheets, scale 1:31,680, https://doi.org/10.3133/ofr00412.
1018 Calzia, J.P., Troxel, B.W., and Raumann, C.G., 2003, Geologic map of the Valjean Hills 7.5′
1019 quadrangle, San Bernardino County, California: U.S. Geological Survey Open-File Report
1020 2003-96, scale 1:24,000, https://doi.org/10.3133/ofr0396.
1021 Calzia, J.P., Rämö, O.T., Jachens, R., Smith, E., and Knott, J., 2016, Geology of the Greenwater
1022 Range, and the dawn of Death Valley, California—Field guide for the Death Valley Natural
1023 History Conference, 2013: U.S. Geological Survey Open-File Report 2016-1064, 32 p.,
1024 https://doi.org/10.3133/ofr20161064.
1025 Cantagrel, J.-M., Didier, J., and Gourgaud, A., 1984, Magma mixing: Origin of intermediate
1026 rocks and "enclaves" from volcanism to plutonism: Physics of the Earth and Planetary
1027 Interiors, v. 35, p. 63–76, https://doi.org/10.1016/0031-9201(84)90034-7.
1028 Çemen, I., Tekeli, O., Seyitoğlu, G., and Isik, V., 2005, Are turtleback fault surfaces common
1029 structural elements of highly extended terranes?: Earth-Science Reviews, v. 73, p. 139–148,
1030 https://doi.org/10.1016/j.earscirev.2005.07.001.
1031 Cesare, B., Gómez-Pugnaire, M.T., and Rubatto, D., 2003, Residence time of S-type anatectic
1032 magmas beneath the Neogene Volcanic Province of SE Spain: A zircon and monazite
1033 SHRIMP study: Contributions to Mineralogy and Petrology, v. 146, p. 28–43,
1034 https://doi.org/10.1007/s00410-003-0490-x.
1035 Christiansen, R.L., Yeats, R.S., Graham, S.A., Niem, W.A., Niem, A.R., and Snavely, P.D., Jr.,
1036 1992, Post-Laramide geology of the U.S. Cordilleran region, *in* Burchfiel, B.C., Lipman,
1037 P.W., and Zoback, M.L., eds., The Cordilleran Orogen: Conterminous U.S.: Boulder,
1038 Colorado, Geological Society of America, Geology of North America, v. G3, p. 261–406,
1039 https://doi.org/10.1130/DNAG-GNA-G3.261.
1040 Coleman, D.S., and Walker, J.D., 1990, Geochemistry of Mio-Pliocene volcanic rocks from
1041 around Panamint Valley, Death Valley area, California, *in* Wernicke, B.P., ed., Basin and
1042 Range Extensional Tectonics Near the Latitude of Las Vegas, Nevada: Geological Society
1043 of America Memoir 176, p. 391–412, https://doi.org/10.1130/MEM176-p391.
1044 Colgan, J.P., Dumitru, T.A., Reiners, P.W., Wooden, J.L., and Miller, E.L., 2006, Cenozoic
1045 tectonic evolution of the Basin and Range Province in northwestern Nevada: American
1046 Journal of Science, v. 306, p. 616–654, https://doi.org/10.2475/08.2006.02.
1047 Condon, D.J., Schoene, B., McLean, N.M., Bowring, S.A., and Parrish, R.R., 2015, Metrology
1048 and traceability of U–Pb isotope dilution geochronology (EARTHTIME Tracer Calibration
1049 Part I): Geochimica et Cosmochimica Acta, v. 164, p. 464–480,
1050 https://doi.org/10.1016/j.gca.2015.05.026.

1051 Coney, P.J., 1978, Mesozoic-Cenozoic Cordilleran plate tectonics, *in* Smith, R.B., and Eaton,
1052 G.P., eds., Cenozoic Tectonics and Regional Geophysics of the Western Cordillera:
1053 Geological Society of America Memoir 152, p. 33–50, https://doi.org/10.1130/MEM152-
1054 p33.
1055 Crough, S.T., and Thompson, G.A., 1977, Upper mantle origin of Sierra Nevada uplift: Geology,
1056 v. 5, p. 396–399, https://doi.org/10.1130/0091-7613(1977)5<396:UMOOSN>2.0.CO;2.
1057 Curry, H.D., 1938, Turtleback fault surfaces in Death Valley, California: Geological Society of
1058 America Bulletin, v. 49, p. 1875.
1059 Curry, H.D., 1954, Turtlebacks in the central Black Mountains, Death Valley, California, *in*
1060 Jahns, R.H., ed., Geology of Southern California: California Division of Mines Bulletin 170,
1061 Ch. IV, p. 53–59.
1062 Davis, G.A., Fowler, T.K., Bishop, K.M., Brudos, T.C., Friedmann, S.J., Burbank, D.W., Parke,
1063 M.A., and Burchfiel, B.C., 1993, Pluton pinning of an active Miocene detachment fault
1064 system, eastern Mojave Desert, California: Geology, v. 21, p. 627–630,
1065 https://doi.org/10.1130/0091-7613(1993)021<0627:PPOAAM>2.3.CO;2.
1066 Dee, S., Miller, M., and Friedman, R.M., 2004, Pre- and post 9.5 Ma shear zone activity at the
1067 Mormon Point turtleback, Death Valley, California: Geological Society of America
1068 Abstracts with Programs, v. 35, no. 5.
1069 de Voogd, B., Serpa, L., Brown, L., Hauser, E., Kaufman, S., Oliver, J., Troxel, B.W., Willemin,
1070 J., and Wright, L.A., 1986, Death Valley bright spot: A midcrustal magma body in the
1071 southern Great Basin, California?: Geology, v. 14, p. 64–67, https://doi.org/10.1130/0091-
1072 7613(1986)14<64:DVBSAM>2.0.CO;2.
1073 Dickinson, J.E., and Hess, P.C., 1982, Zircon saturation in lunar basalts and granites: Earth and
1074 Planetary Science Letters, v. 57, p. 336–344, https://doi.org/10.1016/0012-821X(82)90154-
1075 6.
1076 Dickinson, W.R., and Snyder, W.S., 1979, Geometry of subducted slabs related to San Andreas
1077 transform: The Journal of Geology, v. 87, p. 609–627, https://doi.org/10.1086/628456.
1078 Dilles, J.H., Kent, A.J.R., Wooden, J.L., Tosdal, R.M., Koleszar, A., Lee, R.G., and Farmer,
1079 L.P., 2015, Zircon compositional evidence for sulfur-degassing from ore-forming arc
1080 magmas: Economic Geology, v. 110, p. 241–251,
1081 https://doi.org/10.2113/econgeo.110.1.241.
1082 Drewes, H., 1959, Turtleback faults of Death Valley, California: A reinterpretation: Geological
1083 Society of America Bulletin, v. 70, p. 1497–1508, https://doi.org/10.1130/0016-
1084 7606(1959)70[1497:TFODVC]2.0.CO;2.
1085 Drewes, H., 1963, Geology of the Funeral Peak quadrangle, California, on the east flank of
1086 Death Valley: U.S. Geological Survey Professional Paper 413, 78 p.,
1087 https://doi.org/10.3133/pp413.
1088 Eddy, M.P., Bowring, S.A., Miller, R.B., and Tepper, J.H., 2016, Rapid assembly and
1089 crystallization of a fossil large-volume silicic magma chamber: Geology, v. 44, p. 331–334,
1090 https://doi.org/10.1130/G37631.1.
1091 Eklund, O., and Shebanov, A.D., 1999, The origin of rapakivi texture by sub-isothermal
1092 decompression: Precambrian Research, v. 95, p. 129–146, https://doi.org/10.1016/S0301-
1093 9268(98)00130-2.
1094 Faulds, J.E., Feuerbach, D.L., Miller, C.F., and Smith, E.I., 2001, Cenozoic evolution of the
1095 northern Colorado River extensional corridor, southern Nevada and northwest Arizona, *in*
1096 Erskine, M.C., Faulds, J.E., Bartley, J.M., and Rowley, P.D., eds., The Geologic Transition,

1097 High Plateaus to Great Basin—A Symposium and Field Guide (The Mackin Volume): Utah
1098 Geological Association Publication 30 and Pacific Section American Association of
1099 Petroleum Geologists Guidebook GB78, p. 239–271.
1100 Feldstein, S.N., and Lange, R.A., 1999, Pliocene potassic magmas from the Kings River region,
1101 Sierra Nevada, California: Evidence for melting of a subduction-modified mantle: Journal of
1102 Petrology, v. 40, p. 1301–1320, https://doi.org/10.1093/petroj/40.8.1301.
1103 Fleming, Z., Pavlis, T., and Trullenque, G., 2022, Unraveling the multi-phase history of southern
1104 Death Valley geology, *in* Jiang, G., and Dehler, C., eds., Field Excursions from Las Vegas,
1105 Nevada: Guides to the 2022 GSA Cordilleran and Rocky Mountain Joint Section Meeting:
1106 Geological Society of America Field Guide 63, p. 67–83,
1107 https://doi.org/10.1130/2022.0063(04).
1108 Fleming, Z.D., Pavlis, T.L., and Canalda, S., 2021, Superposition of two kinematically distinct
1109 extensional phases in southern Death Valley: Implications for extensional tectonics:
1110 Geosphere, v. 17, p. 1534–1562, https://doi.org/10.1130/GES02354.1.
1111 Fountain, D.M., 1989, Growth and modification of lower continental crust in extended terrains:
1112 The role of extension and magmatic underplating, *in* Mereu, R.F., Mueller, S., and Fountain,
1113 D.M. eds., Properties and Processes of Earth's Lower Crust: American Geophysical Union
1114 Geophysical Monograph 51, p. 287–299, https://doi.org/10.1029/GM051p0287.
1115 Fowler, T.K., Jr., and Calzia, J.P., 1999, Kingston Range detachment fault, southeastern Death
1116 Valley region, California: Relation to Tertiary deposits and reconstruction of initial dip, *in*
1117 Wright, L.A., and Troxel, B.W., eds., Cenozoic Basins of the Death Valley Region:
1118 Geological Society of America Special Paper 333, p. 245–258, https://doi.org/10.1130/0-
1119 8137-2333-7.245.
1120 Fowler, T.K., Jr., Friedmann, S.J., Davis, G.A., and Bishop, K.M., 1995, Two-phase evolution of
1121 the Shadow Valley Basin, south-eastern California: A possible record of footwall uplift
1122 during extensional detachment faulting: Basin Research, v. 7, p. 165–179,
1123 https://doi.org/10.1111/j.1365-2117.1995.tb00102.x.
1124 Frankel, K.L., Owen, L.A., Dolan, J.F., Knott, J.R., Lifton, Z.M., Finkel, R.C., and Wasklewicz,
1125 T., 2016, Timing and rates of Holocene normal faulting along the Black Mountains fault
1126 zone, Death Valley, USA: Lithosphere, v. 8, p. 3–22, https://doi.org/10.1130/L464.1.
1127 Fridrich, C.J., and Thompson, R.A., 2011, Cenozoic tectonic reorganizations of the Death Valley
1128 region, southeast California and southwest Nevada: U.S. Geological Survey Professional
1129 Paper 1783, 36 p., 1 plate, https://doi.org/10.3133/pp1783.
1130 Fridrich, C.J., Minor, S.A., Ryder, P.L., Slate, J.L., Warren, R.G., Hildenbrand, T.G., Sawyer,
1131 D.A., and Orkild, P.P., 1999, Geologic map of the Oasis Valley basin and vicinity, Nye
1132 County, Nevada: U.S. Geological Survey Open-File Report 99-533-B, scale 1:62,500,
1133 https://doi.org/10.3133/ofr99533B.
1134 Friedmann, S.J., Davis, G.A., and Fowler, T.K., 1996, Geometry, paleodrainage, and geologic
1135 rates from the Miocene Shallow Valley supradetachment basin, eastern Mojave Desert,
1136 California, *in* Beratan, K.K., ed., Reconstructing the History of Basin and Range Extension
1137 Using Sedimentology and Stratigraphy: Geological Society of America Special Paper 303,
1138 p. 85–106, https://doi.org/10.1130/0-8137-2303-5.85.
1139 Gans, P.B., and Bohrson, W.A., 1998, Suppression of volcanism during rapid extension in the
1140 Basin and Range province, United States: Science, v. 279, p. 66–68,
1141 https://doi.org/10.1126/science.279.5347.66.

Gans, P.B., Mahood, G.A., and Schermer, E., 1989, Synextensional Magmatism in the Basin and Range Province: A Case Study from the Eastern Great Basin: Geological Society of America Special Paper 233, 62 p., https://doi.org/10.1130/SPE233.

Gerstenberger, H., and Haase, G., 1997, A highly effective emitter substance for mass spectrometric Pb isotope ratio determinations: Chemical Geology, v. 136, p. 309–312, https://doi.org/10.1016/S0009-2541(96)00033-2.

Gilmer, A.K., and Thompson, R.A., 2024, Whole rock geochemistry for the Central Death Valley volcanic field, California: U.S. Geological Survey Data Release, https://doi.org/10.5066/P13PNIFG.

Glazner, A.F., 2022, Cenozoic magmatism and plate tectonics in western North America: Have we got it wrong?, *in* Foulger, G.R., Hamilton, L.C., Jurdy, D.M., Stein, C.A., Howard, K.A., and Stein, S. eds., In the Footsteps of Warren B. Hamilton: New Ideas in Earth Science: Geological Society of America Special Paper 553, p. 95–108, https://doi.org/10.1130/2021.2553(09).

Glazner, A.F., and Bartley, J.M., 1984, Timing and tectonic setting of Tertiary low-angle normal faulting and associated magmatism in the southwestern United States: Tectonics, v. 3, p. 385–396, https://doi.org/10.1029/TC003i003p00385.

Glazner, A.F., and Supplee, J.A., 1982, Migration of Tertiary volcanism in the southwestern United States and subduction of the Mendocino fracture zone: Earth and Planetary Science Letters, v. 60, p. 429–436, https://doi.org/10.1016/0012-821X(82)90078-4.

Guest, B., Niemi, N., and Wernicke, B., 2007, Stateline fault system: A new component of the Miocene-Quaternary Eastern California shear zone: Geological Society of America Bulletin, v. 119, p. 1337–1347, https://doi.org/10.1130/0016-7606(2007)119[1337:SFSANC]2.0.CO;2.

Haapala, I., and Rämö, O.T., 1990, Petrogenesis of the Proterozoic rapakivi granites of Finland, *in* Stein, H.J., and Hannah, J.L., eds., Ore-Bearing Granite Systems: Petrogenesis and Mineralizing Processes: Geological Society of America Special Paper 246, p. 275–286, https://doi.org/10.1130/SPE246-p275.

Haapala, I., and Rämö, O.T., 1992, Tectonic setting and origin of the Proterozoic rapakivi granites of southeastern Fennoscandia: Earth and Environmental Science Transactions of the Royal Society of Edinburgh, v. 83, p. 165–171, https://doi.org/10.1017/S0263593300007859.

Haapala, I., Rämö, O.T., and Frindt, S., 2005, Comparison of Proterozoic and Phanerozoic rift-related basaltic-granitic magmatism: Lithos, v. 80, p. 1–32, https://doi.org/10.1016/j.lithos.2004.04.057.

Haefner, R.C., 1972, Igneous history of a rhyolite lava-flow series near Death Valley, California [Ph.D. thesis]: University Park, Pennsylvania, USA, Pennsylvania State University, 281 p.

Hamilton, W.B., 1988, Detachment faulting in the Death Valley region, California and Nevada, *in* Carr, M.D., and Yount, J.C., eds., Geologic and Hydrologic Investigations of a Potential Nuclear Waste Disposal Site at Yucca Mountain, Southern Nevada: U.S. Geological Survey Bulletin 1790, p. 51–85.

Hayman, N.W., Knott, J.R., Cowan, D.S., Nemser, E., and Sarna-Wojcicki, A.M., 2003, Quaternary low-angle slip on detachment faults in Death Valley, California: Geology, v. 31, p. 343–346, https://doi.org/10.1130/0091-7613(2003)031<0343:QLASOD>2.0.CO;2.

Hewett, D.F., 1940, New formation names to be used in the Kingston Range, Ivanpah quadrangle, California: Washington Academy of Science Journal, v. 30, p. 39–40.

Hewett, D.F., 1956, Geology and mineral resources of the Ivanpah quadrangle, California and Nevada: U.S. Geological Survey Professional Paper 275, 172 p., https://doi.org/10.3133/pp275.

Hibbard, M.J., 1981, The magma mixing origin of mantled feldspars: Contributions to Mineralogy and Petrology, v. 76, p. 158–170, https://doi.org/10.1007/BF00371956.

Hildreth, W., 1981, Gradients in silicic magma chambers: Implications for lithospheric magmatism: Journal of Geophysical Research: Solid Earth, v. 86, p. 10,153–10,192, https://doi.org/10.1029/JB086iB11p10153.

Hodges, K.V., McKenna, L.W., Stock, J., Knapp, J., Page, L., Sternlof, K., Silverberg, D., Wüst, G., and Walker, J.D., 1989, Evolution of extensional basins and basin and range topography west of Death Valley, California: Tectonics, v. 8, p. 453–467, https://doi.org/10.1029/TC008i003p00453.

Hodges, K.V., McKenna, L.W., and Harding, M.B., 1990, Structural unroofing of the central Panamint Mountains, Death Valley region, southeastern California, *in* Wernicke, B.P., ed., Basin and Range Extensional Tectonics Near the Latitude of Las Vegas, Nevada: Geological Society of America Memoir 176, p. 377–390, https://doi.org/10.1130/MEM176-p377.

Hoisch, T.D., Heizler, M.T., and Zartman, R.E., 1997, Timing of detachment faulting in the Bullfrog Hills and Bare Mountain area, southwest Nevada: Inferences from $^{40}Ar/^{39}Ar$, K-Ar, U-Pb, and fission track thermochronology: Journal of Geophysical Research: Solid Earth, v. 102, p. 2815–2833, https://doi.org/10.1029/96JB03220.

Holm, D.K., 1995, Relation of deformation and multiple intrusion in the Death Valley extended region, California, with implications for magma entrapment mechanism: Journal of Geophysical Research: Solid Earth, v. 100, p. 10,495–10,505, https://doi.org/10.1029/94JB03255.

Holm, D.K., and Dokka, R.K., 1993, Interpretation and tectonic implications of cooling histories: An example from the Black Mountains, Death Valley extended terrane, California: Earth and Planetary Science Letters, v. 116, p. 63–80, https://doi.org/10.1016/0012-821X(93)90045-B.

Holm, D.K., and Wernicke, B., 1990, Black Mountains crustal section, Death Valley extended terrain, California: Geology, v. 18, p. 520–523, https://doi.org/10.1130/0091-7613(1990)018<0520:BMCSDV>2.3.CO;2.

Holm, D.K., Snow, J.K., and Lux, D.R., 1992, Thermal and barometric constraints on the intrusive and unroofing history of the Black Mountains: Implications for timing, initial dip, and kinematics of detachment faulting in the Death Valley Region, California: Tectonics, v. 11, p. 507–522, https://doi.org/10.1029/92TC00211.

Holm, D.K., Fleck, R.J., and Lux, D.R., 1994a, The Death Valley turtlebacks reinterpreted as Miocene-Pliocene folds of a major detachment surface: The Journal of Geology, v. 102, p. 718–727, https://doi.org/10.1086/629715.

Holm, D.K., Pavlis, T.L., and Topping, D.J., 1994b, Black Mountains crustal section, Death Valley region, California: Geological investigations of an active margin, *in* McGill, S.F., and Ross, T.M., eds., Geological Society of America, Cordilleran Section, Annual Meeting: Guidebook: Geological Society of America, p. 31–54.

Hoskin, P.W.O., and Schaltegger, U., 2003, The composition of zircon and igneous and metamorphic petrogenesis: Reviews in Mineralogy and Geochemistry, v. 53, p. 27–62, https://doi.org/10.2113/0530027.

1233 Humphreys, E., 2009, Relation of flat subduction to magmatism and deformation in the western
1234 United States, *in* Kay, S.M., Ramos, V.A., and Dickinson, W.R., eds., Backbone of the
1235 Americas: Shallow Subduction, Plateau Uplift, and Ridge and Terrane Collision: Geological
1236 Society of America Memoir 204, https://doi.org/10.1130/2009.1204(04).
1237 Humphreys, E.D., 1995, Post-Laramide removal of the Farallon slab, western United States:
1238 Geology, v. 23, p. 987–990, https://doi.org/10.1130/0091-
1239 7613(1995)023<0987:PLROTF>2.3.CO;2.
1240 Hunt, C.B., and Mabey, D.R., 1966, Stratigraphy and structure, Death Valley, California: U.S.
1241 Geological Survey Professional Paper 494-A, 162 p., https://doi.org/10.3133/pp494A.
1242 Keller, C.B., Schoene, B., and Samperton, K.M., 2018, A stochastic sampling approach to zircon
1243 eruption age interpretation: Geochemical Perspectives Letters, v. 8, p. 31–35,
1244 https://doi.org/10.7185/geochemlet.1826.
1245 Kirkland, C.L., Smithies, R.H., Taylor, R.J.M., Evans, N., and McDonald, B., 2015, Zircon Th/U
1246 ratios in magmatic environs: Lithos, v. 212–215, p. 397–414,
1247 https://doi.org/10.1016/j.lithos.2014.11.021.
1248 Knott, J.R., Sarna-Wojcicki, A.M., Meyer, C.E., Tinsley, J.C., III, Wells, S.G., and Wan, E.,
1249 1999, Late Cenozoic stratigraphy and tephrochronology of the western Black Mountains
1250 piedmont, Death Valley, California: Implications for the tectonic development of Death
1251 Valley, *in* Wright, L.A., and Troxel, B.W., eds., Cenozoic Basins of the Death Valley
1252 Region: Geological Society of America Special Paper 333, p. 345–366,
1253 https://doi.org/10.1130/0-8137-2333-7.345.
1254 Knott, J.R., Sarna-Wojcicki, A.M., Machette, M.N., and Klinger, R.E., 2005, Upper Neogene
1255 stratigraphy and tectonics of Death Valley—A review: Earth-Science Reviews, v. 73,
1256 p. 245–270, https://doi.org/10.1016/j.earscirev.2005.07.004.
1257 Knott, J.R., et al., 2018, Late Neogene–Quaternary tephrochronology, stratigraphy, and
1258 paleoclimate of Death Valley, California, USA: Geological Society of America Bulletin,
1259 v. 130, p. 1231–1255, https://doi.org/10.1130/B31690.1.
1260 Konstantinou, A., Strickland, A., Miller, E.L., and Wooden, J.P., 2012, Multistage Cenozoic
1261 extension of the Albion–Raft River–Grouse Creek metamorphic core complex:
1262 Geochronologic and stratigraphic constraints: Geosphere, v. 8, p. 1429–1466,
1263 https://doi.org/10.1130/GES00778.1.
1264 Krogh, T.E., 1973, A low-contamination method for hydrothermal decomposition of zircon and
1265 extraction of U and Pb for isotopic age determinations: Geochimica et Cosmochimica Acta,
1266 v. 37, p. 485–494, https://doi.org/10.1016/0016-7037(73)90213-5.
1267 Lanphere, M.A., Wasserburg, G.J.F., Albee, A.L., and Tilton, G.R., 1964, Redistribution of
1268 strontium and rubidium isotopes during metamorphism, World Beater complex, Panamint
1269 Range, California, *in* Craig, H., Miller, S.L., and Wasserburg, G.J., eds., Isotopic and
1270 Cosmic Chemistry: Amsterdam, North-Holland Publishing Company, p. 269–320.
1271 Lima, R.D., Prior, M.G., Stockli, D.F., and Hayman, N.W., 2018, Protracted heating of the
1272 orogenic crust in Death Valley, California, USA: Geology, v. 46, p. 315–318,
1273 https://doi.org/10.1130/G39865.1.
1274 Linnen, R.L., and Keppler, H., 2002, Melt composition control of Zr/Hf fractionation in
1275 magmatic processes: Geochimica et Cosmochimica Acta, v. 66, p. 3293–3301,
1276 https://doi.org/10.1016/S0016-7037(02)00924-9.

1277 Lipman, P.W., 1980, Cenozoic volcanism in the western United States—Implications for
1278 continental tectonics, *in* National Research Council, Continental Tectonics: Washington,
1279 D.C., National Academies Press, p. 161–174.
1280 Lipman, P.W., 1984, The roots of ash flow calderas in western North America: Windows into the
1281 tops of granitic batholiths: Journal of Geophysical Research: Solid Earth, v. 89, p. 8801–
1282 8841, https://doi.org/10.1029/JB089iB10p08801.
1283 Lister, G.S., Etheridge, M.A., and Symonds, P.A., 1986, Detachment faulting and the evolution
1284 of passive continental margins: Geology, v. 14, p. 246–250, https://doi.org/10.1130/0091-
1285 7613(1986)14<246:DFATEO>2.0.CO;2.
1286 Luckow, H.G., Pavlis, T.L., Serpa, L.F., Guest, B., Wagner, D.L., Snee, L., Hensley, T.M., and
1287 Korjenkov, A., 2005, Late Cenozoic sedimentation and volcanism during transtensional
1288 deformation in Wingate Wash and the Owlshead Mountains, Death Valley: Earth-Science
1289 Reviews, v. 73, p. 177–219, https://doi.org/10.1016/j.earscirev.2005.07.013.
1290 Ludwig, K.G., 2022, Geochronologic and thermochronologic constraints on the Mesozoic to
1291 Cenozoic deformation history of southeastern California [M.S. thesis]: Columbia, Missouri,
1292 USA, University of Missouri, 178 p., https://doi.org/10.32469/10355/94115.
1293 Lutz, B.M., Ketcham, R.A., Axen, G.J., Beyene, M.A., Wells, M.L., van Wijk, J.W., Stockli,
1294 D.F., and Ross, J.I., 2021, Thermo-kinematic modeling of detachment-dominated extension,
1295 northeastern Death Valley area, USA: Implications for mid-crustal thermal-rheological
1296 evolution: Tectonophysics, v. 808, https://doi.org/10.1016/j.tecto.2021.228755.
1297 Mahon, R.C., Dehler, C.M., Link, P.K., Karlstrom, K.E., and Gehrels, G.E., 2014,
1298 Geochronologic and stratigraphic constraints on the Mesoproterozoic and Neoproterozoic
1299 Pahrump Group, Death Valley, California: A record of the assembly, stability, and breakup
1300 of Rodinia: Geological Society of America Bulletin, v. 126, p. 652–664,
1301 https://doi.org/10.1130/B30956.1.
1302 Mancktelow, N.S., and Pavlis, T.L., 1994, Fold-fault relationships in low-angle detachment
1303 systems: Tectonics, v. 13, p. 668–685, https://doi.org/10.1029/93TC03489.
1304 Mattinson, J.M., 2005, Zircon U–Pb chemical abrasion ("CA-TIMS") method: Combined
1305 annealing and multi-step partial dissolution analysis for improved precision and accuracy of
1306 zircon ages: Chemical Geology, v. 220, p. 47–66,
1307 https://doi.org/10.1016/j.chemgeo.2005.03.011.
1308 Matzel, J.E.P., Bowring, S.A., and Miller, R.B., 2006, Time scales of pluton construction at
1309 differing crustal levels: Examples from the Mount Stuart and Tenpeak intrusions, North
1310 Cascades, Washington: Geological Society of America Bulletin, v. 118, p. 1412–1430,
1311 https://doi.org/10.1130/B25923.1.
1312 McAllister, J.F., 1970, Geology of the Furnace Creek borate area, Death Valley, Inyo County,
1313 California: California Division of Mines and Geology Map Sheet 14, scale 1:24,000.
1314 McAllister, J.F., 1973, Geologic map and sections of the Amargosa Valley borate area, southeast
1315 continuation of the Furnace Creek area, Inyo County, CA: U.S. Geological Survey
1316 Miscellaneous Geologic Investigations Map I-782, scale 1:24,000,
1317 https://doi.org/10.3133/i782.
1318 McDowell, S.D., 1974, Emplacement of the Little Chief Stock, Panamint Range, California:
1319 Geological Society of America Bulletin, v. 85, p. 1535–1546, https://doi.org/10.1130/0016-
1320 7606(1974)85<1535:EOTLCS>2.0.CO;2.

McDowell, S.D., 1978, Little Chief Granite porphyry: Feldspar crystallization history: Geological Society of America Bulletin, v. 89, p. 33–49, https://doi.org/10.1130/0016-7606(1978)89<33:LCGPFC>2.0.CO;2.

McKenna, L.W., 1990, Processes of continental extension as viewed from the Death Valley region, California [Ph.D. thesis]: Cambridge, Massachusetts, USA, Massachusetts Institute of Technology, 199 p.

McKenna, L.W., and Hodges, K.V., 1990, Constraints on the kinematics and timing of late Miocene-Recent extension between the Panamint and Black Mountains, southeastern California, *in* Wernicke, B.P., ed., Basin and Range Extensional Tectonics Near the Latitude of Las Vegas, Nevada: Geological Society of America Memoir 176, p. 363–376, https://doi.org/10.1130/MEM176-p363.

McLean, N.M., Bowring, J.F., and Bowring, S.A., 2011, An algorithm for U-Pb isotope dilution data reduction and uncertainty propagation: Geochemistry, Geophysics, Geosystems, v. 12, Q0AA18, https://doi.org/10.1029/2010GC003478.

McLean, N.M., Condon, D.J., Schoene, B., and Bowring, S.A., 2015, Evaluating uncertainties in the calibration of isotopic reference materials and multi-element isotopic tracers (EARTHTIME Tracer Calibration Part II): Geochimica et Cosmochimica Acta, v. 164, p. 481–501, https://doi.org/10.1016/j.gca.2015.02.040.

McQuarrie, N., and Oskin, M., 2010, Palinspastic restoration of NAVDat and implications for the origin of magmatism in southwestern North America: Journal of Geophysical Research: Solid Earth, v. 115, https://doi.org/10.1029/2009JB006435.

McQuarrie, N., and Wernicke, B.P., 2005, An animated tectonic reconstruction of southwestern North America since 36 Ma: Geosphere, v. 1, p. 147–172, https://doi.org/10.1130/GES00016.1.

Meurer, K.J., 1992, Tectonic evolution of Smith Mountain–Gold Valley region, Death Valley, California [M.S. thesis]: New Orleans, Louisiana, USA, University of New Orleans, 102 p.

Miller, C.F., Furbish, D.J., Walker, B.A., Claiborne, L.L., Koteas, G.C., Bleick, H.A., and Miller, J.S., 2011, Growth of plutons by incremental emplacement of sheets in crystal-rich host: Evidence from Miocene intrusions of the Colorado River region, Nevada, USA: Tectonophysics, v. 500, p. 65–77, https://doi.org/10.1016/j.tecto.2009.07.011.

Miller, M.B., and Pavlis, T.L., 2005, The Black Mountains turtlebacks: Rosetta stones of Death Valley tectonics: Earth-Science Reviews, v. 73, p. 115–138, https://doi.org/10.1016/j.earscirev.2005.04.007.

Miller, M.B., Friedman, R., and Dee, S., 2004, Pre-10 Ma TIMS U-Pb zircon age for the Smith Mountain Granite, Death Valley, California: Implications for the timing of major extension: Geological Society of America Abstracts with Programs, v. 36, no. 5, p. 501.

Miller, M.G., 1991, High-angle origin of the currently low-angle Badwater Turtleback fault, Death Valley, California: Geology, v. 19, p. 372–375, https://doi.org/10.1130/0091-7613(1991)019<0372:HAOOTC>2.3.CO;2.

Miller, M.G., 1992, Brittle faulting induced by ductile deformation of a rheologically stratified rock sequence, Badwater Turtleback, Death Valley, California: Geological Society of America Bulletin, v. 104, p. 1376–1385, https://doi.org/10.1130/0016-7606(1992)104<1376:BFIBDD>2.3.CO;2.

Miller, M.G., 1999, Implications of ductile strain on the Badwater Turtleback for pre-14-Ma extension in the Death Valley region, California, *in* Wright, L.A., and Troxel, B.W., eds.,

1366 Cenozoic Basins of the Death Valley Region: Geological Society of America Special Paper
1367 333, p. 115–126, https://doi.org/10.1130/0-8137-2333-7.115.
1368 Miller, M.G., 2003, Basement-involved thrust faulting in a thin-skinned fold-and-thrust belt,
1369 Death Valley, California, USA: Geology, v. 31, p. 31–34, https://doi.org/10.1130/0091-
1370 7613(2003)031<0031:BITFIA>2.0.CO;2.
1371 Miller, M.G., and Friedman, R.M., 1999, Early Tertiary magmatism and probable Mesozoic
1372 fabrics in the Black Mountains, Death Valley, California: Geology, v. 27, p. 19–22,
1373 https://doi.org/10.1130/0091-7613(1999)027<0019:ETMAPM>2.3.CO;2.
1374 Miller, M.G., and Friedman, R., 2003, New U-Pb zircon ages indicate major extension in Death
1375 Valley, CA predated 10 Ma: Implications for models of crustal extension: Geological
1376 Society of America Abstracts with Programs, v. 35, no. 6, p. 26.
1377 Miller, M.G., and Prave, A.R., 2002, Rolling hinge or fixed basin?: A test of continental
1378 extensional models in Death Valley, California, United States: Geology, v. 30, p. 847–850,
1379 https://doi.org/10.1130/0091-7613(2002)030<0847:RHOFBA>2.0.CO;2.
1380 Nekvasil, H., 1991, Ascent of felsic magmas and formation of rapakivi: American Mineralogist,
1381 v. 76, p. 1279–1290.
1382 Niemi, N.A., Wernicke, B.P., Brady, R.J., Saleeby, J.B., and Dunne, G.C., 2001, Distribution
1383 and provenance of the middle Miocene Eagle Mountain Formation, and implications for
1384 regional kinematic analysis of the Basin and Range province: Geological Society of
1385 America Bulletin, v. 113, p. 419–442, https://doi.org/10.1130/0016-
1386 7606(2001)113<0419:DAPOTM>2.0.CO;2.
1387 Norton, I., 2011, Two-stage formation of Death Valley: Geosphere, v. 7, p. 171–182,
1388 https://doi.org/10.1130/GES00588.1.
1389 Otton, J.K., 1977, Geology of the central Black Mountains, Death Valley, California: The
1390 turtleback terrane [Ph.D. thesis]: University Park, Pennsylvania, USA, Pennsylvania State
1391 University, 155 p.
1392 Parsons, T., Thompson, G.A., and Smith, R.P., 1998, More than one way to stretch: A tectonic
1393 model for extension along the plume track of the Yellowstone hotspot and adjacent Basin
1394 and Range Province: Tectonics, v. 17, p. 221–234, https://doi.org/10.1029/98TC00463.
1395 Paterson, S.R., Okaya, D., Memeti, V., Economos, R., and Miller, R.B., 2011, Magma addition
1396 and flux calculations of incrementally constructed magma chambers in continental margin
1397 arcs: Combined field, geochronologic, and thermal modeling studies: Geosphere, v. 7,
1398 p. 1439–1468, https://doi.org/10.1130/GES00696.1.
1399 Pavlis, T.L., 1996, Fabric development in syn-tectonic intrusive sheets as a consequence of melt-
1400 dominated flow and thermal softening of the crust: Tectonophysics, v. 253, p. 1–31,
1401 https://doi.org/10.1016/0040-1951(95)00049-6.
1402 Pavlis, T.L., and Trullenque, G., 2021, Evidence for 40–41 km of dextral slip on the southern
1403 Death Valley fault: Implications for the Eastern California shear zone and extensional
1404 tectonics: Geology, v. 49, p. 767–772, https://doi.org/10.1130/G48528.1.
1405 Pavlis, T.L., Tracy, R.J., Hollister, L., and Chadwick, J., 2018, Reappraisal of the Death Valley
1406 turtlebacks from analysis of metamorphism and ductile deformation in the turtlebacks and
1407 Panamint Mountains: Geological Society of America Abstracts with Programs, v. 50, no. 5,
1408 https://doi.org/10.1130/abs/2018RM-314071.
1409 Péron-Pinvidic, G., Manatschal, G., Masini, E., Sutra, E., Flament, J.M., Haupert, I., and
1410 Unternehr, P., 2017, Unravelling the along-strike variability of the Angola–Gabon rifted
1411 margin: a mapping approach, *in* Sabato Ceraldi, T., Hodgkinson, R.A., and Backe, G., eds.,

Petroleum Geoscience of the West Africa Margin: Geological Society, London, Special Publication 438, p. 49–76, https://doi.org/10.1144/SP438.1.
Petronis, M.S., Geissman, J.W., Holm, D.K., Wernicke, B., and Schauble, E., 2002, Assessing vertical axis rotations in large-magnitude extensional settings: A transect across the Death Valley extended terrane, California: Journal of Geophysical Research: Solid Earth, v. 107, https://doi.org/10.1029/2001JB000239.
Putirka, K., and Platt, B., 2012, Basin and Range volcanism as a passive response to extensional tectonics: Geosphere, v. 8, p. 1274–1285, https://doi.org/10.1130/GES00803.1.
Rämö, O.T., and Haapala, I., 1995, One hundred years of rapakivi granite: Mineralogy and Petrology, v. 52, p. 129–185, https://doi.org/10.1007/BF01163243.
Rämö, O.T., Calzia, J.P., and Andersen, T., 2011, Anatomy of the Shoshone Pluton, Death Valley, California—World's youngest rapakivi granite, *in* Kultti, S., and Rämö, O.T., eds., 8th National Geological Colloquium, Program and Abstracts: University of Helsinki, Department of Geosciences and Geography Publication C5, p. 34.
Renik, B., and Christie-Blick, N., 2013, A new hypothesis for the amount and distribution of dextral displacement along the Fish Lake Valley–northern Death Valley–Furnace Creek fault zone, California-Nevada: Tectonics, v. 32, p. 123–145, https://doi.org/10.1029/2012TC003170.
Rubatto, D., 2017, Zircon: The metamorphic mineral: Reviews in Mineralogy and Geochemistry, v. 83, p. 261–295, https://doi.org/10.2138/rmg.2017.83.9.
Rubatto, D., Williams, I.S., and Buick, I.S., 2001, Zircon and monazite response to prograde metamorphism in the Reynolds Range, central Australia: Contributions to Mineralogy and Petrology, v. 140, p. 458–468, https://doi.org/10.1007/PL00007673.
Samperton, K.M., Schoene, B., Cottle, J.M., Keller, C.B., Crowley, J.L., and Schmitz, M.D., 2015, Magma emplacement, differentiation and cooling in the middle crust: Integrated zircon geochronological–geochemical constraints from the Bergell Intrusion, Central Alps: Chemical Geology, v. 417, p. 322–340, https://doi.org/10.1016/j.chemgeo.2015.10.024.
Schoene, B., Latkoczy, C., Schaltegger, U., and Günther, D., 2010, A new method integrating high-precision U–Pb geochronology with zircon trace element analysis (U–Pb TIMS-TEA): Geochimica et Cosmochimica Acta, v. 74, p. 7144–7159, https://doi.org/10.1016/j.gca.2010.09.016.
Schoene, B., Schaltegger, U., Brack, P., Latkoczy, C., Stracke, A., and Günther, D., 2012, Rates of magma differentiation and emplacement in a ballooning pluton recorded by U–Pb TIMS-TEA, Adamello batholith, Italy: Earth and Planetary Science Letters, v. 355–356, p. 162–173, https://doi.org/10.1016/j.epsl.2012.08.019.
Serpa, L., and Pavlis, T.L., 1996, Three-dimensional model of the late Cenozoic history of the Death Valley region, southeastern California: Tectonics, v. 15, p. 1113–1128, https://doi.org/10.1029/96TC01633.
Serpa, L., de Voogd, B., Wright, L., Willemin, J., Oliver, J., Hauser, E., and Troxel, B., 1988, Structure of the central Death Valley pull-apart basin and vicinity from COCORP profiles in the southern Great Basin: Geological Society of America Bulletin, v. 100, p. 1437–1450, https://doi.org/10.1130/0016-7606(1988)100<1437:SOTCDV>2.3.CO;2.
Sizemore, T., Wielicki, M.M., Çemen, I., Stockli, D., Heizler, M., and Robinson, D., 2019, Structural evolution of central Death Valley, California, using new thermochronometry of the Badwater turtleback: Lithosphere, v. 11, p. 436–447, https://doi.org/10.1130/L1044.1.

1457 Snow, J.K., and Lux, D.R., 1999, Tectono-sequence stratigraphy of Tertiary rocks in the
1458 Cottonwood Mountains and northern Death Valley area, California and Nevada, *in* Wright,
1459 L.A., and Troxel, B.W., eds., Cenozoic Basins of the Death Valley Region: Geological
1460 Society of America Special Paper 333, p. 17–64, https://doi.org/10.1130/0-8137-2333-7.17.
1461 Snow, J.K., and Wernicke, B., 1989, Uniqueness of geological correlations: An example from
1462 the Death Valley extended terrain: Geological Society of America Bulletin, v. 101, p. 1351–
1463 1362, https://doi.org/10.1130/0016-7606(1989)101<1351:UOGCAE>2.3.CO;2.
1464 Snow, J.K., and Wernicke, B., 2000, Cenozoic tectonism in the central Basin and Range:
1465 Magnitude, rate, and distribution of upper crustal strain: American Journal of Science,
1466 v. 300, p. 659–719, https://doi.org/10.2475/ajs.300.9.659.
1467 Snow, J.K., and White, C., 1990, Listric normal faulting and synorogenic sedimentation,
1468 northern Cottonwood Mountains, Death Valley region, California, *in* Wernicke, B.P., ed.,
1469 Basin and Range Extensional Tectonics Near the Latitude of Las Vegas, Nevada: Geological
1470 Society of America Memoir 176, p. 413–446, https://doi.org/10.1130/MEM176-p413.
1471 Snyder, N.P., and Hodges, K.V., 2000, Depositional and tectonic evolution of a supradetachment
1472 basin: $^{40}Ar/^{39}Ar$ geochronology of the Nova Formation, Panamint Range, California: Basin
1473 Research, v. 12, p. 19–30, https://doi.org/10.1046/j.1365-2117.2000.00108.x.
1474 Sparks, R.S.J., Annen, C., Blundy, J.D., Cashman, K.V., Rust, A.C., and Jackson, M.D., 2019,
1475 Formation and dynamics of magma reservoirs: Philosophical Transactions of the Royal
1476 Society, London, Series A: Mathematical, Physical and Engineering Sciences, v. 377,
1477 https://doi.org/10.1098/rsta.2018.0019.
1478 Stern, T.W., Newell, M.F., and Hunt, C.B., 1966, Uranium-lead and potassium-argon ages of
1479 parts of the Amargosa thrust complex, Death Valley, California, *in* U.S. Geological Survey,
1480 Geological Survey Research 1966, Chapter B: U.S. Geological Survey Professional Paper
1481 550-B, p. 142–147.
1482 Stewart, J.H., 1983, Extensional tectonics in the Death Valley area, California: Transport of the
1483 Panamint Range structural block 80 km northwestward: Geology, v. 11, p. 153–157,
1484 https://doi.org/10.1130/0091-7613(1983)11<153:ETITDV>2.0.CO;2.
1485 Stockli, D.F., Dumitru, T.A., McWilliams, M.O., and Farley, K.A., 2003, Cenozoic tectonic
1486 evolution of the White Mountains, California and Nevada: Geological Society of America
1487 Bulletin, v. 115, p. 788–816, https://doi.org/10.1130/0016-
1488 7606(2003)115<0788:CTEOTW>2.0.CO;2.
1489 Stull, R.J., 1978, Mantled feldspars from the Golden Horn batholith, Washington: Lithos, v. 11,
1490 p. 243–249, https://doi.org/10.1016/0024-4937(78)90024-5.
1491 Sun, S., and McDonough, W.F., 1989, Chemical and isotopic systematics of oceanic basalts:
1492 Implications for mantle composition and processes, *in* Saunders, A.D., and Norry, M.J. eds.,
1493 Magmatism in the Ocean Basins: Geological Society, London, Special Publication 42, p.
1494 313–345, https://doi.org/10.1144/GSL.SP.1989.042.01.19.
1495 Tang, M., Erdman, M., Eldridge, G., and Lee, C.-T.A., 2018, The redox "filter" beneath
1496 magmatic orogens and the formation of continental crust: Science Advances, v. 4,
1497 https://doi.org/10.1126/sciadv.aar4444.
1498 Topping, D.J., 1993, Paleogeographic reconstruction of the Death Valley extended region:
1499 Evidence from Miocene large rock-avalanche deposits in the Amargosa Chaos Basin,
1500 California: Geological Society of America Bulletin, v. 105, p. 1190–1213,
1501 https://doi.org/10.1130/0016-7606(1993)105<1190:PROTDV>2.3.CO;2.

Troxel, B.W., and Wright, L.A., 1987, Tertiary extensional features, Death Valley region, eastern California, *in* Hill, M.L., ed., Cordilleran Section of the Geological Society of America: Geological Society of America, Decade of North American Geology, Centennial Field Guide, v. 1, p. 121–132, https://doi.org/10.1130/0-8137-5401-1.121.

Vavra, G., Schmid, R., and Gebauer, D., 1999, Internal morphology, habit and U-Th-Pb microanalysis of amphibolite-to-granulite facies zircons: Geochronology of the Ivrea Zone (Southern Alps): Contributions to Mineralogy and Petrology, v. 134, p. 380–404, https://doi.org/10.1007/s004100050492.

Vernon, R.H., 2016, Rapakivi granite problems: Plagioclase mantles and ovoid megacrysts: Australian Journal of Earth Sciences, v. 63, p. 675–700, https://doi.org/10.1080/08120099.2016.1241953.

Wagner, D.L., 1988, Evidence for late Cenozoic extension across Wingate Wash, Death Valley region, southeastern California, *in* Gregory, J.L., and Baldwin, E.J., eds., Geology of the Death Valley Region: South Coast Geological Society Annual Field Trip Guidebook 16, p. 243–259.

Walker, B.A., Jr., Miller, C.F., Lowery Claiborne, L., Wooden, J.L., and Miller, J.S., 2007, Geology and geochronology of the Spirit Mountain batholith, southern Nevada: Implications for timescales and physical processes of batholith construction: Journal of Volcanology and Geothermal Research, v. 167, p. 239–262, https://doi.org/10.1016/j.jvolgeores.2006.12.008.

Walker, J.D., Burchfiel, B.C., and Davis, G.A., 1995, New age controls on initiation and timing of foreland belt thrusting in the Clark Mountains, southern California: Geological Society of America Bulletin, v. 107, p. 742–750, https://doi.org/10.1130/0016-7606(1995)107<0742:NACOIA>2.3.CO;2.

Wang, K., Plank, T., Walker, J.D., and Smith, E.I., 2002, A mantle melting profile across the Basin and Range, SW USA: Journal of Geophysical Research: Solid Earth, v. 107, https://doi.org/10.1029/2001JB000209.

Wark, D.A., and Stimac, J.A., 1992, Origin of mantle (rapakivi) feldspars: Experimental evidence of a dissolution- and diffusion-controlled mechanism: Contributions to Mineralogy and Petrology, v. 111, p. 345–361, https://doi.org/10.1007/BF00311196.

Wasserburg, G.J., Wetherill, G.W., and Wright, L.A., 1959, Ages in the Precambrian terrane of Death Valley, California: The Journal of Geology, v. 67, p. 702–708, https://doi.org/10.1086/626628.

Watson, E.B., and Harrison, T.M., 1983, Zircon saturation revisited: Temperature and composition effects in a variety of crustal magma types: Earth and Planetary Science Letters, v. 64, p. 295–304, https://doi.org/10.1016/0012-821X(83)90211-X.

Wernicke, B., 1992, Cenozoic extensional tectonics of the U.S. Cordillera, *in* Burchfiel, B.C., Lipman, P.W., and Zoback, M.L. eds., The Cordilleran Orogen: Conterminous U.S.: Boulder, Colorado, Geological Society of America, Geology of North America, v. G-3, p. 553–582, https://doi.org/10.1130/DNAG-GNA-G3.553.

Wernicke, B.P., England, P.C., Sonder, L.J., and Christiansen, R.L., 1987, Tectonomagmatic evolution of Cenozoic extension in the North American Cordillera, *in* Coward, M.P., Dewey, J.F., and Hancock, P.L., eds., Continental Extensional Tectonics: Geological Society, London, Special Publication 28, p. 203–221, https://doi.org/10.1144/GSL.SP.1987.028.01.15.

Wernicke, B.P., Axen, G.J., and Snow, J.K., 1988, Basin and Range extensional tectonics at the latitude of Las Vegas, Nevada: Geological Society of America Bulletin, v. 100, p. 1738–1757, https://doi.org/10.1130/0016-7606(1988)100<1738:BARETA>2.3.CO;2.

Wotzlaw, J.-F., Schaltegger, U., Frick, D.A., Dungan, M.A., Gerdes, A., and Günther, D., 2013, Tracking the evolution of large-volume silicic magma reservoirs from assembly to supereruption: Geology, v. 41, p. 867–870, https://doi.org/10.1130/G34366.1.

Wright, L.A., Otton, J.K., and Troxel, B.W., 1974, Turtleback surfaces of Death Valley viewed as phenomena of extensional tectonics: Geology, v. 2, p. 53–54, https://doi.org/10.1130/0091-7613(1974)2<53:TSODVV>2.0.CO;2.

Wright, L.A., Thompson, R.A., Troxel, B.W., Pavlis, T.L., DeWitt, E., Otton, J.K., Ellis, M.A., Miller, M.G., and Serpa, L.F., 1991, Cenozoic magmatic and tectonic evolution of the east-central Death Valley region, California, *in* Walawender, M.J., and Hanan, B.B., eds., Geological Excursions in Southern California and Mexico: Guidebook, 1991 Annual Meeting, Geological Society of America, October 21–24, 1991: San Diego, California, Department of Geological Sciences, San Diego State University, p. 93–127.

Zandt, G., and Humphreys, E., 2008, Toroidal mantle flow through the western U.S. slab window: Geology, v. 36, p. 295–298, https://doi.org/10.1130/G24611A.1.

TABLE 1. LIST OF STUDIED LATE MIOCENE PLUTONS IN DEATH VALLEY

Sample ID	Abbreviated sample name	Rock name	Latitude (°N)	Longitude (°W)
DVCC18-2	Lower WSD	Willow Spring Diorite	36.053919	116.720879
DVCC18-14	Middle WSD	Willow Spring Diorite	36.048960	116.688409
DVCC18-5	Upper WSD	Willow Spring Diorite	36.073299	116.653044
DVCC18-8	QGV	Quartz monzonite of Gold Valley	36.072939	116.640733
DVCC18-9	SMG-F	Smith Mountain Granite (fine-grained phase)	35.997153	116.636151
DVCC18-10	SMG-C	Smith Mountain Granite (coarse-grained phase)	35.997326	116.635966
DVCC18-3	GDP	Granite of Deadman Pass	36.082292	116.438861
20RT18	DFS	Diorite of Furnace site	36.18169	116.67451
LCN	LCG-N	Little Chief Granite (northern facies)	36.172300	117.061800
LCS	LCG-S	Little Chief Granite (southern facies)	36.115200	117.071700
KRG_north	KRG-F	Kingston Range Granite (feldspar porphyry phase)	35.777400	115.9609
KRG_south	KRG-Q	Kingston Range Granite (quartz porphyry phase)	35.742	115.9583
RH420	GRHS	Granite of Rabbit Holes Spring (gray monzonite phase)	35.714700	116.0249

TABLE 2. SUMMARY OF THE MIOCENE PLUTONS WITHIN THE FIELD AREA (FIG. 2) WITH ZIRCON CRYSTALLIZATION AGES FROM THIS STUDY

Pluton	Location	Prior geochronology (Ma)	Zircon crystallization age distribution (Ma; this study)	Composition	Emplacement depth (km)	Key features
Kingston Range Granite	Kingston Range	12.4 (hornblende $^{40}Ar/^{39}Ar$; Calzia, 1990)	13.17–12.07	Rapakivi granite	<4	Three facies (feldspar porphyry, quartz porphyry, aplite), abundant miarolitic cavities and mafic xenoliths
Granite of Rabbit Holes Spring	~1 km west of Kingston Range	–	12.15–11.83	Rapakivi granite	Shallow	Two facies divided into gray monzogranite and tan monzogranite
Little Chief Granite	Panamint Range	11.21 (biotite $^{40}Ar/^{39}Ar$; McKenna, 1990)	11.56–11.27	Rapakivi granite	Hypabyssal	Two facies (northern and southern), miarolitic cavities, monazite in southern facies, mafic inclusions
Willow Spring Diorite	Black Mountains	11.6 (zircon U-Pb; Asmerom et al., 1990)	11.26–10.08	Hornblende gabbro to quartz diorite	~15–20 km	Sill-like intrusion, mixed magmas, ductile fabrics at base, brittle deformation at higher levels
Smith Mountain Granite	Black Mountains	10.45 (zircon U-Pb; Miller et al., 2004)	10.81–10.25	Biotite rapakivi granite	>10 km	Magma mingling with Willow Spring Diorite, no ductile deformation
Quartz monzonite of Gold Valley	Black Mountains	8.69 (hornblende $^{40}Ar/^{39}Ar$; Holm et al., 1992)	10.82–10.19	Rapakivi quartz monzonite to granite	Mid-crustal	Sheeted tabular-shaped pluton, intrudes Willow Spring Diorite and Smith Mountain Granite
Granite of Deadman Pass	Greenwater Range	–	8.18–7.88	Rapakivi granite	~2–2.5 km	Contains xenoliths of gneiss, marble, and quartzite
Diorite of Furnace Site	Black Mountains	–	7.90	Quartz diorite	–	Fine-grained diorite, younger than Willow Spring Diorite
Shoshone pluton	Greenwater Range	10.0 (zircon U-Pb; Rämö et al., 2011)	–	Rapakivi quartz monzonite	Hypabyssal	Miarolitic cavities
Devil Peak intrusion	Spring Mountains	13.2 (zircon U-Pb; Guest et al., 2007)	–	Felsic intrusion	Hypabyssal	Fine-grained to porphyritic rhyolite dome

Note: For additional details about prior geochronology for the plutons and calculations of the zircon age distribution, see text. Data for this table were sourced from Hewett (1956), Drewes (1963), McDowell (1974, 1978), Otton (1977), Almashoor (1983), Asmerom et al. (1990), Calzia (1990), McKenna (1990), Meurer (1992), Holm et al. (1992, 1994a, 1994b), Holm (1995), Calzia et al. (2000, 2003, 2016), Miller et al. (2004), Calzia and Rämö (2005), Pavlis et al. (2018), and Fleming et al. (2022).

TABLE 3. CA-ID-TIMS U-Pb ZIRCON DATES, COMPOSITION, AND ISOTOPIC RATIOS

Sample name	Fraction ID	Dates (Ma)		Composition					Isotopic ratios			
		$^{206}Pb/^{238}U$[a]	±2σ abs.	Mass U (pg)	Th/U[b]	Pb* (pg)[c]	Pb_c (pg)[d]	Pb*/Pb_c[e]	$^{206}Pb/^{204}Pb$[f]	$^{208}Pb/^{206}Pb$[g]	$^{206}Pb/^{238}U$[g]	±2σ (%)
Willow Spring Diorite												
Lower Willow Spring Diorite (Lower WSD)												
DVCC18-2	L2	10.919	0.042	1123.2	0.92	2.19	0.77	2.85	176.02	0.295	1.683E-03	0.35
DVCC18-2	L3	11.182	0.028	1550.1	0.95	3.12	0.66	4.73	277.55	0.306	1.724E-03	0.18
DVCC18-2	L5	11.050	0.026	1420.7	0.86	2.76	0.61	4.49	269.64	0.278	1.703E-03	0.19
DVCC18-2	L13	10.949	0.053	954.1	0.75	1.79	1.11	1.61	111.36	0.240	1.687E-03	0.48
DVCC18-2	M15	10.928	0.065	828.4	0.77	1.56	1.32	1.18	87.86	0.249	1.684E-03	0.59
DVCC18-2	XL2T	10.755	0.024	2829.6	0.73	5.17	1.31	3.95	252.27	0.235	1.657E-03	0.19
DVCC18-2	XL3T	11.086	0.022	3741.0	0.84	7.25	0.62	11.64	687.50	0.270	1.709E-03	0.13
DVCC18-2	XL7B	10.842	0.026	2407.9	0.70	4.40	0.66	6.62	413.43	0.225	1.670E-03	0.21
DVCC18-2	XL8T	10.865	0.041	807.2	0.99	1.59	0.63	2.51	158.32	0.320	1.675E-03	0.34
DVCC18-2	XL9B	10.492	0.037	2090.4	1.21	4.19	1.25	3.34	194.87	0.391	1.618E-03	0.27
DVCC18-2	XL10B	11.260	0.022	2093.1	0.84	4.12	0.64	6.45	389.70	0.270	1.736E-03	0.13
DVCC18-2	XL10C	10.943	0.022	3449.0	0.77	6.49	1.08	6.03	370.84	0.250	1.686E-03	0.14
DVCC18-2	XL10T	10.707	0.089	391.2	0.78	0.72	0.77	0.93	72.04	0.251	1.649E-03	0.84
Middle Willow Spring Diorite (Middle WSD)												
DVCC18-14	L2	10.331	0.075	1738.0	1.25	3.45	3.16	1.09	76.15	0.402	1.592E-03	0.73
DVCC18-14	L6T	10.371	0.041	1342.6	1.34	2.73	1.27	2.15	128.96	0.433	1.598E-03	0.38
DVCC18-14	L9B	10.447	0.113	473.2	1.25	0.95	1.29	0.74	56.38	0.404	1.610E-03	1.09
DVCC18-14	M2	10.585	0.083	643.2	1.55	1.40	1.24	1.12	72.58	0.499	1.632E-03	0.78
DVCC18-14	M12	10.388	0.041	1370.2	1.20	2.71	1.31	2.07	128.43	0.388	1.600E-03	0.38
DVCC18-14	M33	10.398	0.192	262.7	1.12	0.51	1.16	0.44	41.97	0.362	1.601E-03	1.87
DVCC18-14	XL9	10.377	0.018	3798.6	1.20	7.49	0.75	9.95	544.35	0.386	1.599E-03	0.12
DVCC18-14	z2	10.355	0.045	1007.7	1.17	1.97	0.92	2.14	132.67	0.376	1.595E-03	0.42
DVCC18-14	z5	10.369	0.030	562.7	1.02	1.06	0.35	3.06	187.28	0.329	1.597E-03	0.27
DVCC18-14	z12	10.204	0.236	90.7	0.88	0.16	0.50	0.33	37.67	0.286	1.570E-03	2.36
DVCC18-14	z15	10.343	0.038	504.9	0.92	0.93	0.43	2.15	140.00	0.296	1.592E-03	0.36
DVCC18-14	z19	10.347	0.073	400.7	1.46	0.84	0.57	1.48	92.71	0.470	1.595E-03	0.70
Upper Willow Spring Diorite (Upper WSD)												
DVCC18-5	L11	10.063	0.056	1482.5	1.05	2.75	1.87	1.47	97.05	0.340	1.551E-03	0.53
DVCC18-5	M2	10.048	0.175	414.2	0.90	0.74	1.77	0.42	41.94	0.291	1.548E-03	1.78
DVCC18-5	XL2B	10.069	0.077	605.9	0.81	1.06	0.56	1.87	127.44	0.260	1.550E-03	0.76
DVCC18-5	XL3	10.089	0.024	3186.0	1.07	5.94	0.61	9.69	545.85	0.344	1.555E-03	0.10
DVCC18-5	XL2T	10.237	0.193	115.8	0.96	0.21	0.54	0.40	40.48	0.310	1.577E-03	1.92
DVCC18-5	z1	10.075	0.227	64.1	1.00	0.12	0.34	0.35	38.19	0.321	1.552E-03	2.30
DVCC18-5	z5	10.081	0.104	164.2	0.42	0.26	0.41	0.63	59.66	0.135	1.550E-03	1.06
Smith Mountain Granite												
Smith Mountain Granite, fine-grained phase (SMG-F)												
DVCC18-9	L10	10.484	0.064	1278.9	0.89	2.37	1.98	1.20	87.07	0.289	1.613E-03	0.62
DVCC18-9	M3	10.815	0.181	153.5	1.16	0.31	0.38	0.83	61.86	0.375	1.665E-03	1.70
DVCC18-9	M21	10.560	0.196	106.5	1.21	0.22	0.48	0.45	41.74	0.390	1.625E-03	1.89
DVCC18-9	M23	10.595	0.025	857.2	1.32	1.78	0.45	3.97	222.68	0.426	1.631E-03	0.23
DVCC18-9	z8	10.333	0.079	197.4	1.05	0.37	0.36	1.06	76.62	0.339	1.590E-03	0.77
DVCC18-9	z9	10.348	0.066	226.3	0.96	0.42	0.31	1.34	93.90	0.311	1.592E-03	0.65
DVCC18-9	z10	10.248	0.040	497.9	1.10	0.95	0.44	2.16	135.55	0.356	1.576E-03	0.39
Smith Mountain Granite, coarse-grained facies (SMG-C)												
DVCC18-10	M6	10.403	0.029	705.8	1.42	1.47	0.44	3.36	187.65	0.459	1.602E-03	0.28
DVCC18-10	M17	10.457	0.119	267.6	1.09	0.52	0.74	0.70	55.77	0.353	1.610E-03	1.16
DVCC18-10	XL1T	10.546	0.028	726.8	0.73	1.30	0.34	3.86	241.69	0.236	1.622E-03	0.27
DVCC18-10	XL4B	10.492	0.151	344.5	0.77	0.62	1.13	0.55	50.10	0.249	1.614E-03	1.47
DVCC18-10	XL6	10.527	0.017	1668.7	0.97	3.17	0.58	5.50	325.11	0.313	1.620E-03	0.16
DVCC18-10	XL8B	10.448	0.064	484.7	0.71	0.86	0.74	1.16	87.93	0.230	1.607E-03	0.62
Quartz monzonite of Gold Valley (QGV)												
DVCC18-8	L2T	10.822	0.092	469.9	0.77	0.87	0.99	0.88	70.44	0.249	1.666E-03	0.86
DVCC18-8	M3	10.426	0.074	294.0	1.22	0.59	0.38	1.56	100.83	0.393	1.605E-03	0.71
DVCC18-8	M6	10.382	0.200	189.2	1.06	0.36	0.90	0.40	40.88	0.343	1.598E-03	1.96

DVCC18-8	M18	10.500	0.085	731.5	0.87	1.35	1.56	0.87	68.42	0.281	1.616E-03	0.83
DVCC18-8	M19	10.312	0.060	1141.7	1.47	2.38	1.64	1.45	90.94	0.476	1.588E-03	0.58
DVCC18-8	M21	10.354	0.103	2566.6	0.79	4.58	6.36	0.72	60.94	0.254	1.593E-03	1.01
DVCC18-8	z1	10.383	0.017	2144.8	0.98	4.02	0.74	5.44	321.33	0.316	1.598E-03	0.15
DVCC18-8	z2	10.194	0.051	884.0	0.99	1.63	1.07	1.52	103.16	0.321	1.569E-03	0.50
DVCC18-8	z3	10.375	0.017	1931.4	0.76	3.43	0.66	5.17	322.37	0.244	1.596E-03	0.16
DVCC18-8	z4	10.496	0.012	3656.0	1.31	7.48	0.43	17.29	909.51	0.422	1.616E-03	0.08
Diorite of Furnace Site (DFS)												
20RT18	z5	7.855	0.064	601.3	1.59	0.98	0.87	1.13	73.44	0.515	1.208E-03	0.80
20RT18	z8	7.881	0.048	319.9	1.95	0.56	0.29	1.93	105.42	0.630	1.214E-03	0.55
20RT18	z10	7.886	0.035	676.7	2.35	1.28	0.40	3.22	153.17	0.756	1.216E-03	0.32
20RT18	z12	7.932	0.069	421.0	2.66	0.85	0.49	1.73	87.18	0.857	1.224E-03	0.80
20RT18	z17	7.902	0.037	1008.0	2.84	2.08	0.44	4.69	198.39	0.915	1.220E-03	0.26
20RT18	z26	7.918	0.043	670.1	2.96	1.42	0.41	3.42	147.34	0.953	1.223E-03	0.36
20RT18	z29	7.955	0.066	602.0	2.13	1.10	0.88	1.25	73.30	0.686	1.226E-03	0.80
Granite of Deadman Pass (GDP)												
DVCC18-3	L2	8.175	0.019	1417.3	0.91	2.05	0.56	3.66	225.37	0.295	1.255E-03	0.22
DVCC18-3	z2	7.945	0.044	517.9	1.16	0.77	0.51	1.51	99.51	0.375	1.220E-03	0.56
DVCC18-3	z4	7.876	0.086	324.0	1.26	0.49	0.64	0.77	59.09	0.407	1.209E-03	1.11
DVCC18-3	z5	7.964	0.077	247.2	0.89	0.35	0.45	0.78	62.97	0.289	1.222E-03	0.98
Little Chief Granite												
Little Chief Granite, north facies (LCG-N)												
LCN	51304	11.319	0.078	4815.2	0.92	9.71	4.70	2.07	130.60	0.295	1.745E-03	0.68
LCN	51305	11.292	0.061	1993.8	1.12	4.21	1.46	2.88	167.31	0.362	1.742E-03	0.51
LCN	51307	11.365	0.110	17337.6	1.05	36.25	4.89	7.41	407.24	0.338	1.753E-03	0.96
LCN	51309	11.281	0.057	1895.6	1.06	3.95	2.01	1.96	121.32	0.342	1.740E-03	0.49
LCN	51312	11.303	0.039	2206.4	1.07	4.62	1.66	2.79	164.04	0.346	1.743E-03	0.31
LCN	091501	11.373	0.060	568.4	1.01	1.18	0.61	1.93	122.68	0.325	1.754E-03	0.51
LCN	091507	11.443	0.075	673.6	1.00	1.41	1.02	1.38	93.09	0.322	1.765E-03	0.65
LCN	091508	11.557	0.061	884.8	1.10	1.91	0.62	3.07	180.17	0.355	1.783E-03	0.51
Little Chief Granite, south facies (LCG-S)												
LCS	041313	11.457	0.027	2894.4	1.50	6.75	1.44	4.69	239.32	0.482	1.769E-03	0.21
LCS	090913	11.438	0.057	1485.1	1.38	3.38	1.62	2.08	119.97	0.446	1.766E-03	0.46
LCS	090914	11.493	0.040	1739.1	1.06	3.69	1.54	2.39	143.53	0.341	1.773E-03	0.31
LCS	F-3	11.418	0.066	975.4	2.29	2.65	1.13	2.35	117.86	0.737	1.767E-03	0.46
LCS	F-5	11.401	0.054	819.5	1.59	1.94	0.88	2.21	125.76	0.511	1.761E-03	0.41
LCS	F-6	11.439	0.066	1021.5	1.80	2.53	1.32	1.92	107.54	0.579	1.768E-03	0.51
LCS	F-7	11.436	0.034	1792.0	1.47	4.14	0.84	4.92	262.77	0.472	1.766E-03	0.19
LCS	F-8	11.398	0.046	2059.7	1.44	4.72	1.79	2.63	150.22	0.463	1.760E-03	0.34
LCS	F-10	11.397	0.088	956.3	2.45	2.67	1.68	1.59	84.09	0.788	1.765E-03	0.68
Kingston Range Granite												
Kingston Range Granite, feldspar porphyry facies (KRG-F)												
KRG_north	090802	12.516	0.042	4596.6	0.84	10.05	2.54	3.96	241.75	0.270	1.931E-03	0.32
KRG_north	090808	12.444	0.033	11204.1	0.80	24.17	5.46	4.43	270.04	0.259	1.919E-03	0.24
KRG_north	090814	12.493	0.045	2740.0	0.90	6.07	2.81	2.16	138.57	0.288	1.927E-03	0.34
KRG_north	090815	12.585	0.055	4708.7	0.83	10.33	5.66	1.83	121.80	0.267	1.941E-03	0.43
KRG_north	KRG2220	12.470	0.043	1544.7	0.53	3.12	1.46	2.13	150.36	0.171	1.922E-03	0.34
KRG_north	KRG050107	13.072	0.068	659.2	1.22	1.65	0.89	1.86	112.44	0.394	2.019E-03	0.50
KRG_north	KRG050108	13.078	0.094	450.1	0.93	1.06	0.93	1.14	79.83	0.300	2.018E-03	0.72
KRG_north	KRG050109	13.149	0.121	541.9	0.98	1.30	0.92	1.41	93.73	0.317	2.030E-03	0.92
KRG_north	KRG050111	13.164	0.029	1192.9	0.85	2.76	0.53	5.18	303.02	0.274	2.031E-03	0.20
KRG_north	KRG051015	12.605	0.043	1858.9	1.23	4.50	1.55	2.90	164.60	0.395	1.946E-03	0.30
KRG_north	KRG0125011	13.096	0.047	728.4	0.71	1.62	0.71	2.28	148.35	0.228	2.020E-03	0.36
KRG_north	KRGK3	12.634	0.059	1927.2	1.08	4.52	2.55	1.77	110.74	0.347	1.950E-03	0.45
KRG_north	KRGo4	12.632	0.064	2510.6	0.89	5.62	1.97	2.86	174.18	0.286	1.949E-03	0.50
Kingston Range Granite, quartz porphyry facies (KRG-Q)												
KRG_north	090812	12.223	0.027	14109.3	0.70	29.10	7.38	3.94	248.54	0.224	1.884E-03	0.20
KRG_north	090804	12.171	0.033	4589.4	0.54	9.04	3.44	2.63	178.42	0.174	1.875E-03	0.26
KRG_north	090807	12.214	0.025	6338.9	0.84	13.56	2.16	6.28	371.29	0.272	1.884E-03	0.17

KRG_north	KRG012505	12.197	0.065	3428.2	0.88	7.40	5.14	1.44	97.17	0.282	1.881E-03	0.53
KRG_north	KRN-13M	12.071	0.050	1522.0	0.98	3.32	1.50	2.21	141.21	0.314	1.862E-03	0.40
KRG_south	090904	12.119	0.114	621.5	1.20	1.44	1.55	0.93	65.73	0.388	1.871E-03	0.94
KRG_south	090905	12.113	0.110	500.1	1.44	1.22	1.17	1.04	68.54	0.464	1.871E-03	0.90
KRG_south	090906	12.139	0.118	699.7	1.28	1.66	2.14	0.77	56.98	0.414	1.874E-03	0.98
KRG_south	090907	12.127	0.133	615.0	0.92	1.34	1.86	0.72	57.35	0.297	1.871E-03	1.11
KRG_south	090908	12.144	0.160	853.8	1.45	2.10	2.91	0.72	53.15	0.468	1.876E-03	1.32
KRG_south	090909	12.102	0.167	498.2	1.00	1.10	2.00	0.55	47.76	0.321	1.867E-03	1.40
KRG_south	K1209162001	12.128	0.026	1420.0	0.98	3.12	0.41	7.60	441.11	0.316	1.871E-03	0.16
KRG_south	K1209162002	12.100	0.077	662.8	1.07	1.48	1.08	1.37	93.85	0.344	1.867E-03	0.63
KRG_south	K1209162003	12.147	0.057	1479.3	1.03	3.29	1.47	2.24	142.26	0.331	1.874E-03	0.45
KRG_south	K1209162004	12.105	0.038	1659.2	1.26	3.88	0.77	5.05	282.11	0.405	1.869E-03	0.25
KRG_south	K1209162005	12.092	0.031	2241.3	0.96	4.88	1.23	3.98	241.05	0.310	1.865E-03	0.22
KRG_south	K1209162006	12.094	0.051	1311.0	0.93	2.83	1.54	1.84	122.72	0.300	1.865E-03	0.41
KRG_south	K1209162008	12.239	0.032	2223.9	0.83	4.75	1.21	3.93	245.58	0.267	1.887E-03	0.24
KRG_south	K1209162009	12.085	0.096	1017.5	1.35	2.42	1.88	1.29	84.84	0.434	1.866E-03	0.78
KRG_south	K1209162011	12.362	0.051	685.1	1.80	1.83	0.59	3.11	163.83	0.578	1.911E-03	0.33
Granite of Rabbit Holes Spring, gray monzogranite phase (GHRS)												
RH420	RH420	12.01	0.13	274.5	1.39	0.655	0.84	0.78	59	0.446	1.855E-03	1
RH420	RH421	11.91	0.1	801.6	1.97	2.14	1.77	1.21	73	0.633	1.842E-03	0.8
RH420	RH422	12.018	0.078	1198.7	1.09	2.67	1.95	1.37	93	0.351	1.854E-03	0.64
RH420	RH423	11.975	0.065	629.0	1.15	1.42	0.93	1.53	100	0.370	1.848E-03	0.52
RH420	RH424	12.082	0.064	972.3	0.85	2.06	1.47	1.40	100	0.273	1.863E-03	0.53
RH420	RH425	11.92	0.13	727.6	1	1.57	2.25	0.70	58	0.322	1.838E-03	1.1
RH420	RH426	11.91	0.15	289.0	1.2	0.655	1.05	0.62	52	0.386	1.839E-03	1.3
RH420	RH427	11.878	0.037	1237.7	0.74	2.51	1.02	2.46	164	0.239	1.831E-03	0.3
RH420	RH428	11.807	0.049	1406.8	1.42	3.32	1.41	2.35	138	0.458	1.823E-03	0.36
RH420	RH429	11.88	0.11	329.0	0.92	0.697	0.85	0.82	65	0.298	1.832E-03	0.93
RH420	RH430	12.115	0.084	498.8	0.93	1.08	0.98	1.10	81	0.301	1.869E-03	0.69
RH420	RH431	11.978	0.038	2202.6	0.95	4.74	1.84	2.58	163	0.307	1.848E-03	0.29
RH420	RH432	11.965	0.018	2887.8	0.94	6.19	0.26	23.81	1338	0.302	1.846E-03	0.066
RH420	RH433	11.914	0.028	1809.6	0.92	3.85	0.82	4.70	283	0.297	1.837E-03	0.19
RH420	RH434	11.914	0.021	6625.0	1.11	14.7	0.63	23.33	1288	0.359	1.838E-03	0.068
RH420	RH435	11.936	0.028	5840.1	1.19	13.3	2.4	5.54	311	0.385	1.842E-03	0.16
RH420	RH436	12.108	0.022	9657.2	1.01	21.3	0.97	21.96	1235	0.325	1.868E-03	0.11
RH420	RH437	11.918	0.065	1493.7	0.87	3.14	2.29	1.37	97	0.282	1.838E-03	0.54
RH420	RH438	11.983	0.026	1332.2	1.16	3.02	0.41	7.37	412	0.374	1.849E-03	0.13
RH420	RH439	11.962	0.028	4297.8	0.9	9.13	0.88	10.38	607	0.29	1.845E-03	0.2
RH420	RH440	12.26	0.14	246.7	1.18	0.572	0.8	0.72	57	0.379	1.893E-03	1.1
RH420	RH441	12.104	0.09	848.6	1.07	1.9	1.59	1.19	84	0.346	1.868E-03	0.74
RH420	RH442	12.087	0.06	719.2	0.79	1.5	0.95	1.58	111	0.254	1.864E-03	0.5

Note: CA-ID-TIMS—chemical abrasion–isotope dilution–thermal ionization mass spectrometry; abs.— absolute

[a]Corrected for initial Th/U disequilibrium using radiogenic ^{208}Pb and Th/U_{magma} are listed in Table S2.

[b]Th contents calculated from radiogenic ^{208}Pb and ^{230}Th-corrected $^{206}Pb/^{238}U$ date of the sample, assuming concordance between U-Pb and Th-Pb systems.

[c]Total mass of radiogenic Pb.

[d]Total mass of common Pb.

[e]Ratio of radiogenic Pb (including ^{208}Pb) to common Pb.

[f]Measured ratio corrected for fractionation and spike contribution only.

[g]Measured ratios corrected for fractionation, tracer, and blank.

TABLE 4. ZIRCON WEIGHTED MEAN AGES WITH ASSOCIATED MSWD AND THE MAXIMUM (t_{max}), MINIMUM (t_{min}), AND Δt OF ZIRCON AGE DISTRIBUTION BASED ON THE BAYESIAN ALGORITHM OF CHRON.JL (KELLER ET AL., 2018)

Sample ID	Abbreviated sample name	Rock name	Weighted mean age (Ma)	Weighted mean age error (2σ abs.) (m.y.)	MSWD	n_{Dates}	t_{min} (Ma; 95% CI)	t_{max} (Ma; 95% CI)	Δt (m.y.; 95% CI)
KRG_north	KRG-F	Kingston Peak Granite (feldspar porphyry facies)	12.729	0.170	171.7	13	12.442 +0.029/−0.125	13.166 +0.136/−0.028	0.742 +0.186/−0.052
KRG_south	KRG-Q	Kingston Peak Granite (quartz porphyry facies)	12.168	0.031	9.8	20	12.067 +0.025/−0.057	12.336 +0.055/−0.064	0.281 +0.077/−0.081
RH420	GRHS	Granite of Rabbit Holes Spring	11.981	0.031	15.6	23	11.830 +0.055/−0.042	12.148 +0.091/−0.038	0.320 +0.107/−0.072
LCS	LCG-S	Little Chief Granite (southern facies)	11.442	0.021	2.0	9	11.397 +0.045/−0.047	11.479 +0.040/−0.038	0.085 +0.061/−0.085
LCN	LCG-N	Little Chief Granite (northern facies)	11.353	0.067	9.7	8	11.274 +0.033/−0.103	11.557 +0.093/−0.070	0.291 +0.148/−0.083
DVCC18-2	Lower WSD	Willow Spring Diorite	10.978	0.112	185.7	13	10.491 +0.038/−0.130	11.260 +0.115/−0.024	0.786 +0.178/−0.055
DVCC18-5	Upper WSD	Willow Spring Diorite	10.085	0.020	0.6	7	10.084 +0.015/−0.052	10.086 +0.046/−0.015	0.0013 +0.0765/−0.0013
DVCC18-14	Middle WSD	Willow Spring Diorite	10.374	0.021	3.2	12	10.319 +0.046/−0.117	10.550 +0.080/−0.159	0.25 +0.15/−0.21
DVCC18-9	SMG-F	Smith Mountain Granite (fine-grained facies)	10.480	0.122	44.1	7	10.247 +0.040/−0.162	10.81 +0.20/−0.21	0.58 +0.28/−0.21
DVCC18-10	SMG-C	Smith Mountain Granite (coarse-grained facies)	10.503	0.047	13.5	6	10.402 +0.027/−0.070	10.547 +0.069/−0.021	0.151 +0.105/−0.037
DVCC18-8	QGV	Quartz monzonite of Gold Valley	10.431	0.053	41.5	10	10.193 +0.051/−0.145	10.82 +0.16/−0.10	0.64 +0.22/−0.12
20RT18	DFS	Diorite of Furnace site	7.900	0.020	1.2	7	7.896 +0.017/−0.048	7.902 +0.057/−0.015	0.0019 +0.0942/−0.0019
DVCC18-3	GDP	Granite of Deadman Pass	8.122	0.116	48.7	4	7.875 +0.068/−0.178	8.176 +0.111/−0.019	0.309 +0.237/−0.070

Note: Time (t_{max} and t_{min}) estimates represent the time at which the magmatic system reaches zircon saturation and the solidus, respectively. Crystallization time scales (Δt) are the mode of the kernel density estimation distribution of $t_{max} - t_{min}$. All are reported within 95% confidence interval (CI). abs.—absolute; MSWD—mean square of weighted deviates.

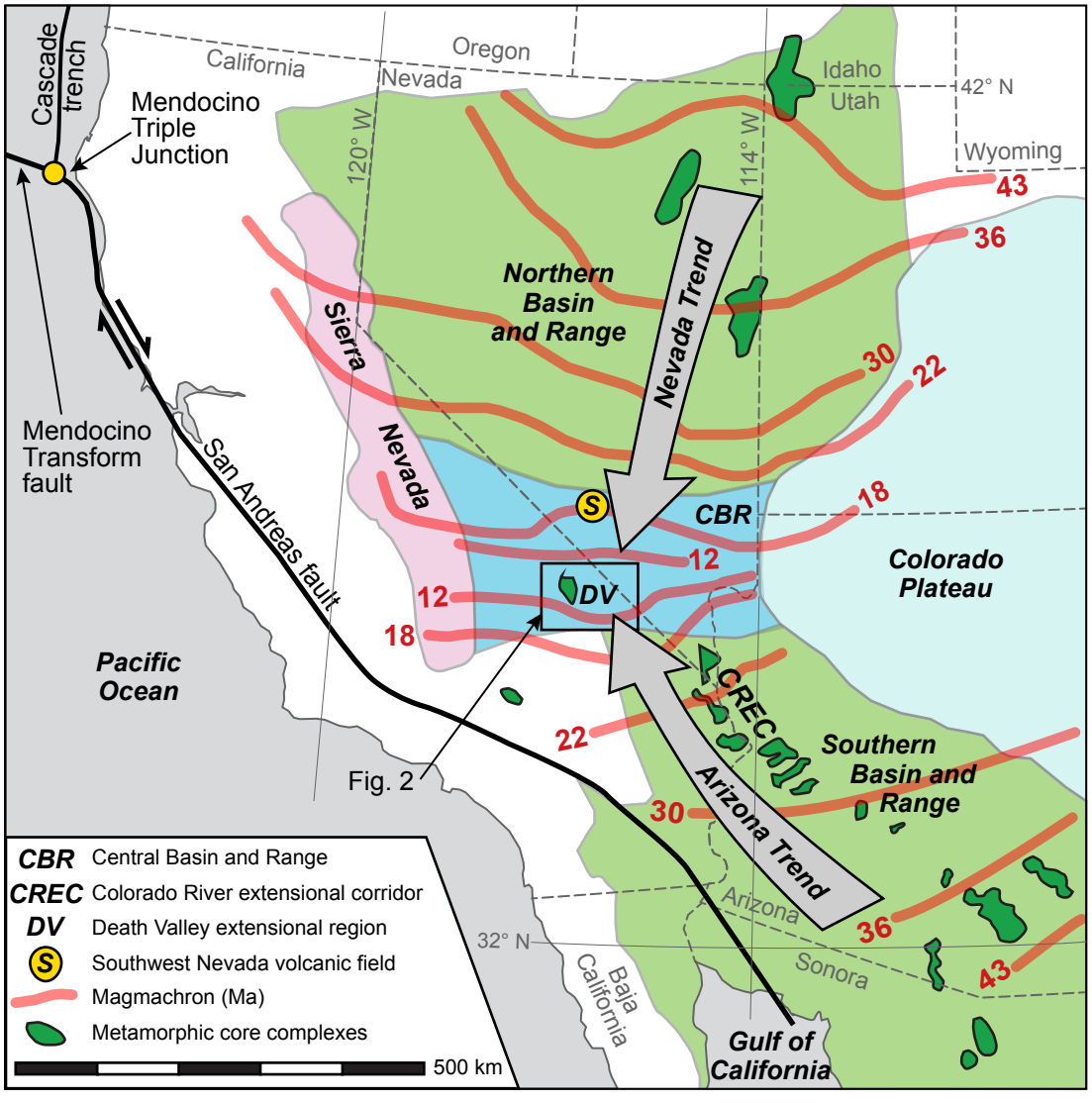
Cascade trench
California
Oregon
Nevada
Idaho
Utah
Wyoming
42° N
120° W
114° W
Mendocino Triple Junction
Mendocino Transform fault
San Andreas fault
Sierra Nevada
Northern Basin and Range
Nevada Trend
CBR
DV
Colorado Plateau
CREC
Arizona Trend
Southern Basin and Range
Pacific Ocean
Fig. 2
Arizona
Sonora
32° N
Baja California
Gulf of California
43
36
30
22
18
12
CBR Central Basin and Range
CREC Colorado River extensional corridor
DV Death Valley extensional region
S Southwest Nevada volcanic field
Magmachron (Ma)
Metamorphic core complexes
500 km

Figure 1.

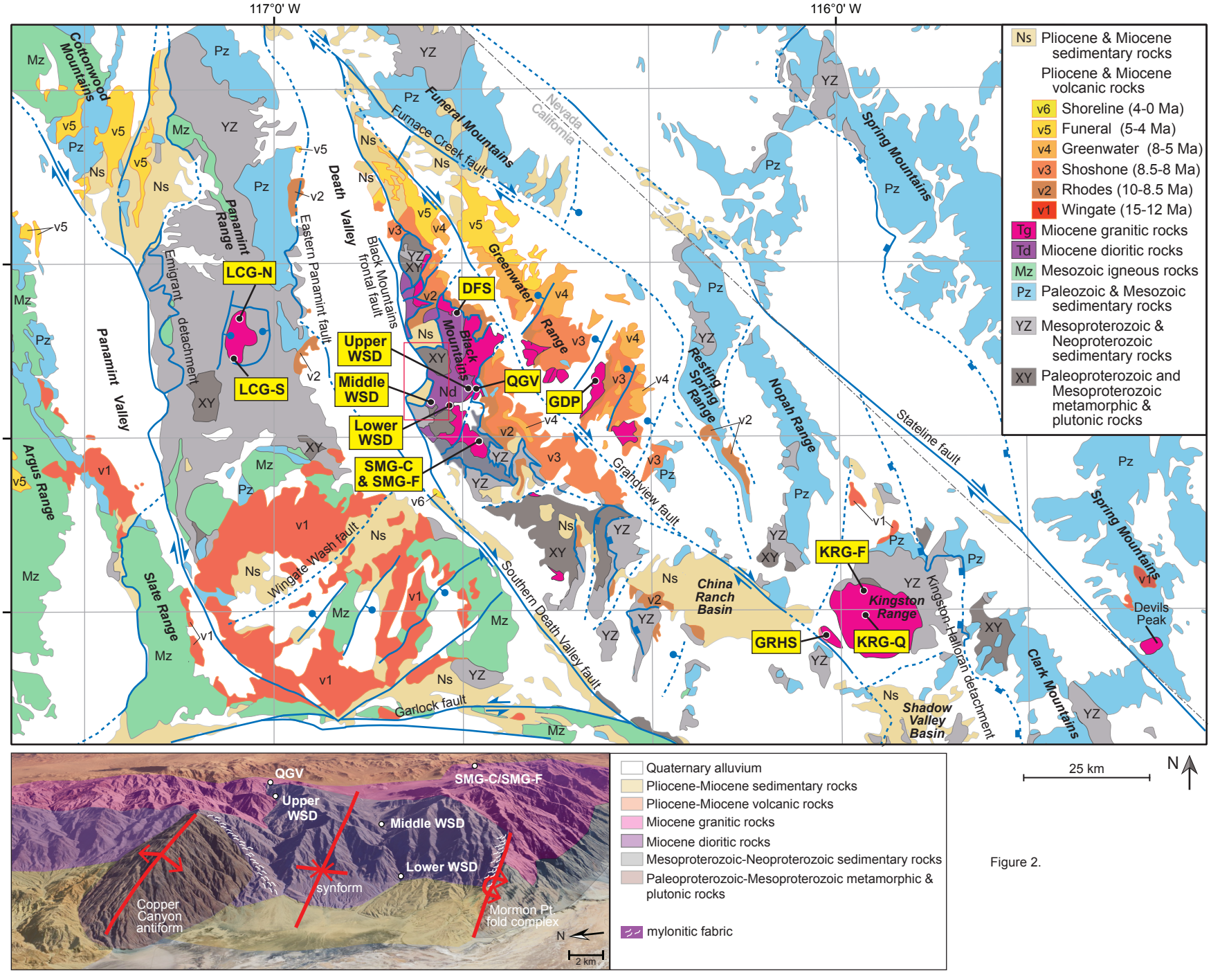
117°0' W
116°0' W
36°15' N
36°0' N
35°45' N
Ns Pliocene & Miocene sedimentary rocks
Pliocene & Miocene volcanic rocks
v6 Shoreline (4-0 Ma)
v5 Funeral (5-4 Ma)
v4 Greenwater (8-5 Ma)
v3 Shoshone (8.5-8 Ma)
v2 Rhodes (10-8.5 Ma)
v1 Wingate (15-12 Ma)
Tg Miocene granitic rocks
Td Miocene dioritic rocks
Mz Mesozoic igneous rocks
Pz Paleozoic & Mesozoic sedimentary rocks
YZ Mesoproterozoic & Neoproterozoic sedimentary rocks
XY Paleoproterozoic and Mesoproterozoic metamorphic & plutonic rocks
LCG-N
LCG-S
DFS
Upper WSD
Middle WSD
Lower WSD
QGV
GDP
SMG-C & SMG-F
KRG-F
KRG-Q
GRHS
Cottonwood Mountains
Panamint Range
Panamint Valley
Emigrant detachment
Eastern Panamint fault
Death Valley
Black Mountains frontal fault
Black Mountains
Funeral Mountains
Furnace Creek fault
Nevada
California
Greenwater Range
Resting Spring Range
Nopah Range
Spring Mountains
Stateline fault
Grapevine fault
Argus Range
Slate Range
Wingate Wash fault
Southern Death Valley fault
Garlock fault
China Ranch Basin
Kingston Range
Kingston-Halloran detachment
Shadow Valley Basin
Clark Mountains
Devils Peak
25 km
N
QGV
Upper WSD
SMG-C/SMG-F
Middle WSD
Lower WSD
synform
Copper Canyon antiform
Mormon Pt. fold complex
N
2 km
Quaternary alluvium
Pliocene-Miocene sedimentary rocks
Pliocene-Miocene volcanic rocks
Miocene granitic rocks
Miocene dioritic rocks
Mesoproterozoic-Neoproterozoic sedimentary rocks
Paleoproterozoic-Mesoproterozoic metamorphic & plutonic rocks
mylonitic fabric

Figure 2.

Figure 3.

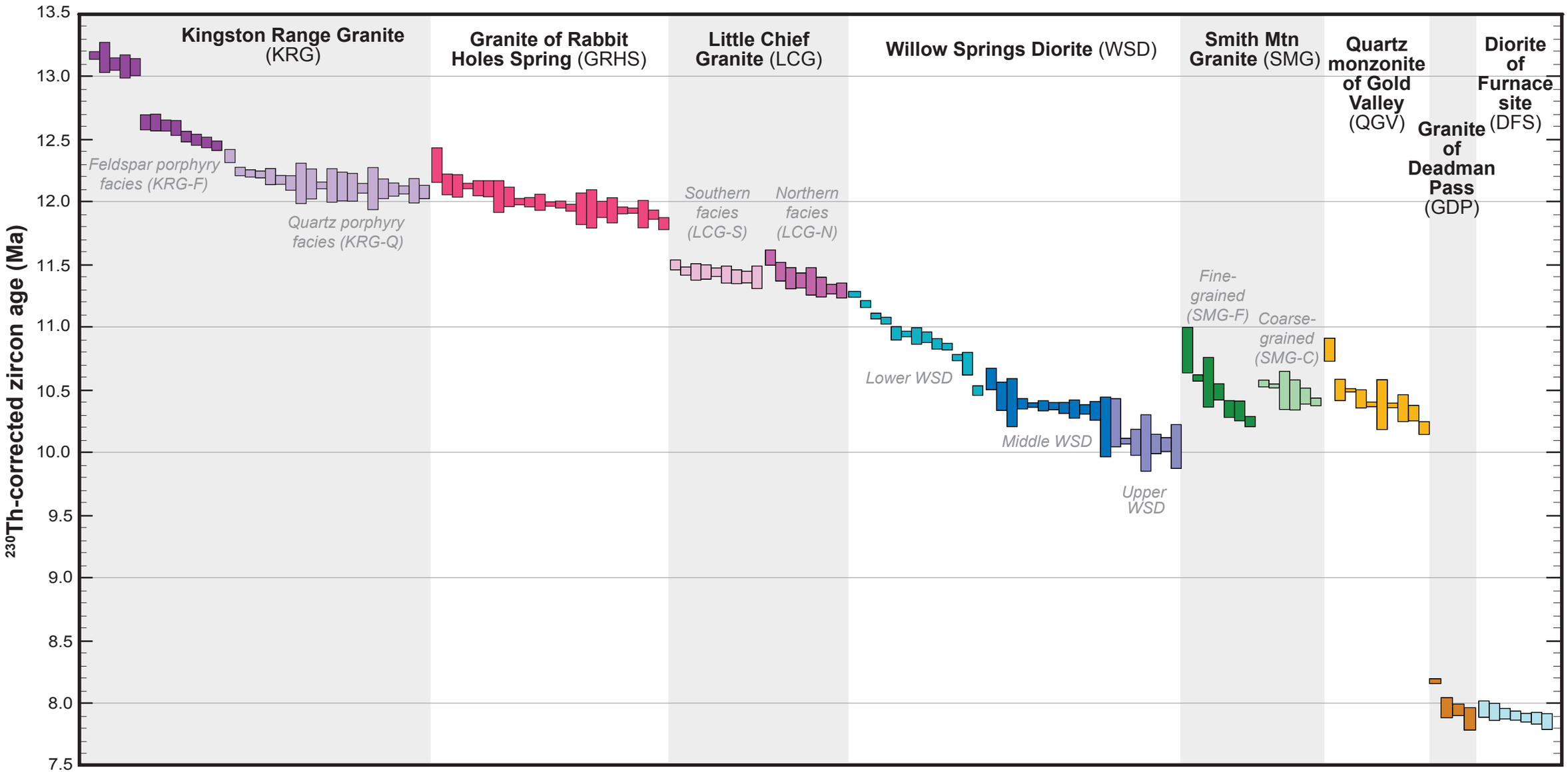
Kingston Range Granite (KRG)
Granite of Rabbit Holes Spring (GRHS)
Little Chief Granite (LCG)
Willow Springs Diorite (WSD)
Smith Mtn Granite (SMG)
Quartz monzonite of Gold Valley (QGV)
Granite of Deadman Pass (GDP)
Diorite of Furnace site (DFS)
Feldspar porphyry facies (KRG-F)
Quartz porphyry facies (KRG-Q)
Southern facies (LCG-S)
Northern facies (LCG-N)
Lower WSD
Middle WSD
Upper WSD
Fine-grained (SMG-F)
Coarse-grained (SMG-C)
230Th-corrected zircon age (Ma)
13.5
13.0
12.5
12.0
11.5
11.0
10.5
10.0
9.5
9.0
8.5
8.0
7.5

Figure 4.

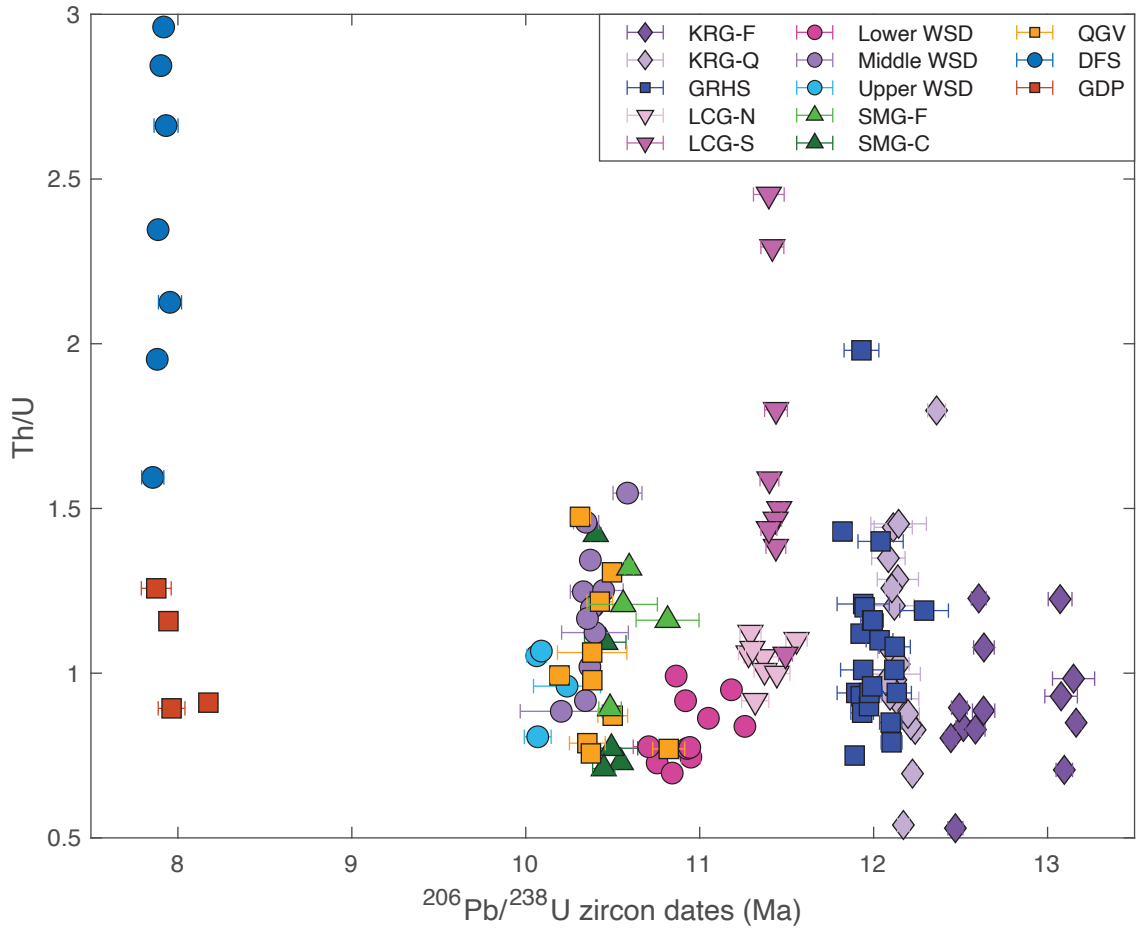
KRG-F
KRG-Q
GRHS
LCG-N
LCG-S
Lower WSD
Middle WSD
Upper WSD
SMG-F
SMG-C
QGV
DFS
GDP
Th/U
3
2.5
2
1.5
1
0.5
8
9
10
11
12
13
206Pb/238U zircon dates (Ma)

Figure 5.

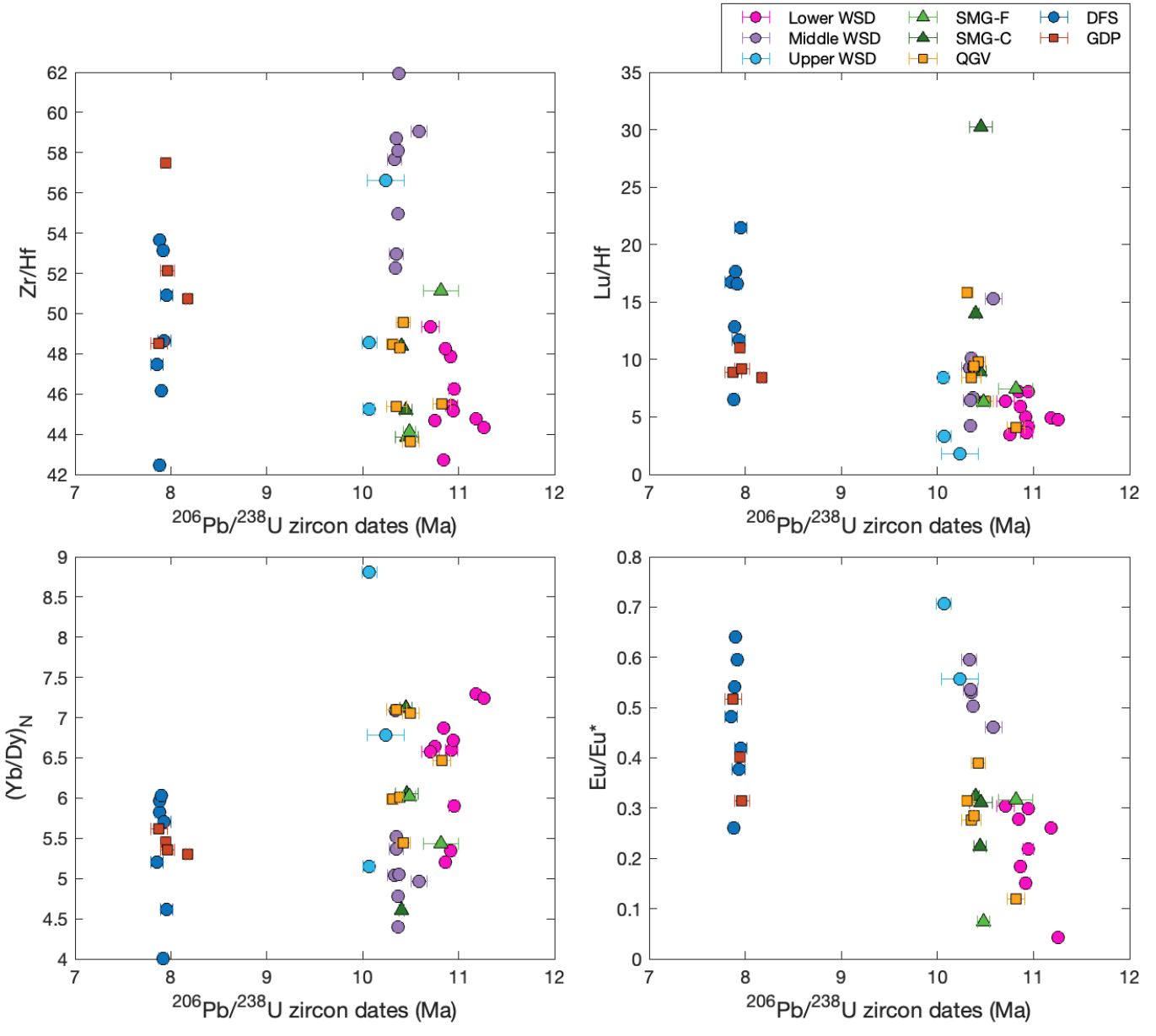
Lower WSD
Middle WSD
Upper WSD
SMG-F
SMG-C
QGV
DFS
GDP
Zr/Hf
Lu/Hf
(Yb/Dy)N
Eu/Eu*
206Pb/238U zircon dates (Ma)

Figure 6.

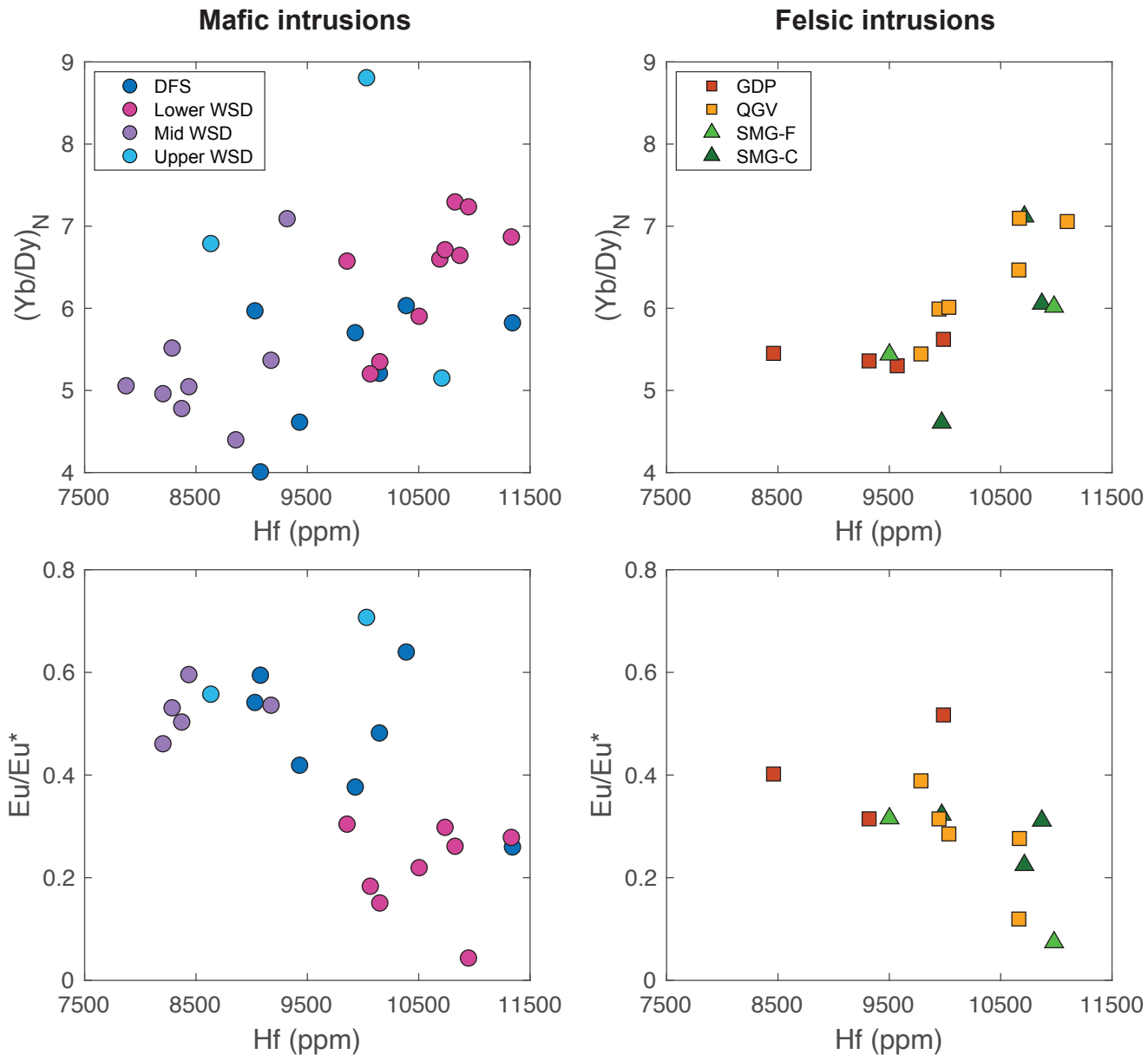
Mafic intrusions
Felsic intrusions
DFS
Lower WSD
Mid WSD
Upper WSD
GDP
QGV
SMG-F
SMG-C
(Yb/Dy)N
Eu/Eu*
Hf (ppm)
9
8
7
6
5
4
0.8
0.6
0.4
0.2
0
7500
8500
9500
10500
11500

Figure 7.

P1: Early granite plutonism—Devil Peak intrusion, Kingston Range Granite, granite of Rabbit Holes Spring, and Little Chief Granite (13.2–11.3 Ma)

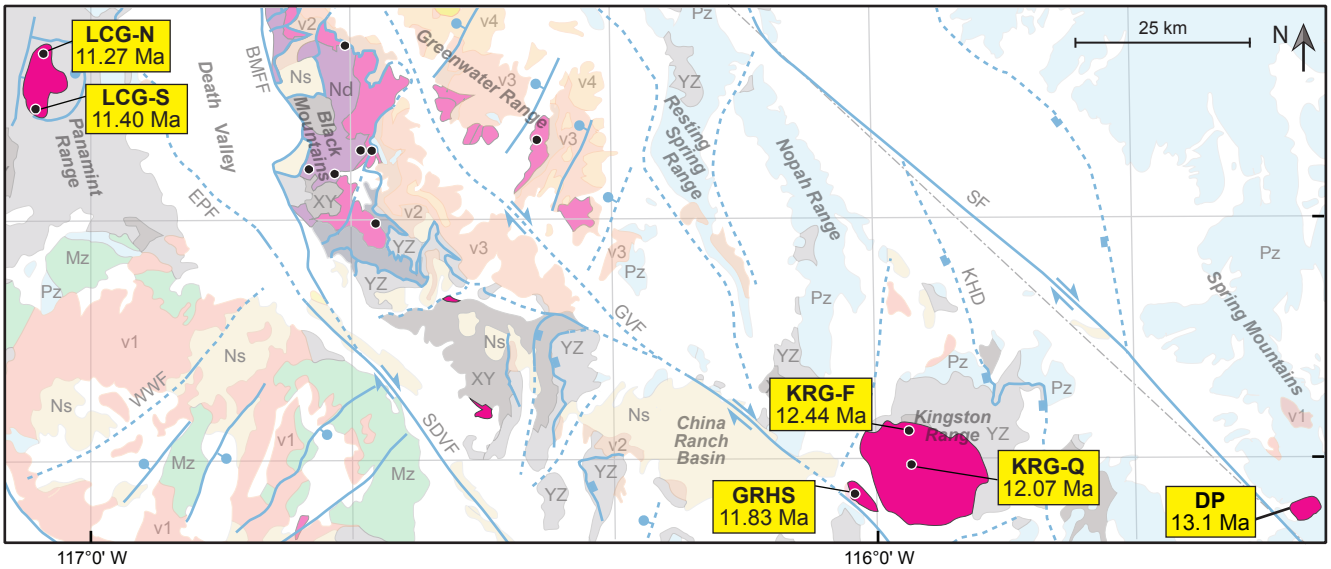

P2: Black Mtn intrusive complex—Willow Spring Diorite, Smith Mtn Granite, and quartz monzonite of Gold Valley (11.3–10.1 Ma)

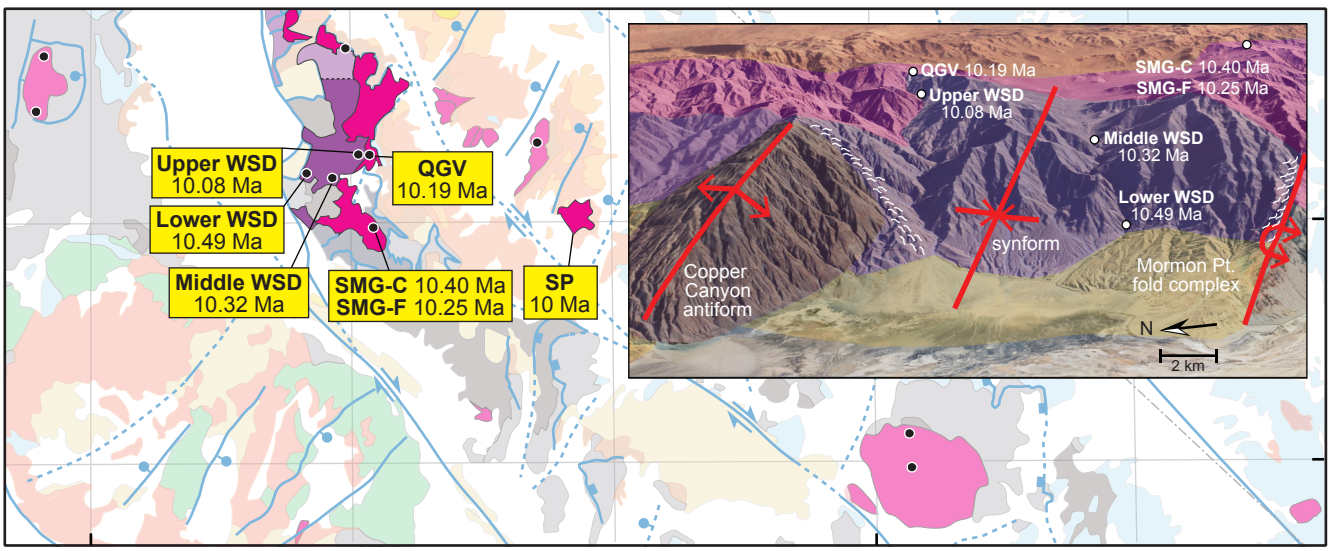

P3: Late plutonism—diorite of Furnace Site and granite of Deadman Pass (8.2–7.9 Ma)

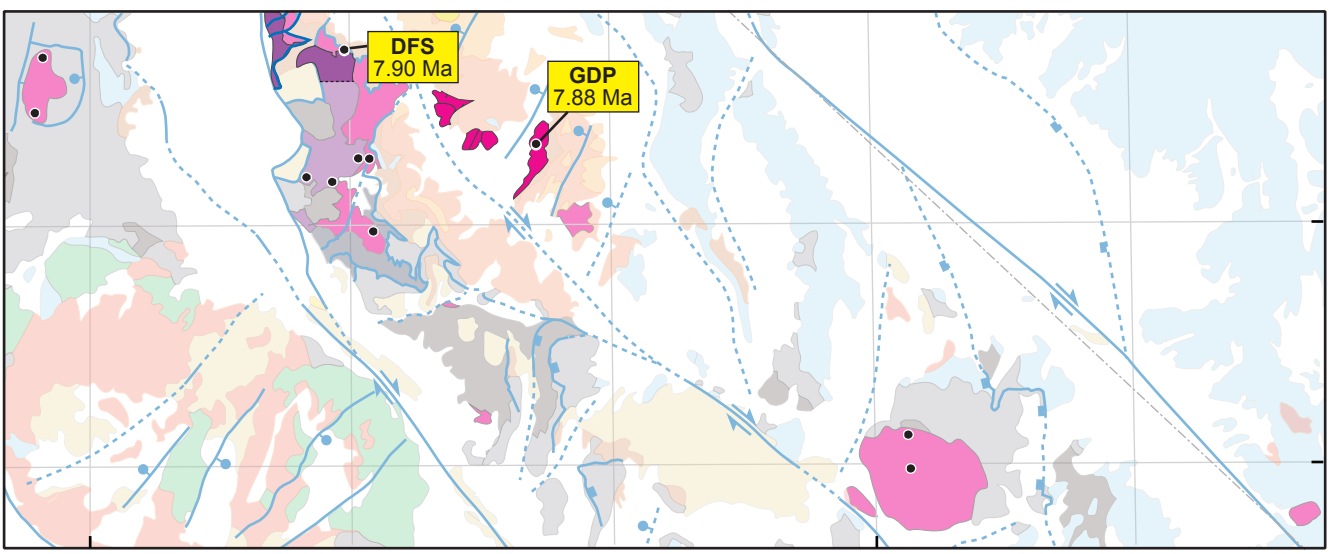

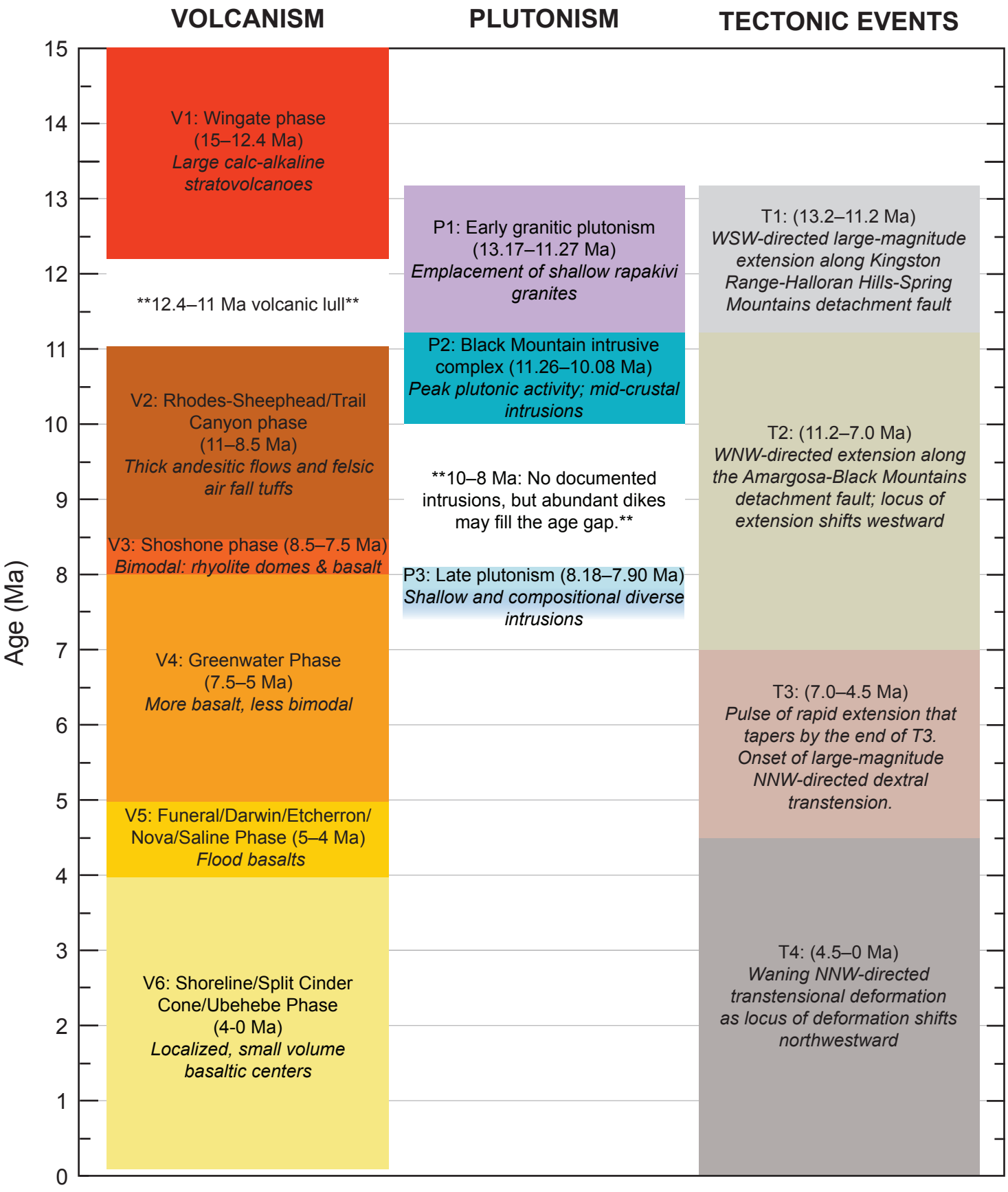
VOLCANISM
PLUTONISM
TECTONIC EVENTS
Age (Ma)
15
14
13
12
11
10
9
8
7
6
5
4
3
2
1
0
V1: Wingate phase (15–12.4 Ma) Large calc-alkaline stratovolcanoes
12.4–11 Ma volcanic lull
V2: Rhodes-Sheephead/Trail Canyon phase (11–8.5 Ma) Thick andesitic flows and felsic air fall tuffs
V3: Shoshone phase (8.5–7.5 Ma) Bimodal: rhyolite domes & basalt
V4: Greenwater Phase (7.5–5 Ma) More basalt, less bimodal
V5: Funeral/Darwin/Etcherron/ Nova/Saline Phase (5–4 Ma) Flood basalts
V6: Shoreline/Split Cinder Cone/Ubehebe Phase (4-0 Ma) Localized, small volume basaltic centers
P1: Early granitic plutonism (13.17–11.27 Ma) Emplacement of shallow rapakivi granites
P2: Black Mountain intrusive complex (11.26–10.08 Ma) Peak plutonic activity; mid-crustal intrusions
10–8 Ma: No documented intrusions, but abundant dikes may fill the age gap.
P3: Late plutonism (8.18–7.90 Ma) Shallow and compositional diverse intrusions
T1: (13.2–11.2 Ma) WSW-directed large-magnitude extension along Kingston Range-Halloran Hills-Spring Mountains detachment fault
T2: (11.2–7.0 Ma) WNW-directed extension along the Amargosa-Black Mountains detachment fault; locus of extension shifts westward
T3: (7.0–4.5 Ma) Pulse of rapid extension that tapers by the end of T3. Onset of large-magnitude NNW-directed dextral transtension.
T4: (4.5–0 Ma) Waning NNW-directed transtensional deformation as locus of deformation shifts northwestward

Figure 8.

FIELD DESCRIPTIONS + PHOTOS

Willow Spring Diorite

Three samples were collected for different structural levels within the Black Mountains (lower Willow Spring Diorite, middle Willow Spring Diorite and upper Willow Spring Diorite).

Lower Willow Spring Diorite (DVCC18-2): This sample was collected from the lower section of Sheep Canyon (left photo). DVCC18-2 was sampled from a more leucocratic zone within a larger gabbroic unit. *Note*: this sample is located several hundred feet above the pluton floor so "lower" is a relative term used in this study. At this site, the intrusion looks highly mixed with blebs and lens with varying grain size (right photo).

Middle Willow Spring Diorite (DVCC18-14): This sample was collected from the Willow Spring Type locality. At the type locality, you can see multiple intrusive generations of the Willow Spring Diorite (right photo). DVCC18-14 sample was collected from a coarser-grained dioritic phase within the finer-grained diorite (left photo).

Upper Willow Spring Diorite (DVCC18-5): Sample was collected from the upper section of Sheep Canyon. DVCC18-5 was collected from a coarser-grained dioritic region within a finer-grained diorite. This plagioclase-biotite diorite is slightly altered with biotite chloritization present but no mylonitic textures were observed.

<u>Smith Mountain Granite</u>

Two samples were collected from the Smith Mountain Granite (SMG).

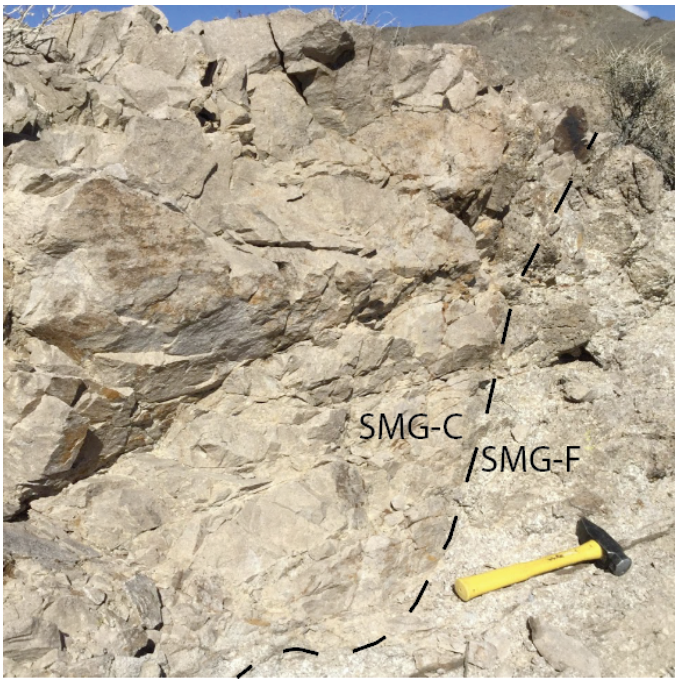

Two samples were collected from a Smith Mountain outcrop located 50 ft from each other: coarser-grained **(SMG-C, DVCC18-10)** and finer-grained phase **(SMG-F, DVCC18-9)**. The contact between the two phases is sharp and undulatory though can appear nearly vertical in other places.

Quartz monzonite of Gold Valley

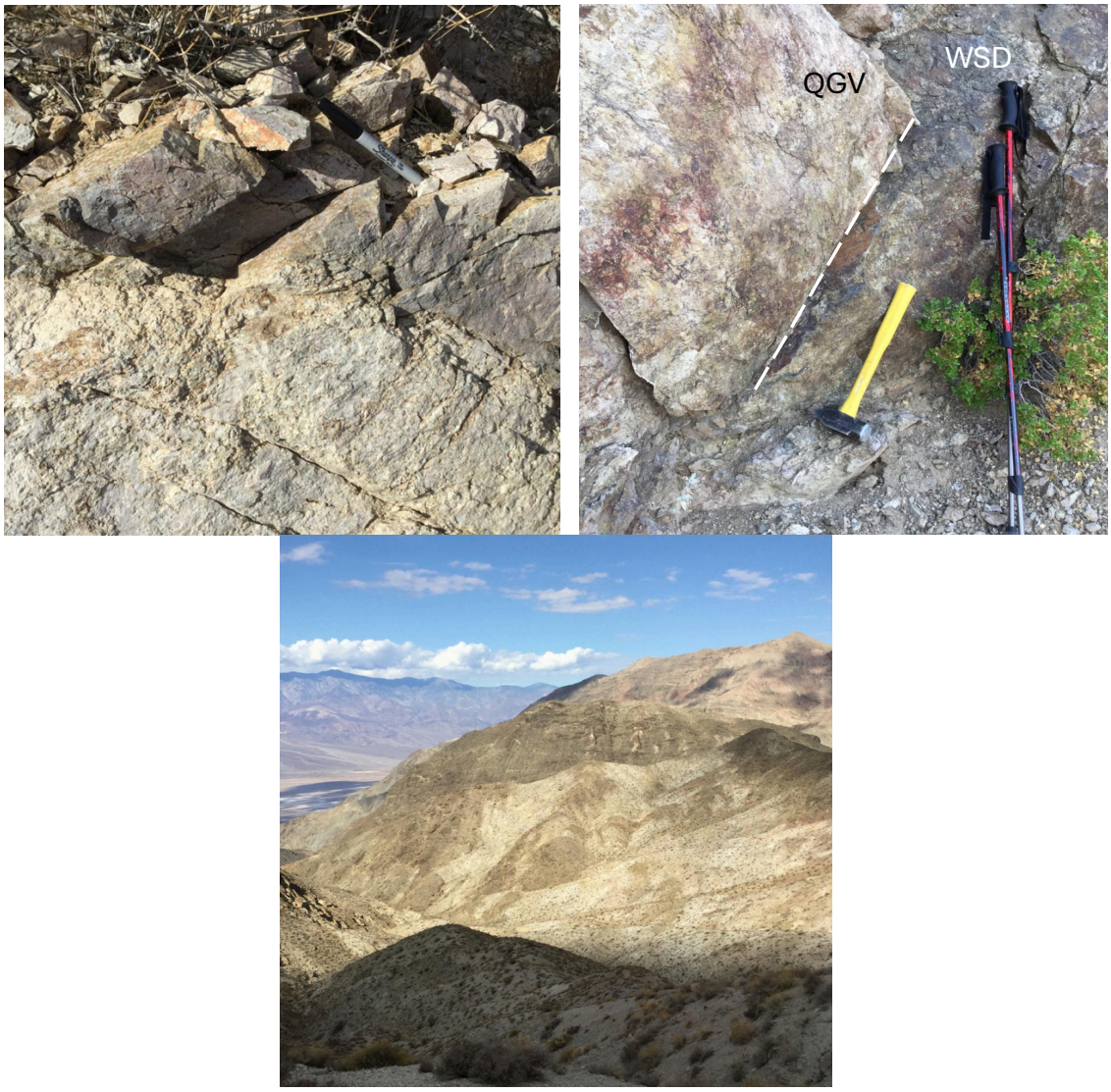

Sample DVCC18-8 was collected near the top of the Sheep Canyon saddle with Gold Valley (top left photo). This sample is a coarse-grained biotite-bearing quartz monzonite. It was found in contact with a finer-grained >10 cm dike. We did not observe rapakivi textures in this sample though Meuer (1992) mentioned rapakivi textures appear locally in the quartz monzonite of Gold Valley.

The contact between the Willow Spring Diorite and quartz monzonite of Gold Valley appears highly variable. The bottom photo is a view from near the DVCC18-8 outcrop, looking NW towards Death Valley. You can see complex interfingering between the darker-colored Willow Spring Diorite and the lighter-colored quartz monzonite of Gold Valley intrusions at higher structural levels in the Black Mountains. Closer to the main Willow

Spring Diorite body, ~0.38 km west of DVCC18-8, the contact forms a fault plane and both intrusions are highly altered (116.644933, 36.073472; top right photo).

Granite of Deadman Pass

Sample DVCC18-3 was collected from Deadman Pass in the Greenwater Range. DVCC18-3 is a medium-grained, porphyritic rapakivi granite. Collected a fresh sample however much of the granite here is sericitized and altered.

Kingston Range Granite

Two samples were collected from the Kingston Range Granite: Kingston Range Granite feldspar porphyry and Kingston Range Granite quartz porphyry

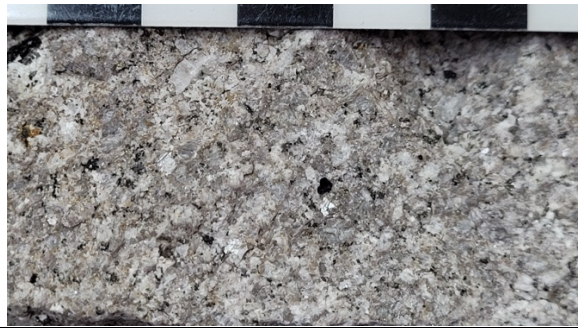

Samples KRG-N and **KRG-S** were collected from a canyon just below the peak of the Kingston Range (left photo). Bouldery weathering characteristics of the Kingston Range Granite prevents detailed observations or internal relationships for more than a few meters. These biotite-bearing granites (right photo) exhibit a rapakivi textures, white rims of

plagioclase around megacrysts of pinkish-gray potassium feldspar in a finer-grained matrix.

Little Chief Granite

Two samples were collected—southern facies and northern facies of the Little Chief Granite

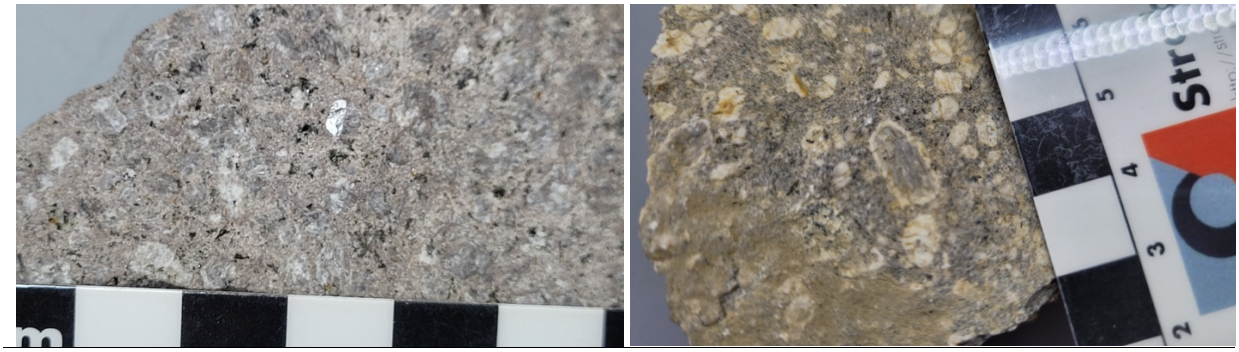

The northern facies (**LCN**) sample was collected ~2.4 km east of Telescope Peak while the southern facies (**LCS**) sample was collected ~2.2 km north of Sentinel Peak. The top right photo is a close-up of northern facies, and the top left photo is a close-up of southern facies. Rapakivi texture is easily seen with white rims of plagioclase around megacrysts of pinkish-gray potassium feldspar in a finer-grained matrix. Note the relatively abundant hornblende and biotite.

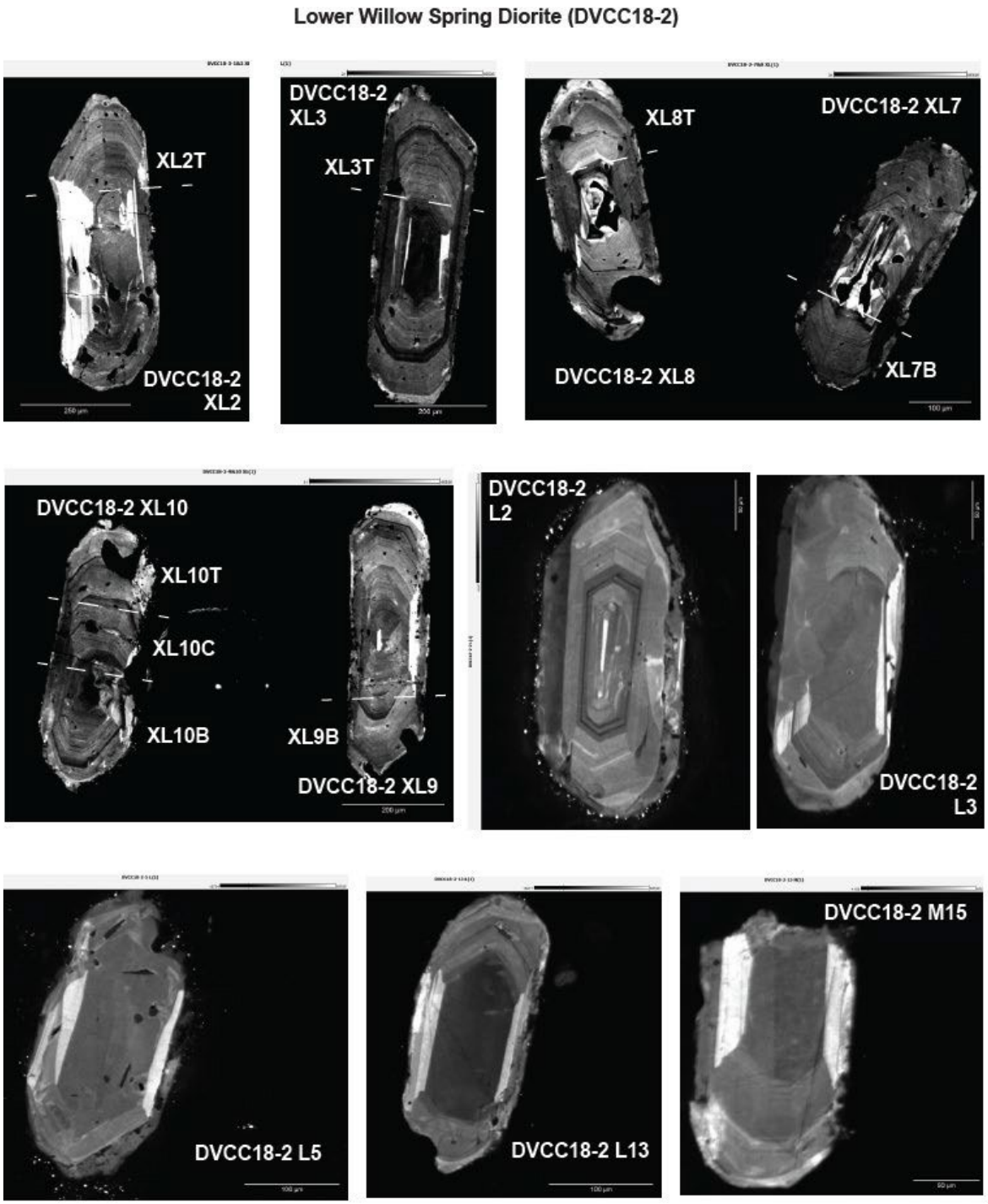

Figure S1. Cathodoluminscence (CL) images of dated zircon grains for the Willow Spring Diorite, Smith Mountain Granite, quartz monzonite of Gold Valley and granite of Deadman Pass. These zircon grains show typical oscillatory and sector zoning patterns. Smith Mountain Granite zircon typically have more well-defined oscillatory growth zoning though otherwise there is no appreciable zoning differences between different samples. Abrupt changes in CL zoning, indicating possible xenocrystic cores are rare and were avoided during sampling for ID-TIMS. Where imaged zircons have been dated, analysis names accompany the image, and where individual grains are microsampled, approximate locations of sample boundaries are indicated. Grain fractions that were large enough to break into multiple fragments were separated into two to three pieces and are indicated with a letter at the end of the fraction ID: (T), (C), and (B) correspond to top (tip), center, and bottom (other tip) fragments of a grain, respectively Dashed lines represent approximate region where an individual grain was broken.

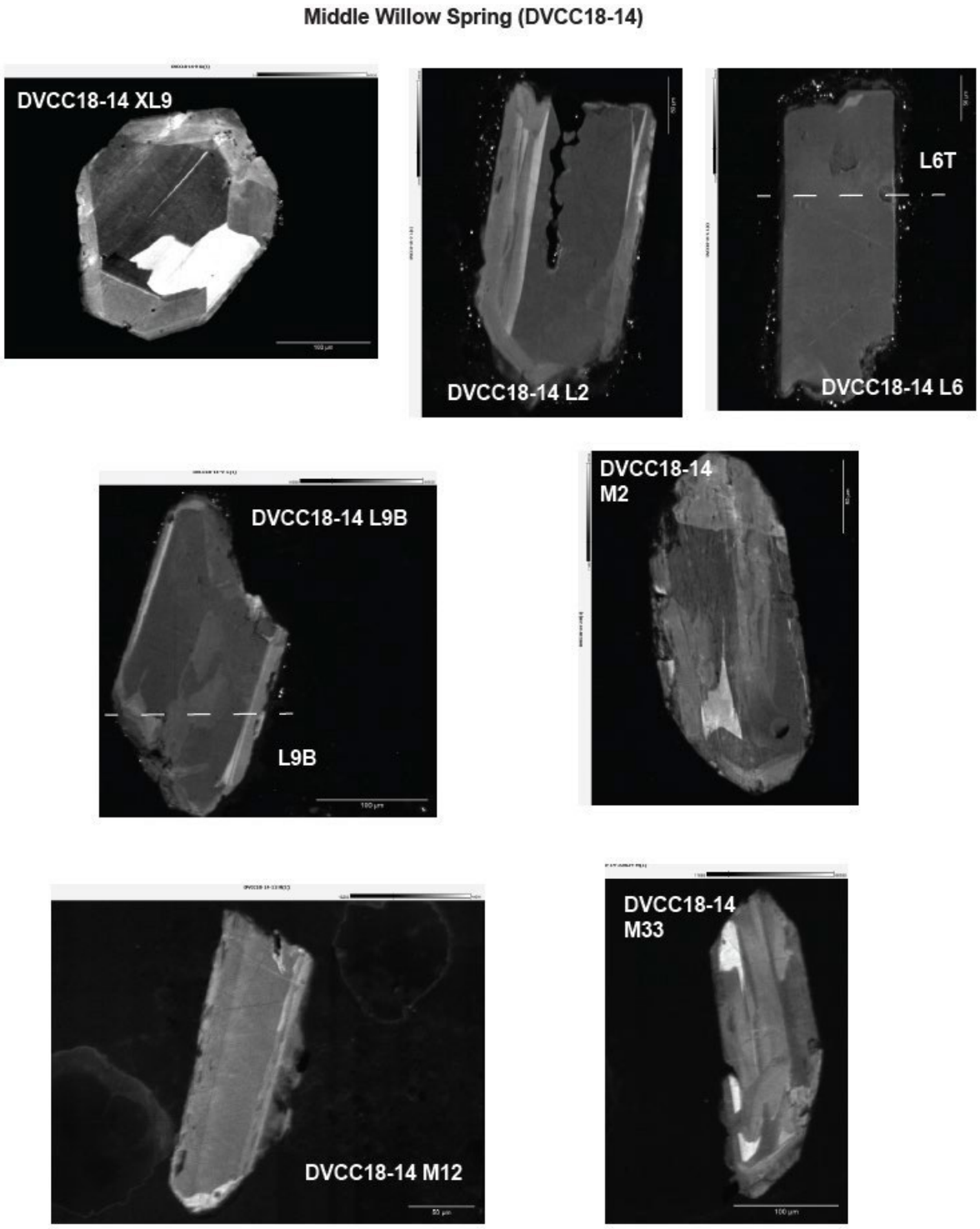

Figure S1. *Continued.*

Upper Willow Spring Diorite CL zircon images (DVCC18-5)

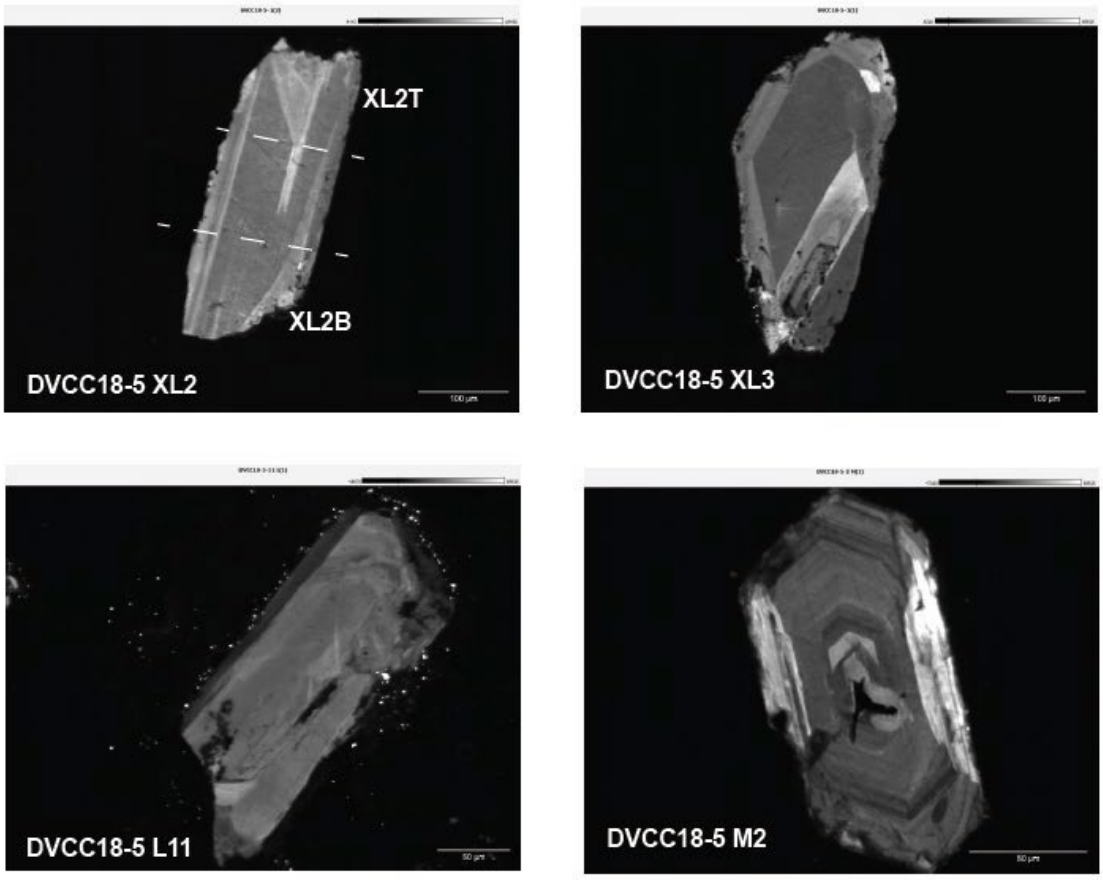

Granite of Deadman Pass (DVCC18-3)

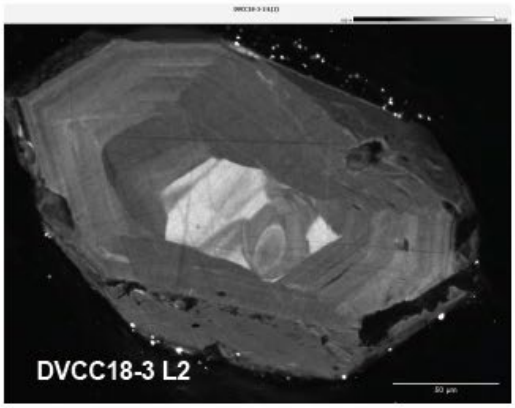

Figure S1. *Continued.*

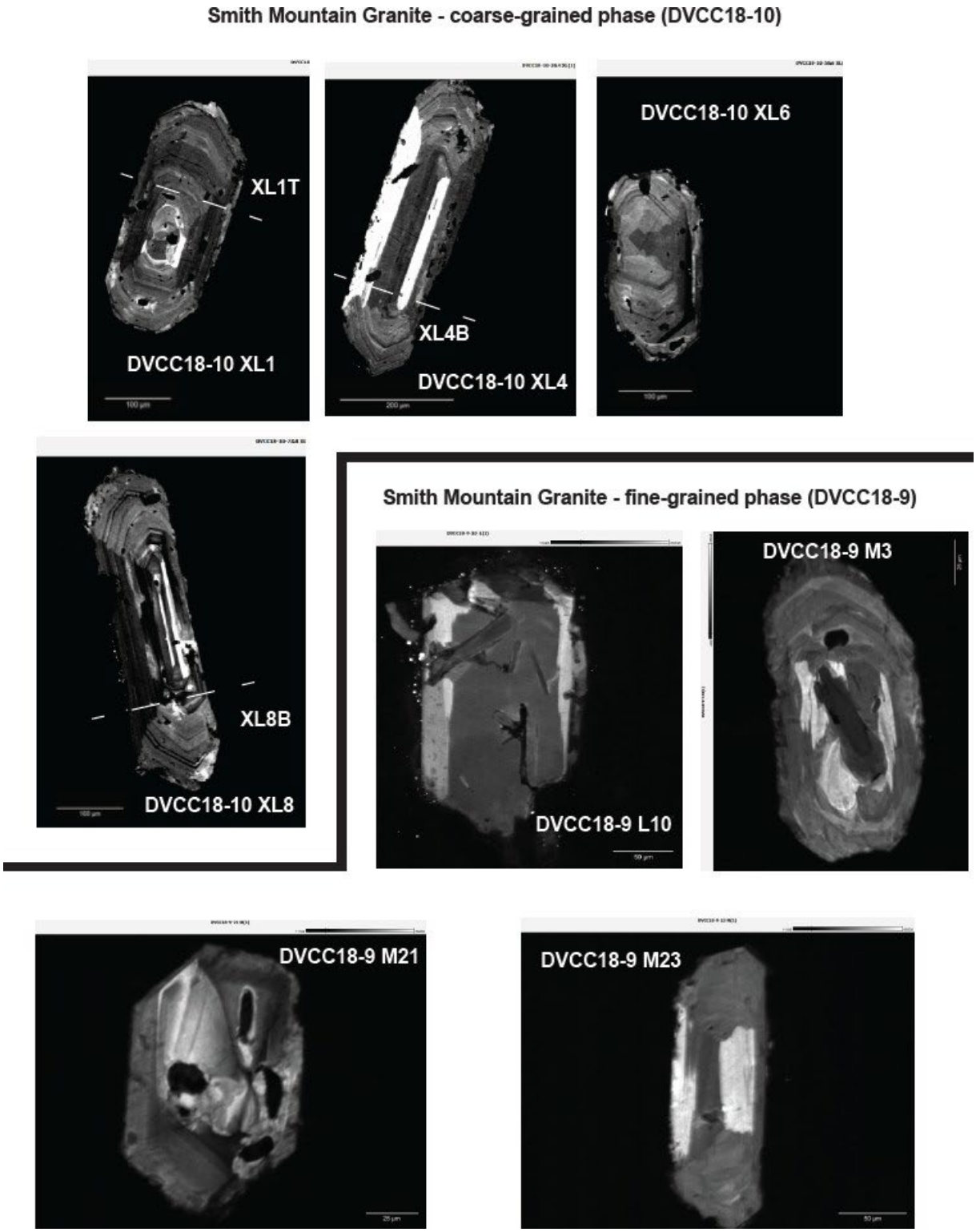

Figure S1. *Continued.*

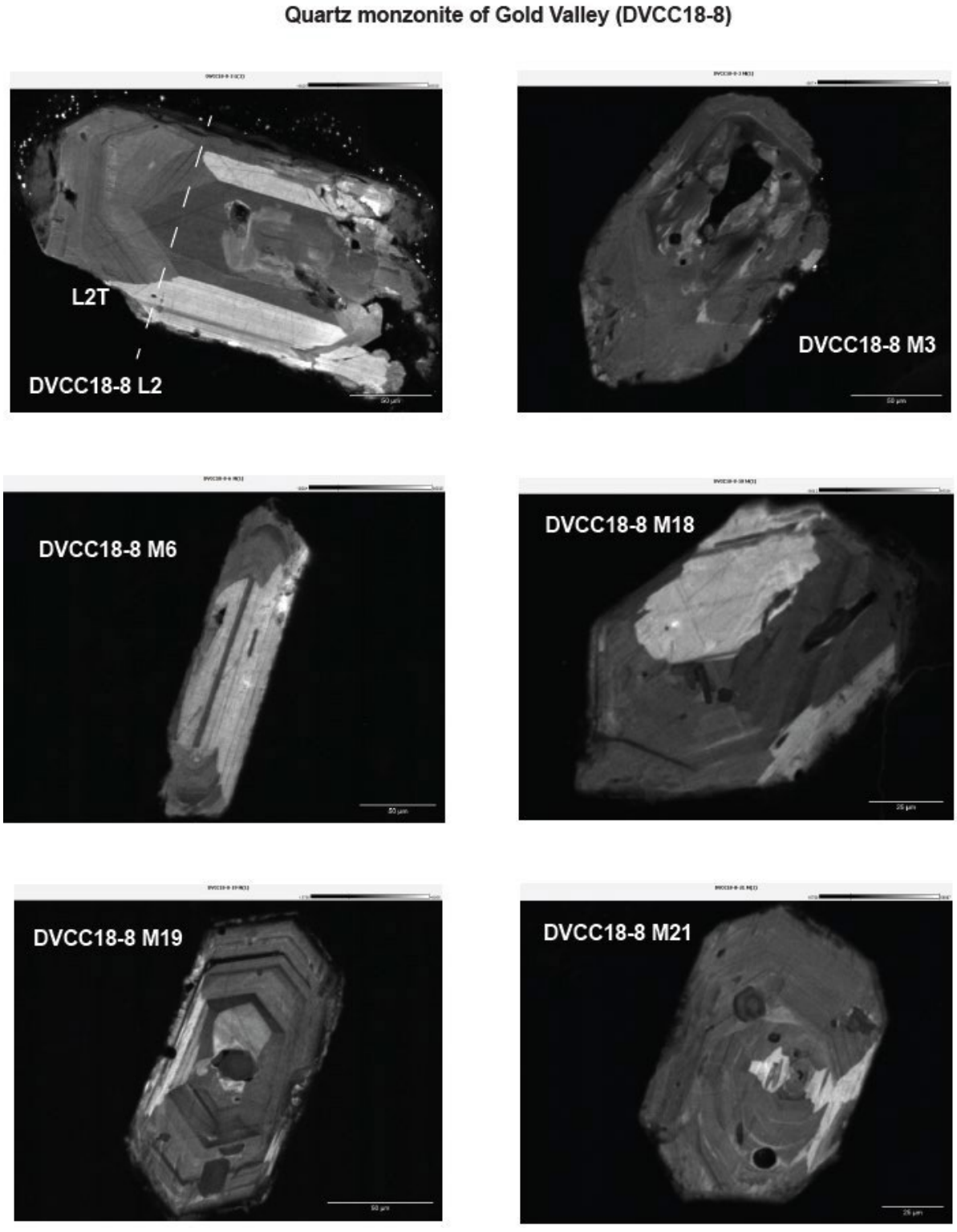

Figure S1. *Continued.*

Figure S2. Stacked plot of zircon $^{206}Pb/^{238}U$ dates. Each bar represents a single-grain date with 2σ. The minimum (blue) and maximum (red) lines were determined correspond are interpreted as estimates of the time at which the magmatic system reaches zircon saturation and the solidus, respectively. Zircon saturation timescales are determined by a Bayesian algorithm in the software Chron.jl (Keller et al., 2018). These results are also summarized in Table 4.

DVCC18-2
Willow Spring Diorite (lower)

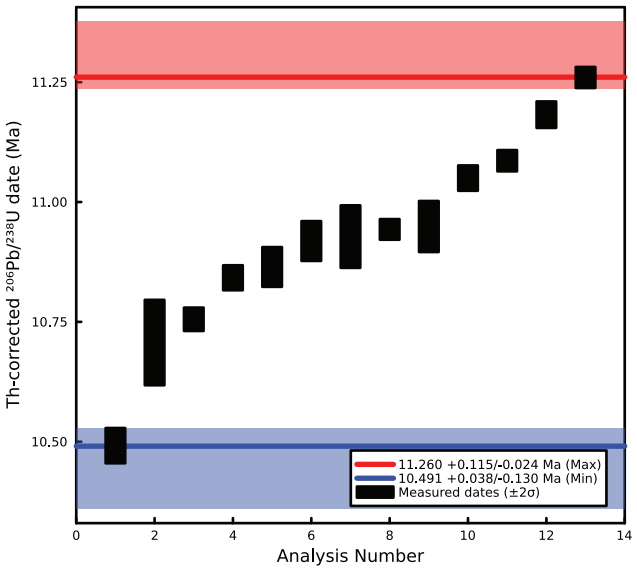

DVCC18-8
quartz monzonite of Gold Valley

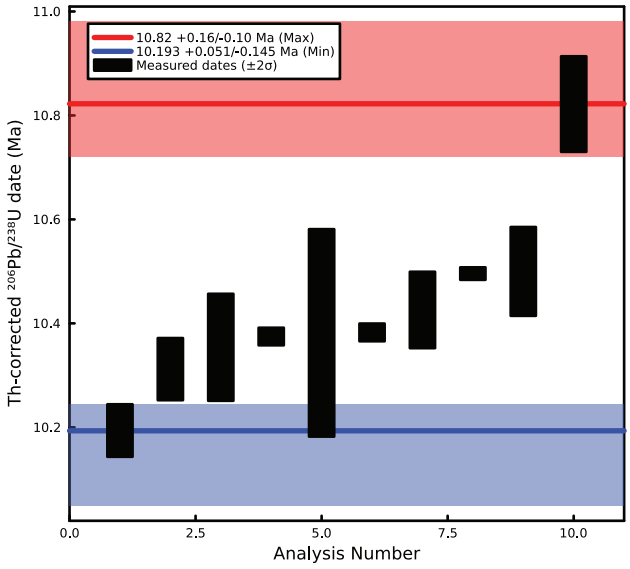

DVCC18-14
Willow Spring Diorite (middle)

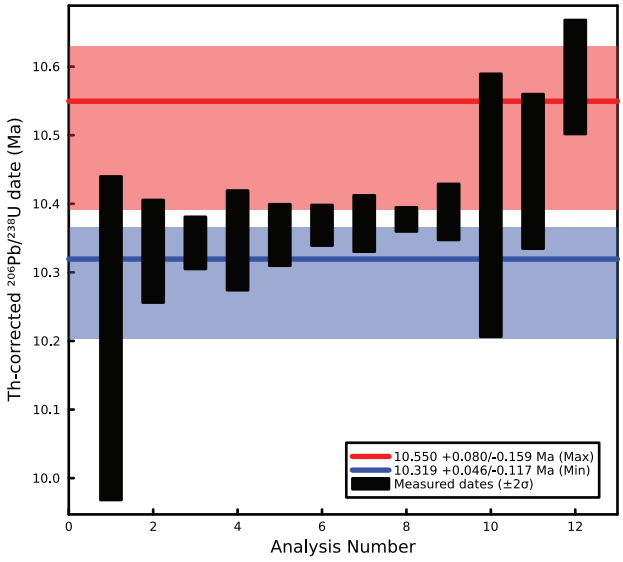

DVCC18-9
Smith Mountain Granite (fine-grained)

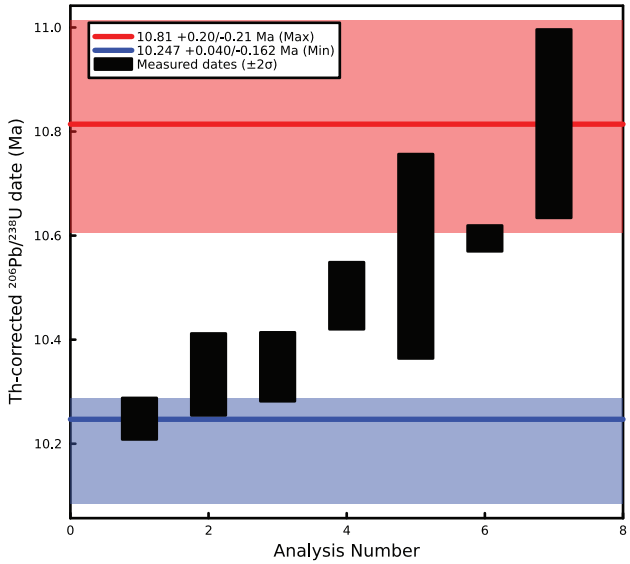

DVCC18-5
Willow Spring Diorite (upper)

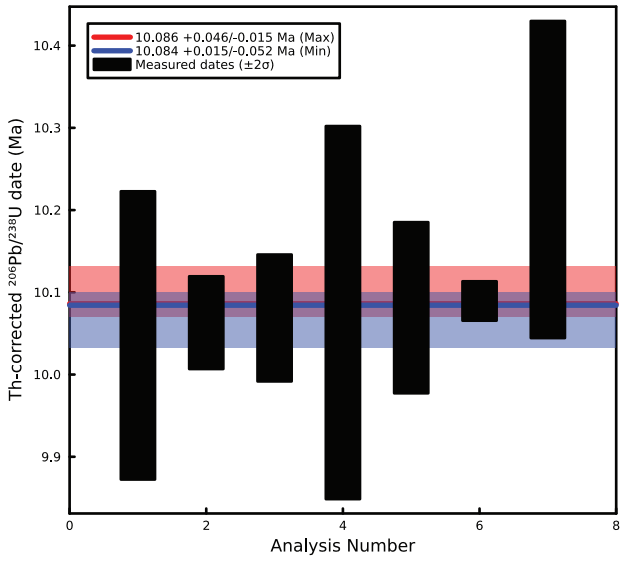

DVCC18-10
Smith Mountain Granite (coarse-grained)

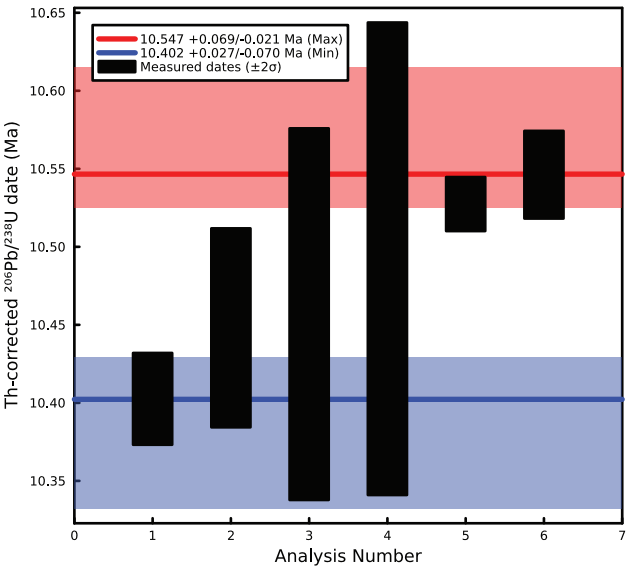

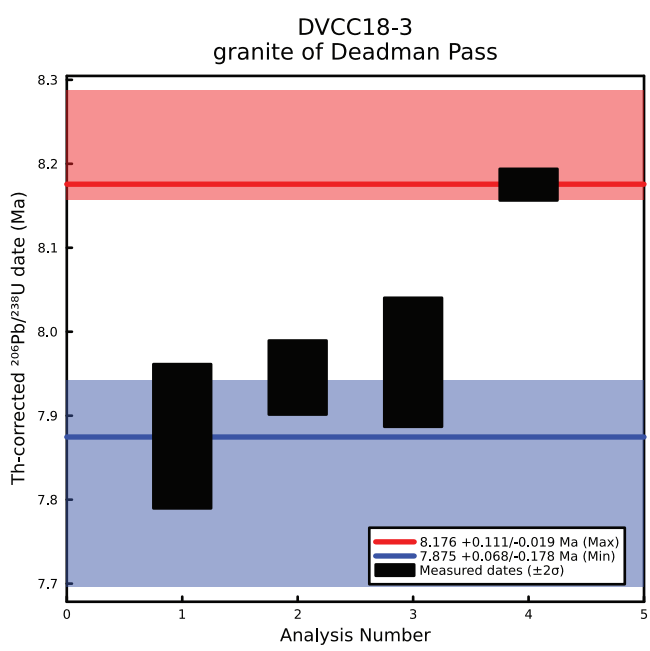
DVCC18-3
granite of Deadman Pass
Th-corrected 206Pb/238U date (Ma)
Analysis Number
8.176 +0.111/-0.019 Ma (Max)
7.875 +0.068/-0.178 Ma (Min)
Measured dates (±2σ)

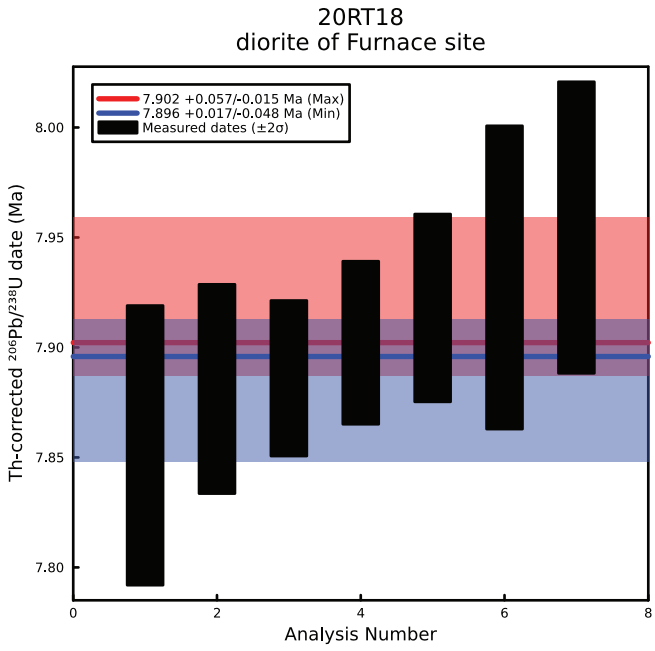
20RT18
diorite of Furnace site
Th-corrected 206Pb/238U date (Ma)
Analysis Number
7.902 +0.057/-0.015 Ma (Max)
7.896 +0.017/-0.048 Ma (Min)
Measured dates (±2σ)

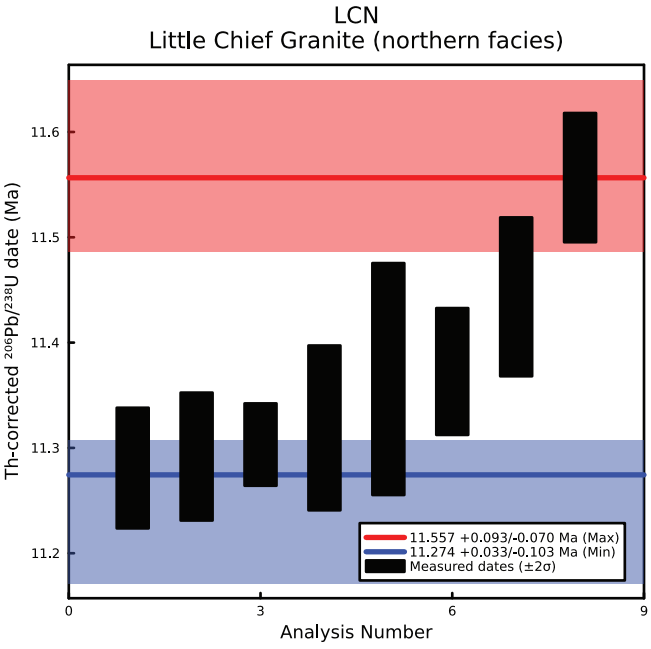
LCN
Little Chief Granite (northern facies)
Th-corrected 206Pb/238U date (Ma)
Analysis Number
11.557 +0.093/-0.070 Ma (Max)
11.274 +0.033/-0.103 Ma (Min)
Measured dates (±2σ)

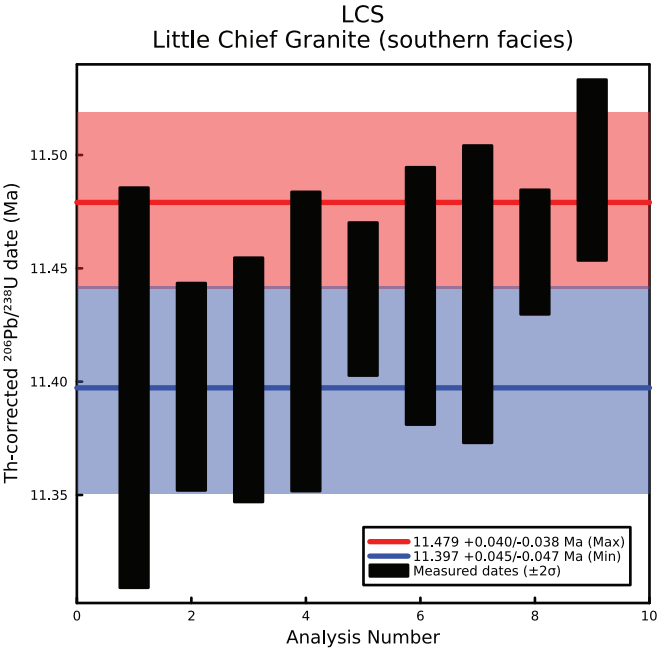
LCS
Little Chief Granite (southern facies)
Th-corrected 206Pb/238U date (Ma)
Analysis Number
11.479 +0.040/-0.038 Ma (Max)
11.397 +0.045/-0.047 Ma (Min)
Measured dates (±2σ)

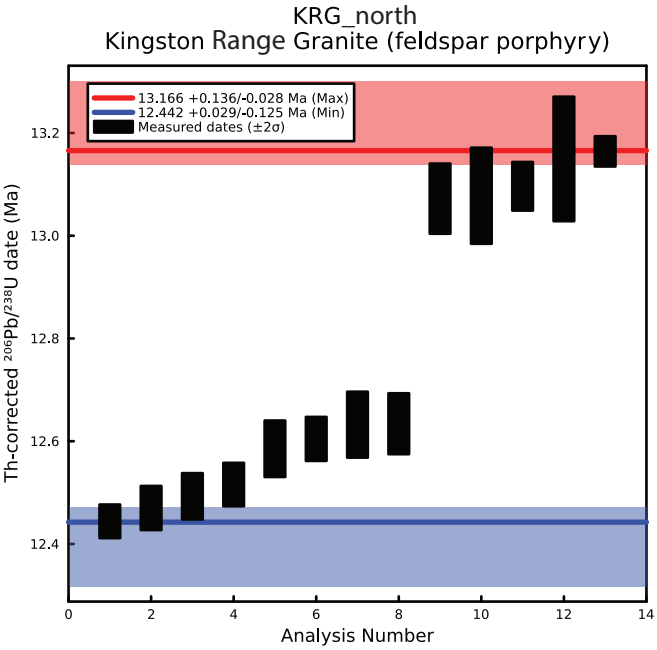
KRG_north
Kingston Range Granite (feldspar porphyry)
Th-corrected 206Pb/238U date (Ma)
Analysis Number
13.166 +0.136/-0.028 Ma (Max)
12.442 +0.029/-0.125 Ma (Min)
Measured dates (±2σ)

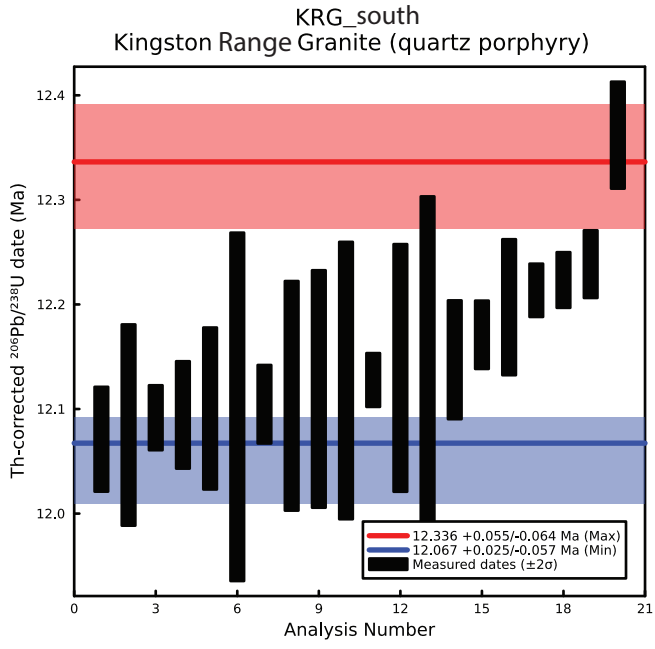
KRG_south
Kingston Range Granite (quartz porphyry)
Th-corrected 206Pb/238U date (Ma)
Analysis Number
12.336 +0.055/-0.064 Ma (Max)
12.067 +0.025/-0.057 Ma (Min)
Measured dates (±2σ)

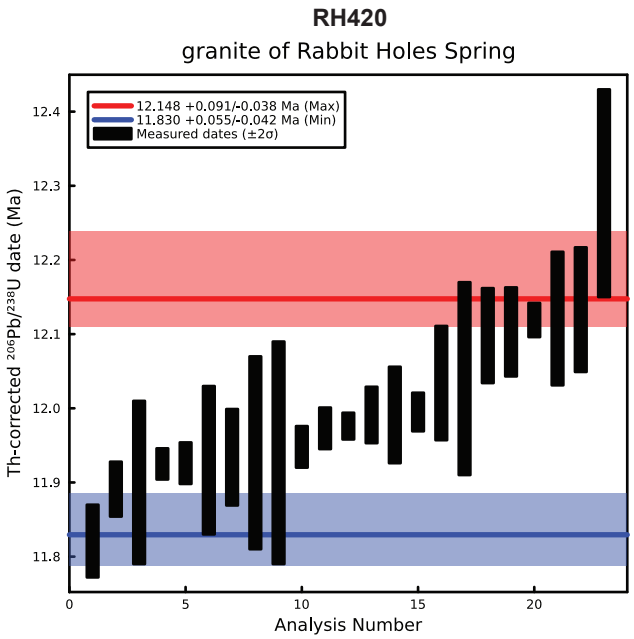
RH420
granite of Rabbit Holes Spring
12.148 +0.091/-0.038 Ma (Max)
11.830 +0.055/-0.042 Ma (Min)
Measured dates (±2σ)
Th-corrected 206Pb/238U date (Ma)
12.4
12.3
12.2
12.1
12.0
11.9
11.8
0
5
10
15
20
Analysis Number

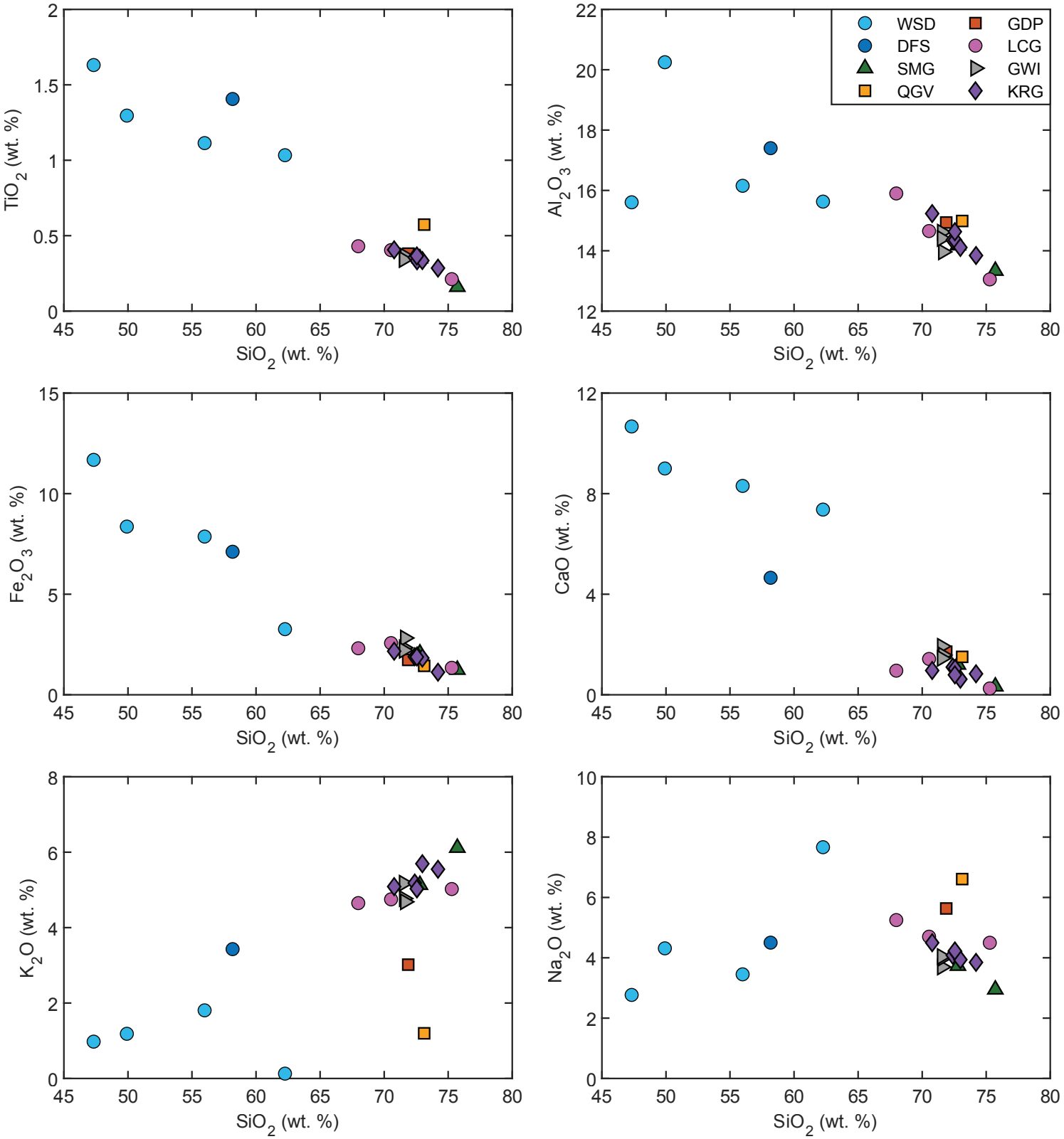

Figure S3. Whole-rock major element oxides versus SiO_2 content. WSD—Willow Spring Diorite (sensu lato), SMG—Smith Mountain Granite, QGV—quartz monzonite of Gold Valley, GDP—granite of Deadman Pass, LCG—Little Chief Granite, GWI—Greenwater Range intrusions, and KRG—Kingston Range Granite. WSD, SMG, QGV, and GDP data are from Gilmer and Thompson (2024). LCG, GWI, and KPG data are from Calzia and Rämo (2005). The WSD samples are more primitive with lower SiO_2 content, but higher and larger range of Fe_2O_3, TiO_2, CaO, and Al_2O_3 relative to the more felsic samples in the Death Valley extensional region.

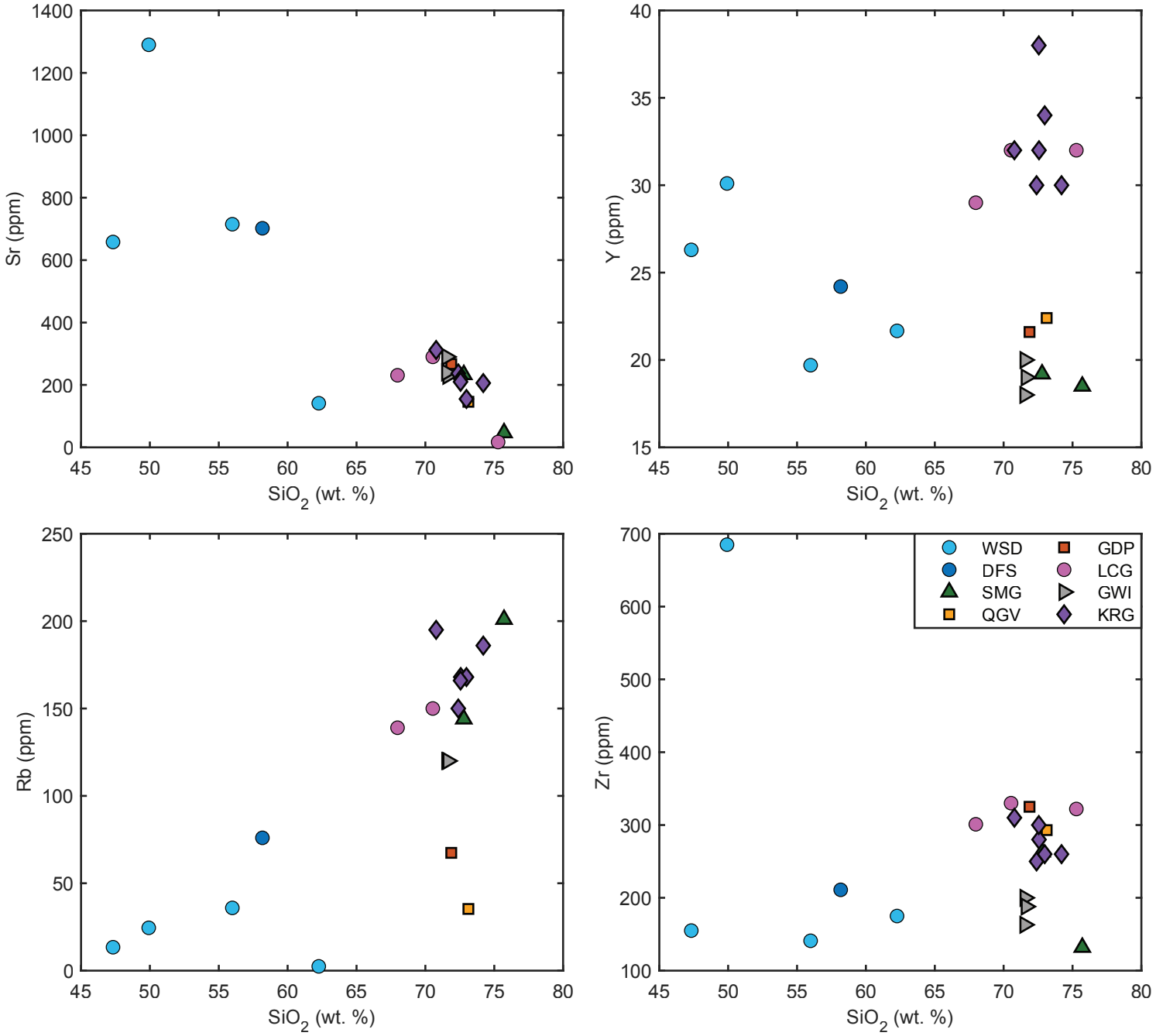

Figure S4. Comparison of whole-rock trace element compositions versus SiO_2 content. WSD— Willow Spring Diorite (sensu lato), SMG—Smith Mountain Granite, QGV—quartz monzonite of Gold Valley, GDP—granite of Deadman Pass, LCG—Little Chief Granite, GWI—Greenwater Range intrusions, and KRG— Kingston Range Granite. WSD, SMG, QGV, and GDP data are from Gilmer and Thompson (2024). LCG, GWI, and KPG data are from Calzia and Rämo (2005). The KPG and LCG share similar trace element compositions (Y, Zr, Nb) suggesting that they might all be derived from similar magma source(s). In the WSD samples, the decreasing Sr and Y trends with increasing SiO_2 are related to plagioclase and amphibole + accessory mineral phase (titanite+zircon) crystallization, respectively.

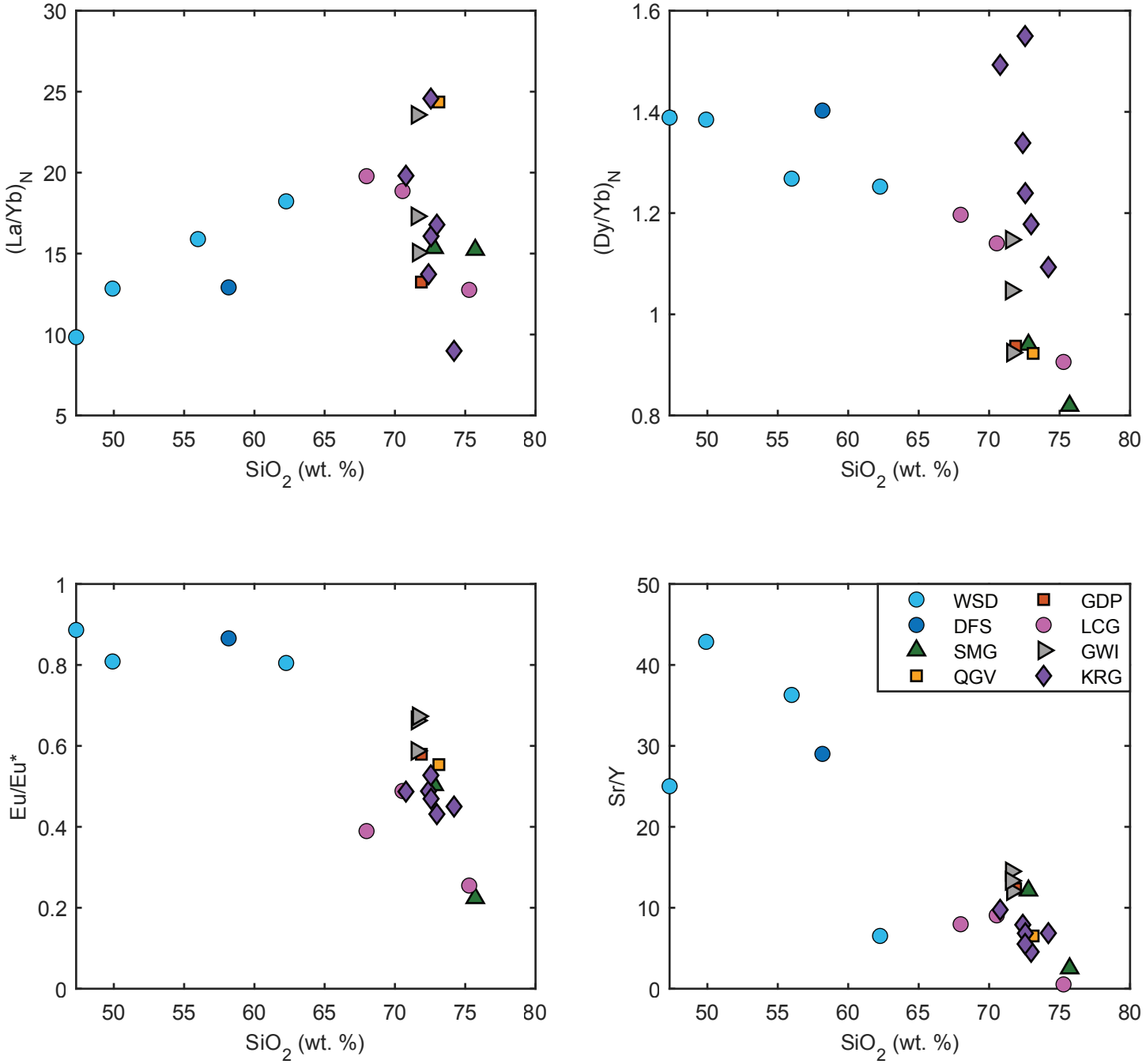

Figure S5. Plots of whole-rock REE ratios and Eu anomaly (Eu/Eu*) versus SiO_2 content. WSD—Willow Spring Diorite (sensu lato), SMG—Smith Mountain Granite, QGV—quartz monzonite of Gold Valley, GDP—granite of Deadman Pass, LCG—Little Chief Granite, GWI—Greenwater Range intrusions, and KRG— Kingston Range Granite. WSD, SMG, QGV, and GDP data are from Gilmer and Thompson (2024). LCG, GWI, and KP data are from Calzia and Rämo (2005). The WSD samples show increasing $(La/Yb)_N$ but decreasing $(Dy/Yb)_N$ with SiO_2. This is characteristic of amphibole crystallization from an evolving melt. However, WSD samples only have a small Eu anomaly, which is more likely related to the oxidation state of more mafic magmas as opposed to a lack of plagioclase fractionation (e.g., Trail et al., 2012). The leucocratic intrusions (SMG, QGV, GDP, LCG, and KRG) exhibit a large range in $(La/Yb)_N$ and $(Dy/Yb)_N$ that do not correlate with SiO_2 content but do show increasing Eu anomaly with SiO_2 suggesting that plagioclase crystallization was more prominent than amphibole crystallization.

Table S1. ID-TIMS 206Pb/238U zircon dates and zircon trace element concentrations (ppm) collected via TIMS-TEA. Th/U of the zircon is estimated from whole-rock Th/U ratios and the assumption that 232Th and 238U decay systems are concordant. If whole-rock Th/U is not available, the ratio is assumed to be 3.5. TIMS-TEA trace element uncertainties are expressed as 2σ percent while zircon date uncertainties are 2σ absolute. KRG—Kingston Range Granite (-F and -Q denote feldspar porphyry facies and quartz porphyry facies, respectively); GRHS—granite of Rabbit Holes Spring; LCG—Little Chief Granite (-N and -S denote northern and southern intrusive facies, respectively); WSD—Willow Spring Diorite; SMG—Smith Mountain Granite (-F and -C denote finer-grained and coarser-grained phases, respectively); QGV—quartz monzonite of Gold Valley; DFS—diorite of Furnace site; and GDP—granite of Deadman Pass.

fractionID	Abbrev. Sample Name	Date $^{206}Pb/^{238}U$ (Ma)	$^{206}Pb/^{238}U$ 2σ (abs)	Th/U	Y ppm	Y 2σ%	Zr ppm	Zr 2σ%	Hf ppm	Hf 2σ%	Th ppm	Th 2σ%	Sm ppm	Sm 2σ%
14L2	middle WSD	10.331	0.075	1.25	1278.3	0.31	486967	0.09	8466.6	0.09	559.1	0.24	8.3	0.51
14L6T	middle WSD	10.371	0.041	1.34	1360.0	0.09	486867	0.11	8385.8	0.11	528.3	0.09	9.9	0.10
14L9B	middle WSD	10.447	0.113	1.25									11.3	0.13
14M2	middle WSD	10.585	0.083	1.55	2092.3	0.06	485804	0.05	8238.6	0.06	1274.7	0.05		
14M12	middle WSD	10.388	0.041	1.20									7.3	0.35
14M33	middle WSD	10.398	0.192	1.12										
14XL9	middle WSD	10.377	0.018	1.20	1211.1	0.30	488031	0.06	7911.0	0.07	577.2	0.13		
14z2	middle WSD	10.355	0.045	1.17	1289.3	0.18	487120	0.10	8308.5	0.10	567.7	0.14	6.7	0.74
14z5	middle WSD	10.369	0.030	1.02	1018.0	0.34	487132	0.07	8884.8	0.07	428.4	0.16	6.8	0.68
14z12	middle WSD	10.204	0.236	0.88									5.8	0.89
14z15	middle WSD	10.343	0.038	0.92	622.3	0.55	487210	0.07	9338.1	0.08	242.0	0.30	6.5	0.52
14z19	middle WSD	10.347	0.073	1.46	938.4	0.50	486805	0.09	9209.7	0.09	784.0	0.19	2.9	1.74
2L2	lower WSD	10.919	0.042	0.92	1111.6	0.31	485440	0.07	10184.1	0.09	205.6	0.69	2.8	1.79
2L3	lower WSD	11.182	0.028	0.95	971.6	0.40	484883	0.07	10854.6	0.09	388.2	0.37	4.1	0.80
2L5	lower WSD	11.050	0.026	0.86									5.9	0.82
2L13	lower WSD	10.949	0.053	0.75	841.2	0.32	485549	0.08	10526.2	0.10	176.3	0.60	7.5	0.12
2M15	lower WSD	10.928	0.065	0.77	835.3	0.45	485433	0.07	10713.9	0.09	196.9	0.74	3.2	1.04
2XL2T	lower WSD	10.755	0.024	0.73	812.6	0.45	485292	0.07	10889.8	0.09	173.4	0.84	4.5	0.22
2XL3T	lower WSD	11.086	0.022	0.84									2.9	0.38
2XL7B	lower WSD	10.842	0.026	0.70	1063.9	0.27	484322	0.09	11348.6	0.10	300.3	0.36		
2XL8T	lower WSD	10.865	0.041	0.99	1287.3	0.27	485284	0.07	10100.7	0.09	215.7	0.67	1.7	0.00
2XL9B	lower WSD	10.492	0.037	1.21	1240.8	0.09	487925	0.11	7421.0	0.11	767.5	0.10	1.7	0.69
2XL10B	lower WSD	11.260	0.022	0.84	866.4	0.28	485100	0.08	10963.7	0.10	271.1	0.34	1.5	0.66
2XL10C	lower WSD	10.943	0.022	0.77	950.1	0.09	485149	0.07	10742.1	0.07	255.0	0.13	7.3	1.35
2XL10T	lower WSD	10.707	0.089	0.78	764.3	0.12	486385	0.05	9866.9	0.07	165.6	0.19	5.5	0.00
5L11	upper WSD	10.063	0.056	1.05	1355.1	0.24	484513	0.07	10721.4	0.07	336.1	0.22	16.8	0.07
5M2	upper WSD	10.048	0.175	0.90	1483.9	3.29	483713	0.27	11205.8	0.26	605.1	2.91	14.4	0.27

5XL2B	upper WSD	10.069	0.077	0.81	283.5	0.39	487076	0.07	10034.6	0.07	83.7	0.49	9.7	0.12
5XL2T	upper WSD	10.237	0.193	0.96	136.5	0.71	488723	0.05	8641.3	0.06	32.8	0.92	10.2	0.11
5XL3	upper WSD	10.089	0.024	1.07									12.4	0.08
5z1	upper WSD	10.075	0.227	1.00	920.7	1.03	487295	0.07	8655.8	0.07	157.1	2.26	22.6	0.03
5z5	upper WSD	10.081	0.104	0.42	1201.6	1.45	482614	0.08	12719.8	0.08	297.3	2.15	20.3	0.09
20RT18z5	DFS	7.855	0.064	1.59	2636.0	0.06	482762	0.03	10196.2	0.04	1004.3	0.05		
20RT18z8	DFS	7.881	0.048	1.95	1592.0	0.34	482777	0.03	11422.7	0.03	857.2	0.20	7.6	0.31
20RT18z10	DFS	7.886	0.035	2.35	1652.9	0.09	485541	0.03	9088.7	0.04	1226.9	0.04	7.3	1.44
20RT18z12	DFS	7.932	0.069	2.66	1767.0	0.08	484353	0.03	9987.9	0.04	1443.6	0.03	7.0	0.38
20RT18z17	DFS	7.902	0.037	2.84	2673.9	0.05	482384	0.03	10476.1	0.04	3071.4	0.03	5.0	1.08
20RT18z26	DFS	7.918	0.043	2.96	2883.8	0.03	483565	0.04	9115.2	0.05	1269.0	0.03	6.2	0.42
20RT18z29	DFS	7.955	0.066	2.13	3719.9	0.06	481693	0.03	9509.7	0.03	1432.7	0.05	4.0	1.32
3L2	GDP	8.175	0.019	0.91	1249.5	0.23	485875	0.07	9589.5	0.08	277.3	0.24	11.0	0.41
3z2	GDP	7.945	0.044	1.16	1400.2	0.15	486709	0.10	8476.4	0.10	223.2	0.38	5.3	1.04
3z4	GDP	7.876	0.086	1.26	1391.0	0.70	485134	0.07	10031.5	0.08	316.8	1.16	5.5	0.50
3z5	GDP	7.964	0.077	0.89	1299.2	0.18	486021	0.10	9334.5	0.10	198.8	0.49	5.9	0.78
8L2T	QGV	10.822	0.092	0.77	909.3	0.44	485185	0.07	10692.1	0.09	246.0	0.63	6.0	0.61
8M3	QGV	10.426	0.074	1.22	1369.3	0.17	485374	0.05	9808.1	0.05	395.6	0.18	1.1	0.00
8M6	QGV	10.382	0.200	1.06									10.1	0.83
8M18	QGV	10.500	0.085	0.87	1229.3	0.31	484316	0.07	11120.7	0.09	399.5	0.36	11.8	4.05
8M19	QGV	10.312	0.060	1.47	2167.9	0.18	483705	0.09	9992.4	0.09	1378.0	0.10	14.6	0.27
8M21	QGV	10.354	0.103	0.79	1150.3	0.44	484758	0.08	10693.6	0.09	336.4	0.55		
8z1	QGV	10.383	0.017	0.98	1362.2	0.17	485172	0.10	10053.9	0.10	413.4	0.21		
8z2	QGV	10.194	0.051	0.99										
8z3	QGV	10.375	0.017	0.76										
8z4	QGV	10.496	0.012	1.31										
9L10	SMG-F	10.484	0.064	0.89	1289.6	0.26	484334	0.07	11001.2	0.09	322.7	0.41		
9M3	SMG-F	10.815	0.181	1.16	1022.4	0.32	486242	0.09	9520.6	0.10	219.2	0.58		
9M21	SMG-F	10.560	0.196	1.21										
9M23	SMG-F	10.595	0.025	1.32										
9z8	SMG-F	10.333	0.079	1.05	1336.4	1.94	484293	0.12	11042.3	0.12	539.8	1.73		
9z9	SMG-F	10.348	0.066	0.96	1710.8	0.45	483835	0.07	10635.6	0.08	1352.0	0.18		
9z10	SMG-F	10.248	0.040	1.10	2253.6	2.04	483051	0.25	10410.8	0.25	1000.5	1.65		
10M6	SMG-C	10.403	0.029	1.42	2416.8	0.15	483405	0.09	10004.8	0.10	841.8	0.15		
10M17	SMG-C	10.457	0.119	1.09										

10XL1T	SMG-C	10.546	0.028	0.73										
10XL4B	SMG-C	10.492	0.151	0.77										
10XL6	SMG-C	10.527	0.017	0.97										
10XL8B	SMG-C	10.448	0.064	0.71										
90802	KRG-F	12.516	0.042	0.84										
90808	KRG-F	12.444	0.033	0.80										
90814	KRG-F	12.493	0.045	0.90										
90815	KRG-F	12.585	0.055	0.83										
KRG2220	KRG-F	12.470	0.043	0.53										
KRG050107	KRG-F	13.072	0.068	1.22										
KRG050108	KRG-F	13.078	0.094	0.93										
KRG050109	KRG-F	13.149	0.121	0.98										
KRG050111	KRG-F	13.164	0.029	0.85										
KRG051015	KRG-F	12.605	0.043	1.23										
KRG0125011	KRG-F	13.096	0.047	0.71										
KRGK3	KRG-F	12.634	0.059	1.08										
KRGo4	KRG-F	12.632	0.064	0.89										
90812	KRG-Q	12.223	0.027	0.70										
KRG012505	KRG-Q	12.197	0.065	0.88										
90804	KRG-Q	12.171	0.033	0.54										
90807	KRG-Q	12.214	0.025	0.84										
KRN-13M	KRG-Q	12.071	0.050	0.98										
90904	KRG-Q	12.119	0.114	1.20										
90905	KRG-Q	12.113	0.110	1.44										
90906	KRG-Q	12.139	0.118	1.28										
90907	KRG-Q	12.127	0.133	0.92										
90908	KRG-Q	12.144	0.160	1.45										
90909	KRG-Q	12.102	0.167	1.00										
K1209162001	KRG-Q	12.128	0.026	0.98										
K1209162002	KRG-Q	12.100	0.077	1.07										
K1209162003	KRG-Q	12.147	0.057	1.03										
K1209162004	KRG-Q	12.105	0.038	1.26										
K1209162005	KRG-Q	12.092	0.031	0.96										
K1209162006	KRG-Q	12.094	0.051	0.93										
K1209162008	KRG-Q	12.239	0.032	0.83										

K1209162009	KRG-Q	12.085	0.096	1.35										
K1209162011	KRG-Q	12.362	0.051	1.80										
51304	LCG-N	11.319	0.078	0.92										
51305	LCG-N	11.292	0.061	1.12										
51307	LCG-N	11.365	0.110	1.05										
51309	LCG-N	11.281	0.057	1.06										
51312	LCG-N	11.303	0.039	1.07										
91501	LCG-N	11.373	0.060	1.01										
91507	LCG-N	11.443	0.075	1.00										
91508	LCG-N	11.557	0.061	1.10										
41313	LCG-S	11.457	0.027	1.50										
90913	LCG-S	11.438	0.057	1.38										
90914	LCG-S	11.493	0.040	1.06										
F-3	LCG-S	11.418	0.066	2.29										
F-5	LCG-S	11.401	0.054	1.59										
F-6	LCG-S	11.439	0.066	1.80										
F-7	LCG-S	11.436	0.034	1.47										
F-8	LCG-S	11.398	0.046	1.44										
F-10	LCG-S	11.397	0.088	2.45										
2T12	GRHS	11.821	0.049	1.43										
2T10	GRHS	11.891	0.037	0.75										
2T13	GRHS	11.9	0.11	0.94										
04	GRHS	11.926	0.028	0.93										
05	GRHS	11.925	0.021	1.12										
11	GRHS	11.934	0.065	0.88										
2T08	GRHS	11.94	0.13	1.01										
2T09	GRHS	11.94	0.15	1.21										
06	GRHS	11.948	0.028	1.20										
2T02	GRHS	11.93	0.1	1.77										
14	GRHS	11.973	0.028	0.88										
03	GRHS	11.976	0.018	0.26										
02	GRHS	11.991	0.038	1.84										
2T04	GRHS	11.991	0.065	0.93										
13	GRHS	11.995	0.026	0.41										
2T03	GRHS	12.034	0.077	1.95										
2T01	GRHS	12.04	0.13	0.83										
2T05	GRHS	12.098	0.064	1.46										

T15	GRHS	12.103	0.06	0.95										
08	GRHS	12.119	0.023	0.97										
T09	GRHS	12.121	0.09	1.59										
2T14	GRHS	12.133	0.084	0.98										
T05	GRHS	12.29	0.14	0.8										

Eu ppm	Eu 2σ%	Gd ppm	Gd 2σ%	Tb ppm	Tb 2σ%	Dy ppm	Dy 2σ%	Ho ppm	Ho 2σ%	Er ppm	Er 2σ%	Tm ppm	Tm 2σ%	Yb ppm	Yb 2σ%	Lu ppm	Lu 2σ%
3.0	0.88	33.6	0.17	10.1	0.66	112.9	0.11	39.9	0.33	184.9	0.20	41.5	1.00	382.9	0.11	82.2	0.55
3.2	0.16	40.5	0.09	11.9	0.11	128.4	0.10	45.0	0.09	212.0	0.09	46.7	0.17	410.9	0.11	83.5	0.11
4.6	0.19	89.6	0.09	16.0	0.15	178.1	0.05	65.5	0.07	310.4	0.05	68.5	0.19	592.5	0.06	126.1	0.12
20.5	1.12	94.8	1.17	10.4	1.19	129.6	0.29	38.0	0.32	184.7	0.19	41.2	0.56	383.3	0.07	82.3	0.24
2.4	0.67	30.1	0.12	9.5	0.42	108.3	0.09	39.3	0.20	188.0	0.12	43.1	0.57	401.2	0.09	86.1	0.31
13.1	1.82	105.1	1.22	10.7	1.05	119.4	0.29	32.5	0.34	152.4	0.22	33.3	0.64	308.6	0.07	67.8	0.26
1.7	0.00	27.4	3.41	4.2	2.71	59.5	0.65	19.0	0.59	97.4	0.35	22.0	0.92	212.7	0.10	47.9	0.36
1.9	1.62	23.5	0.28	7.1	1.09	79.6	0.18	28.2	0.56	137.7	0.33	31.3	1.51	288.2	0.16	63.2	0.83
1.2	1.98	27.7	0.24	7.9	0.83	96.9	0.09	37.6	0.26	184.2	0.14	40.0	0.95	349.8	0.09	75.6	0.57
1.7	1.58	33.3	0.22	6.0	1.22	74.1	0.14	29.1	0.39	151.6	0.20	36.9	1.13	358.3	0.10	79.8	0.59
1.2	1.54	19.7	0.26	10.0	0.48	72.0	0.10	27.7	0.27	135.5	0.15	31.2	0.93	285.2	0.09	62.3	0.52
0.6	4.31	15.5	0.49	5.2	1.35	66.5	0.15	26.0	0.41	130.3	0.22	31.5	1.26	292.7	0.12	64.2	0.71
0.5	5.33	15.0	0.49	5.1	1.33	64.3	0.15	26.1	0.40	130.5	0.22	30.2	1.29	284.7	0.12	63.0	0.71
0.5	4.19	18.4	0.24	6.5	0.78	84.5	0.11	34.0	0.29	178.3	0.15	41.5	0.73	391.5	0.09	84.7	0.39
1.3	1.87	30.4	0.22	9.7	0.69	115.5	0.08	42.4	0.23	196.4	0.14	45.0	0.86	405.6	0.08	84.4	0.52
2.9	0.20	68.2	0.13	9.1	0.16	107.1	0.10	39.8	0.09	192.6	0.09	44.5	0.20	403.2	0.11	81.1	0.12
0.6	3.14	15.0	0.32	5.4	0.86	66.7	0.10	26.6	0.26	138.2	0.13	33.7	0.78	320.7	0.08	69.2	0.42
0.6	1.40	16.9	0.09	5.9	0.26	74.6	0.06	29.8	0.10	157.0	0.06	37.2	0.28	337.7	0.06	75.7	0.11
0.3	1.92	12.5	0.14	4.8	0.39	62.3	0.06	24.7	0.13	130.1	0.07	30.4	0.31	276.9	0.06	62.8	0.18
4.1	7.89	72.2	1.21	10.6	1.08	146.9	0.26	45.4	0.23	223.0	0.14	48.9	0.43	453.9	0.06	99.1	0.18
0.7	0.00	24.6	2.99	9.0	8.50	117.9	1.41	47.4	3.45	245.5	2.02	58.6	7.89	539.7	1.02	120.5	4.43
0.4	2.16	4.1	0.44	1.5	1.24	19.7	0.17	8.3	0.44	46.2	0.23	11.8	1.09	121.9	0.10	31.5	0.32
0.3	1.71	4.3	0.41	1.1	1.59	14.0	0.23	5.2	0.62	27.1	0.35	6.6	1.34	66.2	0.17	16.0	0.70
1.6	3.75	24.2	0.57	6.6	2.30	78.5	0.38	29.4	1.08	149.6	0.62	35.1	2.63	338.3	0.28	79.2	1.31
0.9	0.00	29.2	0.88	8.1	3.42	101.6	0.56	39.4	1.48	201.1	0.86	49.0	3.42	485.3	0.37	109.1	1.75
6.2	0.15	111.9	0.07	20.1	0.20	233.5	0.04	85.8	0.09	417.7	0.05	93.0	0.39	810.4	0.04	180.0	0.08
6.7	0.45	516.8	0.07	10.3	1.34	127.7	0.22	49.6	0.62	250.4	0.32	56.1	2.21	489.8	0.19	106.7	0.49

3.4	0.28	56.7	0.14	12.1	0.34	144.0	0.05	54.5	0.16	269.7	0.08	61.6	0.61	573.2	0.04	126.8	0.12
5.0	0.18	179.7	0.07	12.9	0.30	151.9	0.04	56.7	0.14	278.5	0.07	63.8	0.56	577.1	0.04	126.0	0.12
4.0	0.21	45.6	0.19	18.4	0.19	221.8	0.04	84.6	0.08	423.2	0.04	98.4	0.32	893.7	0.04	193.2	0.07
8.3	0.04	86.5	0.08	26.1	0.05	288.8	0.05	98.1	0.04	439.7	0.04	94.0	0.12	772.4	0.05	154.5	0.04
9.2	0.15	252.0	0.07	27.4	0.22	318.3	0.04	119.1	0.10	572.3	0.05	120.2	0.47	975.2	0.04	217.6	0.11
2.4	0.00	58.5	1.26	9.0	1.12	129.8	0.26	40.8	0.23	205.0	0.13	44.6	0.41	412.7	0.06	88.4	0.17
1.8	0.84	31.3	0.11	10.6	0.34	122.3	0.09	45.0	0.16	218.6	0.10	49.5	0.46	447.2	0.09	95.5	0.25
1.9	3.35	31.2	0.46	10.1	1.58	118.0	0.25	44.6	0.74	217.6	0.44	48.8	2.00	449.2	0.21	97.2	1.13
1.2	1.47	28.3	0.13	9.6	0.43	114.0	0.09	42.7	0.19	204.9	0.12	45.2	0.57	410.0	0.09	88.0	0.31
1.3	2.08	67.3	0.16	5.9	1.28	73.2	0.15	29.5	0.39	145.5	0.21	34.9	1.23	315.8	0.12	70.6	0.69
1.3	1.22	30.7	0.13	10.0	0.44	122.5	0.06	46.7	0.16	229.5	0.09	50.8	0.45	449.7	0.06	96.4	0.29
0.5	5.69	21.7	0.35	7.4	0.99	93.4	0.11	38.0	0.28	192.8	0.15	45.7	0.90	438.2	0.08	97.1	0.47
2.0	1.51	48.1	0.12	15.0	0.47	178.5	0.08	67.6	0.20	342.9	0.11	79.3	0.54	718.7	0.09	161.2	0.28
1.2	2.92	60.9	0.18	6.9	1.23	90.9	0.17	36.0	0.47	191.4	0.25	45.6	1.13	436.9	0.11	94.7	0.59
0.8	2.10	24.9	0.14	8.9	0.47	111.8	0.09	43.4	0.18	218.5	0.11	49.6	0.51	451.6	0.09	97.3	0.28
0.9	2.65	26.3	0.25	8.6	0.75	106.0	0.09	40.1	0.24	196.4	0.13	46.1	0.81	427.6	0.08	93.3	0.44
1.2	1.85	37.9	0.14	8.1	0.69	95.4	0.11	35.5	0.31	178.2	0.17	38.9	0.88	348.7	0.10	73.8	0.51
0.0	0.00			7.6	5.39	103.3	0.83	41.9	2.07	223.2	1.16	53.9	4.59	518.5	0.53	117.7	2.41
2.9	1.78	45.2	0.24	12.1	1.07	143.9	0.16	55.1	0.47	281.4	0.26	66.5	1.18	636.5	0.11	140.7	0.61
4.2	6.84	122.3	0.56	15.4	4.71	186.7	0.83	72.6	2.12	361.8	1.29	86.8	5.05	800.4	0.64	175.6	2.88
2.9	0.92	65.8	0.09	19.8	0.31	227.3	0.08	81.1	0.15	373.7	0.10	81.9	0.48	701.7	0.09	143.5	0.29